Advanced Virgo Baseline Design

VIR–027A–09

Issue 1

The Virgo Collaboration

May 16, 2009

F. Acernese[5ac], M. Alshourbagy[10ab], F. Antonucci[11a], S. Aoudia[6], K.G. Arun[7], P. Astone[11a], G. Ballardin[2], F. Barone[5ac], M. Barsuglia[14], Th.S. Bauer[12a], M. Beker[12], S. Bigotta[10ab], S. Birindelli[6], M.A. Bizouard[7], C. Boccara[8], F. Bondu[6], L. Bonelli[10ab], L. Bosi[9a], S. Braccini[10a], C. Bradaschia[10a], A. Brillet[6], V. Brisson[7], H.J. Bulten[12ab], D. Buskulic[1], G. Cagnoli[3a], E. Calloni[5ab], E. Campagna[3ac], B. Canuel[2], F. Carbognani[2], L. Carbone[9a], F. Cavalier[7], R. Cavalieri[2], G. Cella[10a], E. Chassande-Mottin[14], S. Chatterji[11a], A. Chincarini[16], F. Cleva[6], E. Coccia[13ab], P.F. Cohadon[**], J. Colas[2], M. Colombini[11b], C. Corda[10ab], A. Corsi[11a], J.-P. Coulon[6], E. Cuoco[2], S. D'Antonio[13a], A. Dari[9ab], V. Dattilo[2], M. Davier[7], R. Day[2], R. De Rosa[5ab], M. del Prete[10ac], L. Di Fiore[5a], A. Di Lieto[10ab], M. Di Paolo Emilio[13ad], A. Di Virgilio[10a], M. Drago[15cd], V. Fafone[13ab], I. Ferrante[10ab], F. Fidecaro[10ab], I. Fiori[2], R. Flaminio[4], J.-D. Fournier[6], J. Franc[4], S. Frasca[11ab], F. Frasconi[10a], A. Freise[*], L. Gammaitoni[9ab], F. Garufi[5ab], G. Gemme[16], E. Genin[2], A. Gennai[10a], A. Giazotto[10a], M. Granata[14], V. Granata[1], C. Greverie[6], G. Guidi[3ac], A. Heidmann[**], H. Heitmann[6], P. Hello[7], S. Hild[*], D. Huet[2], P. La Penna[2], M. Laval[6], N. Leroy[7], N. Letendre[1], M. Lorenzini[3a], V. Loriette[8], G. Losurdo[3a], J.-M. Mackowski[4], E. Majorana[11a], N. Man[6], M. Mantovani[2], F. Marchesoni[9a], F. Marion[1], J. Marque[2], F. Martelli[3ac], A. Masserot[1], F. Menzinger[2], C. Michel[4], L. Milano[5ab], Y. Minenkov[13a], M. Mohan[2], J. Moreau[8], N. Morgado[4], A. Morgia[13ab], S. Mosca[5ab], B. Mours[1], I. Neri[9ab], F. Nocera[2], G. Pagliaroli[13ab], C. Palomba[11a], F. Paoletti[10a,2], S. Pardi[5ab], A. Pasqualetti[2], R. Passaquieti[10ab], D. Passuello[10a], G. Persichetti[5ab], F. Piergiovanni[3ac], L. Pinard[4], R. Poggiani[10ab], G.A. Prodi[15ab], M. Punturo[9a], P. Puppo[11a], O. Rabaste[14], P. Rapagnani[11ab], V. Re[15ab], T. Regimbau[6], F. Ricci[11ab], F. Robinet[7], A. Rocchi[13a], L. Rolland[1], R. Romano[5ac], P. Ruggi[2], F. Salemi[15ab], B. Sassolas[4], D. Sentenac[2], R. Sturani[3c], B. Swinkels[2], R. Terenzi[13ac], A. Toncelli[10ab], M. Tonelli[10ab], E. Tournefier[1], F. Travasso[9ab], J.Trummer[1], G. Vajente[10ab], J.F.J. van den Brand[12ab], S. van der Putten[12a], G. Vedovato[15c], D. Verkindt[1], F. Vetrano[3ac], A. Viceré[3ac], J.-Y. Vinet[6], H. Vocca[9a], M.Was[7], M. Yvert[1]

[1] *Laboratoire d'Annecy-le-Vieux de Physique des Particules (LAPP), IN2P3/CNRS, Université de Savoie, F-74941 Annecy-le-Vieux, France*

[2] *European Gravitational Observatory (EGO), I-56021 Cascina (Pi), Italy*

[3] *INFN, Sezione di Firenze, I-50019 Sesto Fiorentino[a]; Università degli Studi di Firenze, I-50121[b], Firenze; Università degli Studi di Urbino "Carlo Bo", I-61029 Urbino[c], Italy*

[4] *Laboratoire des Matériaux Avancés (LMA), IN2P3/CNRS, F-69622 Villeurbanne, Lyon, France*

[5] *INFN, sezione di Napoli [a]; Università di Napoli "Federico II"[b] Complesso Universitario di Monte S.Angelo, I-80126 Napoli; Università di Salerno, Fisciano, I-84084 Salerno[c], Italy*

[6] *Departement Artemis, Observatoire de la Côte d'Azur, CNRS, F-06304 Nice, France.*

[7] *LAL, Université Paris-Sud, IN2P3/CNRS, F-91898 Orsay, France*

[8] *ESPCI, CNRS, F-75005 Paris, France*

[9] *INFN, Sezione di Perugia[a]; Università di Perugia[b], I-6123 Perugia,Italy*

[10] *INFN, Sezione di Pisa[a]; Università di Pisa[b]; I-56127 Pisa; Università di Siena, I-53100 Siena[c], Italy*

[11] *INFN, Sezione di Roma[a]; Università "La Sapienza"[b], I-00185 Roma, Italy*

[12] *National institute for subatomic physics, NL-1009 DB[a]; Vrije Universiteit, NL-1081 HV [b], Amsterdam, The Netherlands*

[13] *INFN, Sezione di Roma Tor Vergata[a]; Università di Roma Tor Vergata[b], Istituto di Fisica dello Spazio Interplanetario (IFSI) INAF[c], I-00133 Roma; Università dell'Aquila, I-67100 L'Aquila[d], Italy*

[14] *AstroParticule et Cosmologie (APC), CNRS: UMR7164-IN2P3-Observatoire de Paris-Université Denis Diderot-Paris VII - CEA : DSM/IRFU*

[15] *INFN, Gruppo Collegato di Trento[a] and Università di Trento[b], I-38050 Povo, Trento, Italy; INFN, Sezione di Padova[c] and Università di Padova[d], I-35131 Padova, Italy*

[16] *INFN, Sezione di Genova; I-16146 Genova, Italy*

[*] *Permanent address: School of Physics & Astronomy, University of Birmingham, B15 2TT, UK*

[**] *Permanent address: Laboratoire Kastler Brossel, UPMC-ENS-CNRS, Paris Cedex 05, France.*

Contents

Advanced Virgo Baseline Design:

PART 1:

Design overview, sensitivity, science case

1 Introduction

Interferometric gravitational wave (GW) detectors of the first generation (Virgo, LIGO, GEO600) have successfully completed their first long-duration data taking runs and a new one is going to start soon. Upgrades that exploits available technology and allow to enhance the accessible volume of universe by about a factor 10 (Virgo+, Enhanced LIGO) are currently being performed and will allow to improve the sensitivities by ~ 2. However, it will be the second generation of gravitational wave detectors, that will give us the chance to open an exciting new window on the universe.

Advanced Virgo (AdV) is the project to upgrade the Virgo detector to a second generation instrument. AdV will be able to scan a 1000 times larger volume of the Universe than initial Virgo. Even though it will be hosted in the same infrastructures as Virgo, the AdV sensitivity (see sec. 3) will be better by one order of magnitude over most of the detection band.

The effort of the Virgo Collaboration towards the design of a second generation detector started in 2005 with the *Advanced Virgo White Paper* [1]. In fall 2007 an *Advanced Virgo Conceptual Design* was proposed [2] and submitted to the funding agencies together with a *Preliminary project execution plan and cost plan* [3]. Finally, in fall 2007 the *Advanced Virgo Preliminary Design* [4] was released.

This *Advanced Virgo Baseline Design* provides a description of the reference design solutions adopted for AdV:

- in the first part the concept of AdV is introduced, with an overview of the main design features and the expected achievable sensitivity. The science case for AdV is discussed, describing the scenarios for the expected detection rates, the benefits of a network of GW detectors (AdV will join Advanced LIGO [5]) and the opportunities from multi-messenger observations;
- in the second part the design of the interferometer is described: optical configuration, laser, injection system, mirrors, thermal compensation, detection system and interferometer sensing and control;
- part three is dedicated to the vibration isolation system. It describes the planned changes on the Virgo superattenuator, especially on the payload, that has to be compliant with a bigger mirror and fused silica suspension fibers;
- though AdV will be host in the same Virgo facilities important upgrades of the vacuum system and of some infrastructures are needed. These are discussed in the fourth part. An overview of the envisaged upgrades of the electronics is also provided.

2 Advanced Virgo Design

The scope of this section is to give a summary of the central design features of AdV. Upgrades necessary to convert the Virgo instrument to the AdV detector, are briefly introduced here, while comprehensive and more detailed descriptions can be found in the Section 5 to 16.

Since AdV aims for a sensitivity about a factor 10 better than initial Virgo, most of the detector subsystems have to deliver a largely improved performance to be compatible with the AdV targets. The actual design choices of the AdV baseline design were made taking into account:

- the knowledge and experience gained from the commissioning of first generation gravitational wave detectors;
- the outcomes of the internal review process;
- the constraints from the existing infrastructure and costs;
- the results of the vast R&D programs carried out within the GW community;
- the time constraints from the fact that AdV will join Advanced LIGO in the network of the second generation GW detectors.

In this section we will briefly describe the AdV reference configuration by listing the main features of the AdV design (see also fig. 1). At the end of this section a summary of the relevant design parameters for AdV is given in the tables 1,2.

Interferometer optical configuration (Sec. 5)

- AdV will be a dual recycled interferometer. Beside the standard power recycling, a signal recycling (SR) cavity will be present. The tuning of the SR parameter allows to change the shape of the sensitivity curve and to optimize the detector for a given astrophysical source (fig. 3).
- The recycling cavities are designed to be non-degenerate for higher order optical modes (non-degenerate recycling cavities, NDRC). This design is expected to greatly reduce the interferometer sensitivity to misalignments and thermal effects.
- The coating thermal noise limits the AdV sensitivity in the mid-frequency range. One way to lower its level is to enlarge the spot size on the test masses. Therefore, unlike Virgo, the beam waist will be placed closed to the center of the 3 km Fabry-Perot cavities, resulting in beam radii of 55 mm and 65 mm for the input and end mirrors, respectively.

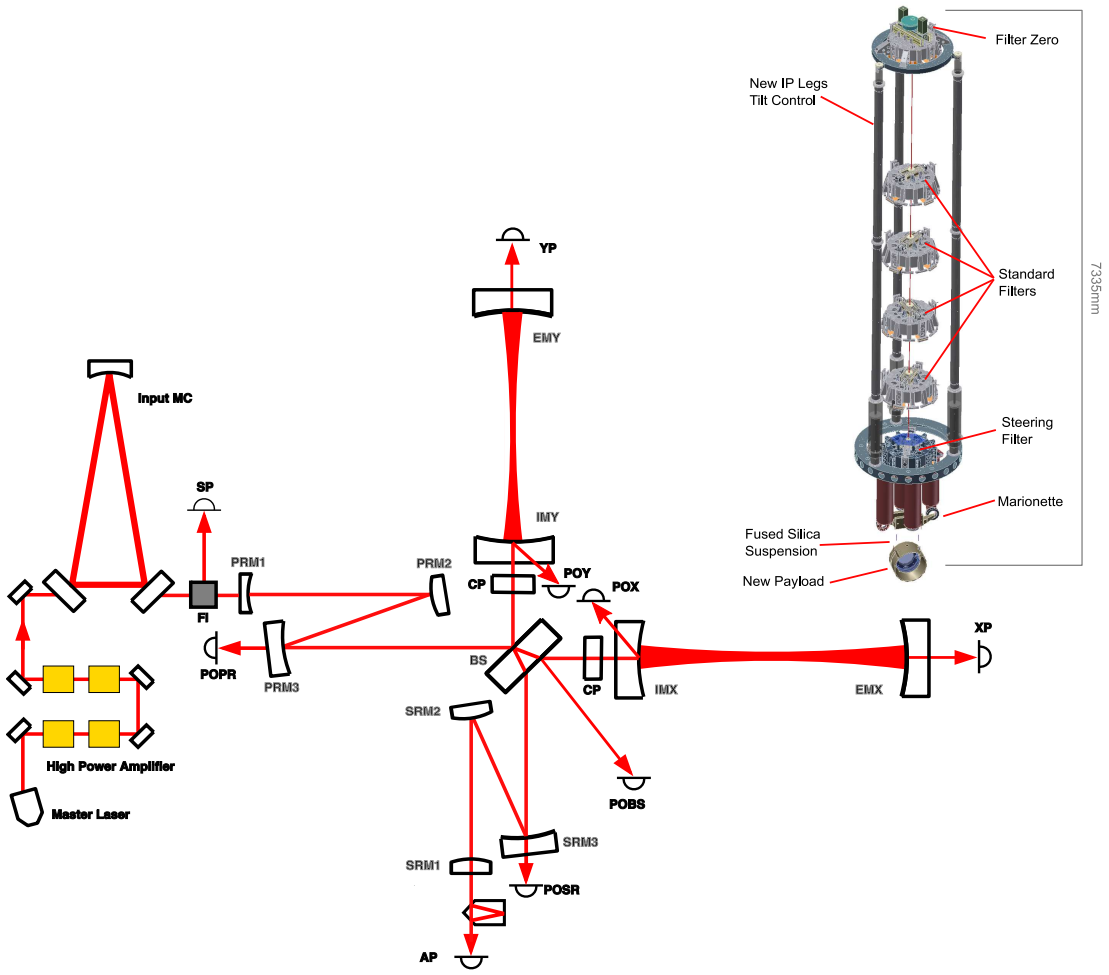

Figure 1: AdV Reference Design. Optical scheme, following the beam from the laser to the dark port: high power laser, triangular input mode cleaner, Faraday Isolator (FI), folded power recycling cavity, beam splitter, compensation plates, 3 km Fabry-Perot cavities, SR cavity, output mode cleaner, dark fringe photodiode. An image of the Virgo superattenuator is shown.

Laser (Sec. 6)

- More laser power is needed to improve the sensitivity at high frequency, where it is shot noise limited. The AdV laser must provide a power of at least 165 W. The design of the high power stage is based on the one developed at LZH for Advanced LIGO.

Injection system (Sec. 7)

- The input optics for AdV must be compliant with the 10 times increased optical power. Proper electo-optic modulators and Faraday isolators are being developed.
- The Virgo configuration for the input mode cleaner (144m long triangular cavity) will be kept.
- With the use of non-degenerate power recycling cavity the injection bench will host one of the power recycling cavity mirrors (PRM1).

Mirrors (Sec. 8)

- Given the much larger optical power in the cavities, radiation pressure noise becomes a limit in the low frequency range and heavier test masses are needed to reduce it. The mirrors designed for AdV have the same diameter as the Virgo ones (35 cm) but are twice as thick (20 cm) and heavy (42 kg).
- A large R&D effort is being carried out in the GW community to produce coatings with lower mechanical losses (an thus less thermal noise). The coating of the AdV mirrors is expected to start in 2011: new R&D results achieved by then might lead to a further improvement of the AdV sensitivity (see sec. 3).

Thermal compensation (Sec. 9)

- Thermal effects (originating from light absorption) create wavefront distortion that can spoil the interferometer dynamics. Such effects, visible even in Virgo and LIGO, might become dramatic in AdV and must be compensated for.
- The AdV Thermal Compensation System (TCS) consists of a combination of CO_2 laser projectors acting on dedicated compensation plates and ring heaters acting directly onto the test masses.

Detection (Sec. 10)

- AdV will use a DC detection scheme, which improves the quantum noise and eliminates some technical noises (such as RF phase noise) which would be (close to) limiting the detector sensitivity in case of heterodyne readout.

- The main photodiodes will be placed on the suspended detection bench (in vacuum) to improve the rejection of seismic and acoustic noise.
- With the use of non-degenerate signal recycling cavity, the matching telescope will no more be hosted on the detection bench. Instead, the bench will host one of the signal recycling cavity mirrors (SRM1).

Interferometer sensing and control (sec. 11)

- An extended *Variable Finesse Technique*, successfully tested in Virgo, will be used to achieve the full lock. The reference solution for the lock of the high finesse Fabry-Perot cavities foresees an auxiliary laser for which the arm cavity finesse is much reduced. Possible sets of modulation frequencies and cavity lengths have been defined (requiring to move the towers in the central building).

Vibration isolation (Sec. 12)

- The seismic attenuation provided by the Virgo superattenuator (SA) is compliant with the AdV sensitivity. The only important upgrade planned is the implementation of a tilt control at the base of the inverted pendulum: this will allow us to control the inertial platform in 6 degrees of freedom, increasing the detector robustness in windy days.

Payloads (Sec. 13,13.5)

- The payloads will be modified to be compliant with the thicker and heavier mirrors.
- In the NDRC baseline scheme the BS payload must suspend two extra mirrors (PRM2/SRM2).
- In the NDRC baseline scheme the mirrors PRM1/SRM1 are suspended in the injection/detection towers respectively and proper payloads will be developed for the purpose.

Vacuum (Sec. 15)

- The current Virgo vacuum level needs to be improved by a factor of about 100 in order to be compliant with the AdV sensitivity. Such improvement requires to bake out the pipes. To separate the pipes from the towers and allow the bakeout, cryotraps will be installed.
- Vacuum links with a larger diameter are needed in the central area, to allow for the larger size of laser beam and for the folded path in the non-degenerate recycling cavities. The links will also have different lengths to meet the new requirements on the position of the towers set by the interferometric sensing and control subsystem.

Infrastructure (Sec. 16)

- To reduce the influence of anthropogenic noise some noisy machines will be either replaced with more silent ones, seismically and acoustically isolated or moved out of the experimental halls.

AdV Overview, Part I		
Subsystem and Parameters	**AdV Baseline Design**	**Initial Virgo Implementation**
Sensitivity		
Binary Neutron Star Inspiral Range	145 Mpc	11 Mpc
Anticipated Strain Sensitivity	$3.5 \cdot 10^{-24}/\sqrt{\text{Hz}}$	$4 \cdot 10^{-23}/\sqrt{\text{Hz}}$
Instrument Topology		
Interferometer	Michelson	Michelson
Power Enhancement	Armcavities and Power Recycling	Armcavities and Power Recycling
Signal Enhancement	Signal Recycling	n.a.
Laser and Optical Powers		
Laser Wavelength	1064 nm	1064 nm
Optical Power at Laser Output	>165 W	20 W
Optical Power at Interferometer Input	125 W	8 W
Optical Power at Test Masses	760 kW	6 kW
Optical Power on Beam Splitter	2.7 kW	0.3 kW
Test Masses		
Mirror Material	Fused Silica	Fused Silica
Main Test Mass Diameter	35 cm	35 cm
Main Test Mass Weight	42 kg	21 kg
Test Mass Surfaces and Coatings		
Coating Material	Ti doped Ta_2O_5	Ta_2O_5
Roughness	< 1 Angstrom	< 0.5 Angstrom
Flatness	0.5 nm RMS	< 8 nm RMS
Losses per Surface	37.5 ppm	250 ppm (measured)
Test Mass ROC	Input Mirror = 1416 m End Mirror = 1646 m	Input Mirror = flat End Mirror = 3600 m
Beam Radius at Input Mirror	56 mm	21 mm
Thermal Compensation		
Thermal Actuators	CO_2-Lasers and Ring Heater	CO_2-Lasers
Actuation Points	Compensation Plates and directly at Mirrors	Directly at Mirrors

Table 1: Main parameters of the AdV Baseline Design (PART 1)

AdV Overview, Part II		
Subsystem and Parameters	**AdV Preliminary Design**	**Initial Virgo Implementation**
Suspension		
Seismic Isolation System	Superattenuator	Superattenuator
Degrees of Freedom of Inverted Pendulum Inertial Control	6	4
Suspension Fibres	Fused Silica Fibres (optimized geometry)	Steel Wires
Vacuum System		
Pressure	$2 \cdot 10^{-9}$ mbar	$2 \cdot 10^{-7}$ mbar
Injection System		
Input mode cleaner throughput	>90%	85% (meas.)
Detection System		
GW Signal Readout	DC-Readout	Heterodyne (RF)
Output Mode Cleaner Suppression	RF Sidebands and Higher Order Modes	Higher Order Modes
Main Photo Diode Environment	in Vacuum	in Air
Lengths		
Arm Cavity Length	3 km	3 km
Input Mode Cleaner	144 m	144 m
Power Recycling Cavity	28 m	10 m
Signal Recycling Cavity	28 m	n.a.
Interferometric Sensing and Control		
Lock Acquisition Strategy	Auxiliary Lasers (different wavelength)	Main Laser
Number of RF Modulations	3	1
Schnupp Asymmetry	4 cm	85 cm
Recycling Cavity Design	Non-degenerate	Marginally stable
Signal Recycling Parameter		
Signal Recycling Mirror Transmittance	11 %	n.a.
Signal Recycling Tuning	0.15 rad	n.a.

Table 2: Main parameters of the AdV Baseline Design (PART 2).

3 Sensitivity

3.1 The AdV reference sensitivity

The AdV reference sensitivity[1] as well as the main noise contributions are shown in fig. 2. The curve is calculated using the parameters in tables 1,2. The SR parameters have been chosen in order to maximize the sight distance for Binary Neutron Stars (BNS) [6]. The corresponding inspiral ranges are $\sim$ 150 Mpc for BNS and $\sim$ 1.1 Gpc for 10 $M_{\odot}$ Binary Black Holes (BBH).

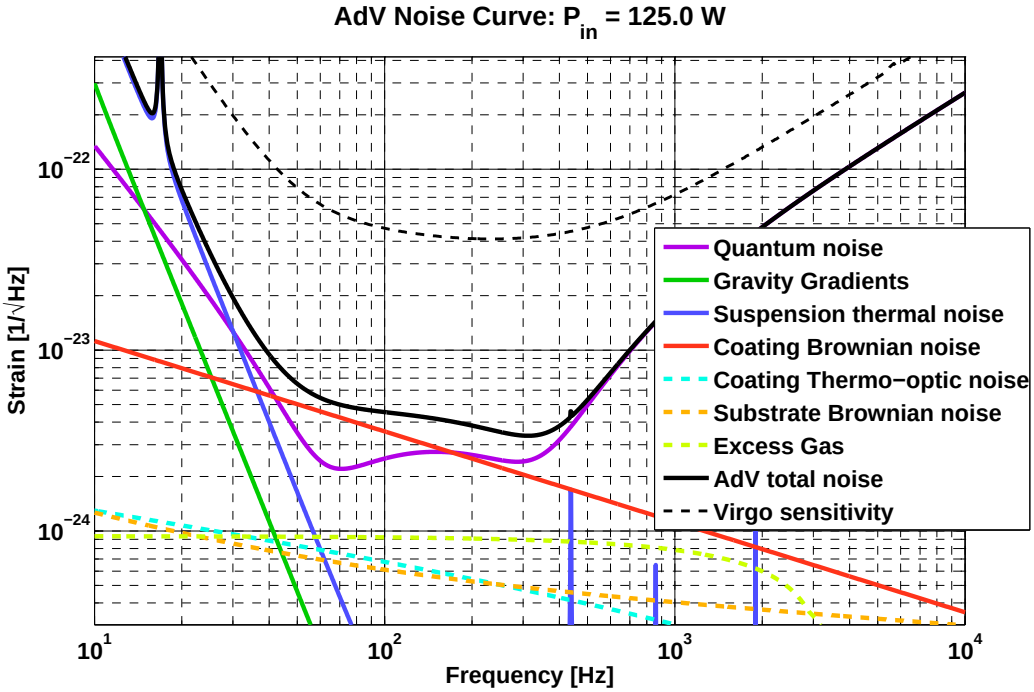

Figure 2: Reference AdV sensitivity and expected noise contributions. It has been calculated with SR mirror transmittance of 11% and SR phase of 0.15 rad, 125 W of laser power entering the interferometer, cavity finesse of 888 and PR factor of 21.5. The chosen SR tuning optimizes the inspiral range for coalescing binary neutron stars. The Virgo design sensitivity is shown for the sake of comparison.

As already mentioned, the presence of the SR cavity allows to think of AdV as a tuneable detector (see Section 5.4): the sensitivity curve can be shaped in order to optimize it for targeting different astrophysical sources. The SR mirror transmittance influences the detector bandwidth, while the microscopic lenght of the SR cavity changes the frequency of the maximal sensitivity.

Fig. 3 shows some examples of sensitivity curves obtained with different tunings. With respect to the reference sensitivity (optimized for BNS) one can:

[1] The sensitivity curves shown in this section have been plotted using the MATLAB *GWINC* code developed within the LSC [7] and adapted to AdV [8]. Documentation on all sensitivity options shown in this section can be found in [9].

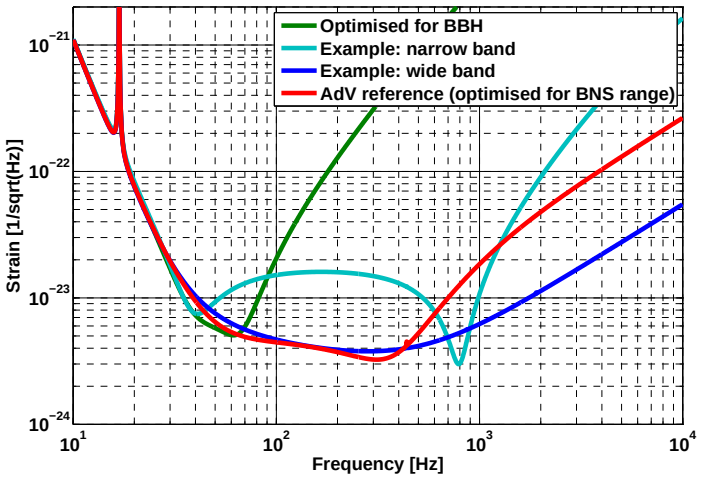

Figure 3: Tuning the AdV sensitivity by changing the SR parameters. The red curve corresponds to the reference sensitivity of fig. 2 and maximizes the inspiral range for BNS. The green curve is optimized for BBH detection (BH of 10 $M_\odot$ are considered) and is obtained with a low input power (9 W). The cyan curve shows a narrow band tuning, useful to target a monochromatic source, while the blue "wide-band" tuning allows to improve the high frequency sensitivity .

- enhance the low frequency response in order to increase the detectability of large mass BBH (green curve in fig. 3). This also requires lowering the input power;
- enhance the sensitivity in a certain frequency range, *narrow banding* the response (cyan curve in fig. 3). This is indicated to target young pulsars;
- widen the detector response and increase the high frequency sensitivity for burst search (blue curve in fig. 3).

3.2 Sensitivity and detector commissioning

Reaching the AdV design sensitivity will require several progress steps. The presence of the SR cavity and the tenfold laser power increase are features that require the commissioning team to face new problems. The commissioning will certainly start in a low power configuration and the power will be then increased gradually, as the understanding of the detector improves and the control becomes more robust. It is also possible to start the commissioning without the SR mirror, in a configuration more similar to Virgo/Virgo+, though such choice will require to use a different control scheme.

Independent of the commissioning strategy, it is remarkable that, even in a preliminary configuration (in low power with SR or in high power without SR) AdV can reach a sensitivity allowing to take interesting science data. Fig. 4 compares the sensitivity curves achievable in the different commissioning scenarios, while in table 3 we list the

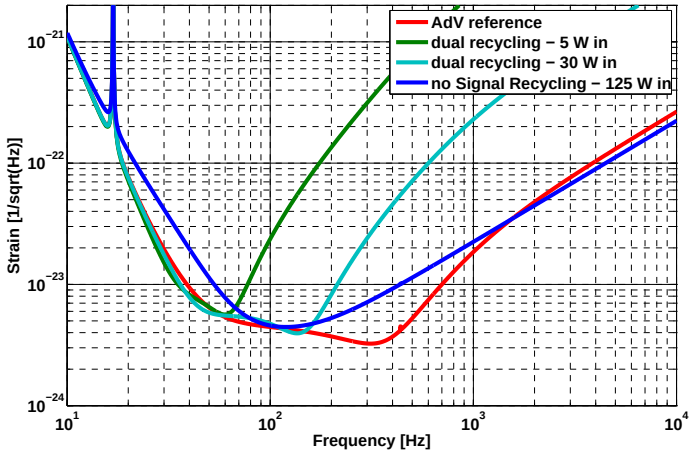

Figure 4: The AdV reference sensitivity (red) is compared with the ones achievable in the following cases: dual recycled 5W power in (green), dual recycled 30W power in (cyan), power recycled 125 W power in (blue).

inspiral range for BNS and BBH and the sensitivity at 1 kHz achievable in the various configurations described so far. It is remarkable that with 30 W of laser power in the interferometer (more or less the Virgo+ input power) one can achieve target BNS at about the same distance as the reference sensitivity, with slightly better sensitivity for BBH, at the cost of a bad response in the high frequency range. This suggests that AdV can be thought as a flexible detector with a high science potential even in a non complete configuration.

FIG. of MERIT	**BNS range (MPc)**	**BBH range (Mpc)**	h**@1 kHz** ($1/\sqrt{\text{Hz}}$)
Virgo (design)	11	58	7.2e-23
AdV BNS opt. (reference, fig. 2)	145	1112	1.8e-23
AdV BBH opt. (green in fig. 3)	108	1276	3.2e-21
AdV broadband (blue in fig. 3)	134	987	6.2e-24
AdV dual rec. 5W in (green in fig. 4)	98	118	2.5e-21
AdV dual rec. 30W in (cyan in fig. 4)	132	1216	2.3e-22
AdV no SR. 125W in (blue in fig. 4)	107	643	2.2e-23

Table 3: The inspiral range for BNS and BBH and the strain sensitivity at 1 kHz for Virgo and some possible AdV configurations.

4 Advanced Virgo science case

This section addresses some of the scientific motivations for the realization of AdV, listing its main astrophysical targets, the potentialities for discovery and science, and the opportunities for collaborative work with other GW detectors, as well as with other observatories of e.m. and ν radiation.

4.1 Generalities

The AdV detector has the goal to contribute bringing the gravitational waves into maturity, by achieving an improvement in sensitivity of about a factor of 10 or better with respect to the initial Virgo design sensitivity.

AdV will harvest its scientific potential thanks to the close collaboration with the Advanced LIGO detectors, constituting a long baseline network of observatories, capable to coherently exploit the time, amplitude and phase information coming from the different sites, thus reconstructing the source position, the polarization of the impinging waves, ultimately giving access to the physics of the sources.

In Sec. 4.2 we will translate the AdV sensitivity into scientific potential for the different sources; these estimates are illustrative of the instrument capabilities. Then in Sec. 4.3 we discuss how these capabilities contribute to the AdV - Advanced LIGO network as a whole. Finally in Sec. 4.4 we will address the importance and the potentialities of a multi-messenger approach to astrophysical phenomena, in collaboration with other instruments, sensitive to e.m. and neutrino signals.

Sensitivities: a choice We show in Fig. 5 a comparison of the AdV sensitivity, of the Virgo sensitivity, and of two possible sensitivity curves for the intermediate step, Virgo+, currently under commissioning. As discussed in Sec. 3 the AdV sensitivity is tunable, to optimize the detection probability for different sources. We will make the simplification of considering only a "BNS optimized" curve as the basis for quantitative considerations.

In the following, for some of the interesting GW sources, we try to list the scientific motivation and the chances of detecting or placing interesting upper limits.

4.2 Scientific potential

We list here briefly the sources which can be of interest for AdV, and provide when possible estimates of the source strength or the rate.

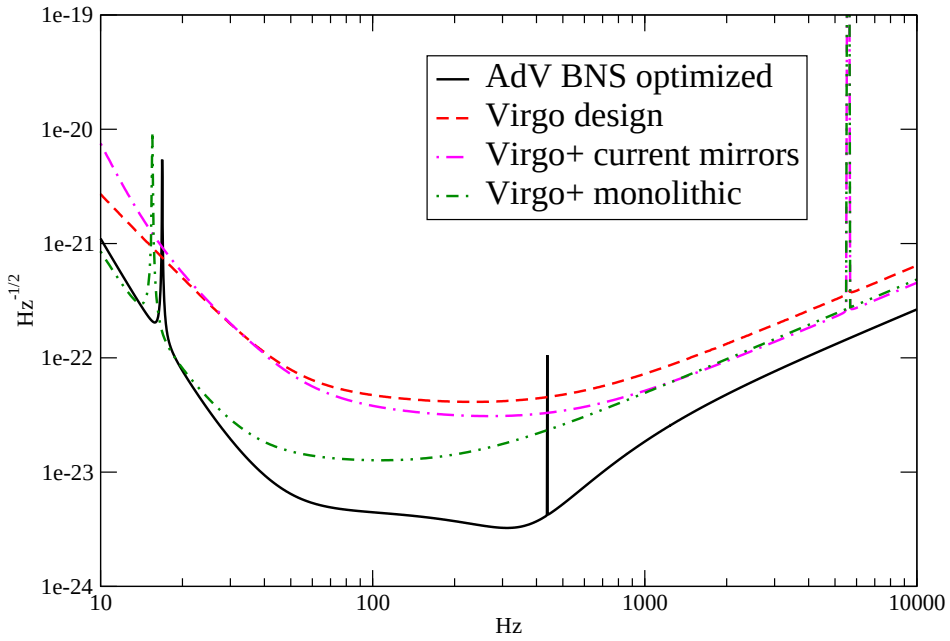

Figure 5: Comparison of AdV sensitivity with the design sensitivity of Virgo and Virgo+. The "BNS optimized" is representative of a range of possible sensitivity tunings. We show Virgo+ curves in two different configurations, which include or not a subset of AdV technical solutions.

4.2.1 Binary neutron stars

A "compact binary coalescence" (CBC) is the best known event leading to copious production of gravitational waves; it is conventionally divided in three phases:

inspiral during which the orbit shrinks adiabatically and the signal is modeled with a post-newtonian expansion;

merger which marks the collision of the compact objects;

ringdown characterized by oscillating, decaying signals emitted by the resulting object.

It is a very effective source; during the inspiral phase alone, it emits in GW's an energy[2]

$$\Delta E_{rad} \simeq 4.2 \times 10^{-2} M_{\odot} c^2 \left(\frac{\mathcal{M}}{1.21 M_{\odot}}\right)^{5/3} \left(\frac{f_{max}}{1\mathrm{kHz}}\right)^{2/3} . \quad (1)$$

The existence of binary neutron stars is well attested by the observation of pulsars in binary systems, for which mass parameters have been estimated, with values close to $1.4\mathcal{M}_{\odot}$.

[2] Here we introduce the chirp mass $\mathcal{M}$ defined as $\mathcal{M} = \mu^{3/5} M^{2/5}$ in terms of the total mass $M \equiv m_1 + m_2$ and the reduced mass $\mu \equiv \frac{m_1 m_2}{M}$ of the binary system. We introduce as well f_{max}, the GW frequency at the end of the inspiral phase.

Scientific payoff of BNS detections A number of consequences would stem from a direct BNS detection;

- GW emissions explain the rate of orbital period variation in binary NS. However, a detection of GW waves from the inspiral phase would be a very clean, direct confirmation of GR;
- a network of detectors allows to reconstruct the waveform amplitude, a known function of source distance and binary masses; the masses though can also be extracted by the time evolution of the waveform. Hence a BNS event distance can be reconstructed, and if the event can be associated with an astrophysical object, it will serve as distance calibration, thus potentially competing with other methods for determining the Hubble constant.
- the merger phase is expected to emit GWs dependent on the details of the NS structure, including the Equation of State (EoS) of the nuclear matter in the neutron star.[3]
- the ringdown phase of the resulting BH, characterized by the emission of waves corresponding to the quasi-normal-modes of the system, will give direct access to mass and spin parameters of the BH.

A non-detection of BNS events would not violate strongly the astrophysical expectations; however, a non-detection by the LSC-Virgo network over several years of observation would strain the models quite.

Expected rate of events There are basically two ways by which astrophysicists can predict the number of BNS events: empirical, based on a few observations of compact binary systems which will coalesce on a timescale comparable with the age of the Universe; and theoretical, based on models of binary star formation and evolution.

For a recent account of the results of the empirical method, the reader is referred to [10]; on the basis of the observations, corrected for selection factors linked to the fact that we only see binary systems in which at least one component is a visible pulsar, quotes a rate range $\mathcal{R}_{emp} \in 3 - 190\mathrm{Myr}^{-1} \times \mathrm{MWEG}^{-1}$, where MWEG stands for Milky-Way Equivalent Galaxy.

The theoretical models display different cases, depending on assumptions about the dominant channel by which a pair of massive stars evolves into a pair of close compact objects, surviving two supernova explosions without being disrupted, and whether during a common envelope phase the binary system undergoes instead a premature merger as a result of friction.

The reader is referred to [11] for an example of the comparison of different models, and the resulting recent re-estimate of the rates; the authors introduce several models, two of which (A and B) are more pessimistic, since they assume that binaries in a common

[3] Given the complexity of the system though, and the expected weakness of the merger signal in BNS, it is likely that more can be learned about the NS EoS in BH-NS collisions (see below).

envelope phase are more likely to undergo a premature merger; the third model (C) instead allows for survival of stars in the Hertzsprung gap (HG) through the CE phase and leads to larger estimates.

For BNS systems, model A predicts galactic merger rates $\mathrm{R}_A \in [12-19]\mathrm{Myr}^{-1}$; model B is slightly more pessimistic, with rates in $\mathcal{R}_B[7.6-12]\mathrm{Myr}^{-1}$, while model C is markedly more optimistic, with rates $\mathcal{R}_C \in [68-101]\mathrm{Myr}^{-1}$.

The range of variability of the results within each theoretical model depends also on the way they are calibrated, either by means of assumptions about the star formation rate, or by means of the rate of supernova events in a Milky Way type galaxy; low rates are obtained with star formation calibration, high rates with supernova calibration.

The wide range of models available in the literature has been taken into account into a summary document made available by the LSC-Virgo CBC group [12]; the realistic NS-NS rate value is expected to be $\mathcal{R}_{re} \simeq 50\mathrm{Myr}^{-1}\mathrm{MWEG}^{-1}$, but models allow this figure to vary by one order of magnitudes above and below.

The other ingredient for estimating the rate of detectable events is the density of MWEG, which can be assumed to be

$$\rho_{gal} \simeq 0.01\mathrm{Mpc}^{-3}. \tag{2}$$

For BNS events, the detection range is sufficiently close not to require correcting this density to take into account cosmological effects.

Finally, we need to estimate the distance up to which AdV can be expected to detect BNS signals; to this end, we rely only on the accurate knowledge of the BNS waveform in the inspiral phase[4].

The signal to noise ratio (SNR) of an optimal oriented source in the inspiral phase can be written as

$$\begin{aligned}\mathrm{SNR} &= \sqrt{4\int_0^{f_{Nyquist}} \frac{|\tilde{s}(f)|^2}{S_n(f)}df} = \frac{(G_N\mathcal{M})^{5/6}}{r\,c^{3/2}\,\pi^{2/3}}\left(\frac{5}{6}\right)^{1/2}\sqrt{\int \frac{f^{-\frac{7}{3}}}{S_n(f)}df} \\ &= 1.56\times10^{-19}\left[\frac{\mathcal{M}}{M_\odot}\right]^{5/6}\left[\frac{\mathrm{Mpc}}{r}\right]\sqrt{\int_0^{f_{upper}} \frac{f^{-\frac{7}{3}}}{S_n(f)}df}\,,\end{aligned} \tag{3}$$

The actual value of the f_{upper} beyond which the merger begins is somewhat model dependent; a conservative value is given by the so called "innermost stable circular orbit", ISCO, which at the lowest order in the PN expansion can be written as

$$f_{ISCO} \simeq \frac{4.4\mathrm{kHz}}{(M/M_\odot)}\,. \tag{4}$$

[4] It should be made clear though, that significant GW signal is expected also in the merger phase and the subsequent ringdown of the formed object; targeting these signals is foreseen in data analysis, and should increase the detectability of the event. We omit this effect because we are unable to size it quantitatively at the same level of accuracy possible for the inspiral phase

Detector	sight distance (Mpc)	detection rate (yr^{-1})	comments
Virgo	12.4	4×10^{-3}	design sensitivity
Virgo+ (CM)	16.8	10^{-2}	current mirrors
Virgo+ (NM+MS)	59.4	0.4	new mirr. + mon. susp.
AdV	155	8	BNS optimized

Table 4: Realistic rate of BNS events for the Virgo detector at different stage of its upgrade towards Advanced Virgo. These figures might easily be wrong by one order of magnitude.

Given the SNR expression, we can define a sight distance d_{sight} as the distance at which AdV would detect, exploiting solely the inspiral phase, an event with an SNR=8[5].

The sight distance results to be

$$\frac{d_{sight}}{1Mpc} = \frac{1}{2.26} \times 1.95 \times 10^{-20} \left[\frac{\mathcal{M}}{M_\odot}\right]^{5/6} \sqrt{\int_0^{f_{ISCO}} \frac{f^{-\frac{7}{3}}}{S_n(f)} df}\,, \tag{5}$$

where the factor $\frac{1}{2.26}$ accounts for an average over source location and polarization, leading to a reduction of the SNR value as compared with the optimally oriented one. For a BNS, one has $\mathcal{M} \simeq 1.219 M_\odot$, and $f_{ISCO} \sim 1.4$kHz; in AdV, the resulting sight distance is of $\simeq$ 155Mpc; the resulting volume observable by AdV alone is therefore $V_{BNS} \simeq 15.6 \times 10^6 \mathrm{Mpc}^3$.

In Tab. 4, for the various stages of the Virgo detector, we report the sight distances and the expected detection rates, on the basis of the simple formula

$$\rho = V_{BNS} \times \mathcal{R}_{MW} \times \rho_{gal} \tag{6}$$

where $\mathcal{R}_{MW}$ is the merger rate in a "Milky Way equivalent galaxy". It should be noticed that the authors [11] quote about 8 times larger rates for AdLIGO; the reason is that they assume a detection range of Advanced LIGO of $\sim$ 300 Mpc, which results by using coherently the three AdLIGO detectors, each having a sight distance of about 170Mpc.

Let us anticipate here what we will discuss in Sec. 4.3; adding coherently AdV to the Advanced LIGO network leads of course to even larger detection range, and rates increased by about 40%, but more importantly allows to solve the inverse problem, locate the source position and reconstruct its polarization.

4.2.2 Binary black holes, and mixed systems

Differently from BNS, no BH-BH or BH-NS system has been observed yet; consequently, the assumptions about the coalescence rate of such systems is somewhat less firm. However, since the SNR scales roughly as $M^{5/6}$, larger mass systems are potentially visible to greater distances and their interest is quite substantial.

[5] This value was conventionally assumed as safe for a detection, but experience has shown that actual detectors may yield spuria well above this limit, depending on the quality of the detector noise.

Scientific payoff Some of the considerations made for BNS events apply also to BBH and BH-NS events, in particular the possibility to measure the event distance, and actually to much larger distances.

The BH-BH collisions will be a unique laboratory; each BH is solely characterized by its mass and spin, which completely determine the dynamic of the event horizon, and a BH-BH collision can be studied by methods of Numerical Relativity, and yield accurate predictions about the waveforms. This program has met in the past enormous difficulties, which have been in large part overcome ingenuously [13, 14] and start to yield complete predictions about the waveforms: see for instance [15].

A direct BBH observation would be a clean test of GR in a regime of strong fields, thus allowing for instance to discriminate alternative formulations of GR.

The BH-NS collisions have instead a good potential to shed light on the EoS of the NS; for a wide range of mass parameters, the latter will be disrupted by the tidal forces due to the BH, and the resulting GWs will be within the frequency range of GW detectors, thus allowing a direct probe of the NS structure [16].

It should also be noticed that BH-NS coalescences are one of the proposed mechanisms for producing the violent shocks that would generate Gamma Ray Burst events; the importance of collaborating with GRB detectors is paramount.

We will see that a non detection of BH-NS events would generally be compatible with current models of stellar evolution. Instead, a non detection of massive BBH events would challenge the theoretical expectations, and lead to revise substantially the models.

Expected rate of events There are essentially two ways by which a population of BBH or BH-NS systems can be inferred. First, it is possible to use the same population synthesis models applied to the BNS systems, and partially calibrated by the observation of binary pulsars, to infer the population of more massive stars [11].

Second, it is possible to exploit a unique observation, the one of a single binary system formed by a Wolf-Rayet massive star and a black hole, the IC10 X1, to infer the rate of BBH production, on the basis of the assumption that the WR star will soon evolve into a BH [17].

Rate based on population synthesis models The population synthesis models discussed in [11] display for BBH the same variation of the results, internal within each model and across models, that we have discussed for the BNS sources.

The more pessimistic model A predicts for pairs BH-NS galactic merger rates of $0.07 - 0.11\mathrm{Myr}^{-1}$, while for BBH systems it predicts chirp masses in the range $[4, 8]M_{\odot}$ and galactic merger rates in $[0.02 - 0.03]\mathrm{Myr}^{-1}$.

These values are to be compared with those resulting from the more optimistic model C, which assumes a more favorable evolution of the binary system through the common-

Model	$\mathcal{M}/M\_\odot$ range	$d_{eff-sight}$Mpc	merger rates Myr^{-1}	AdV det. rate yr^{-1}
A	$2.5-3$	300	$0.07-0.11$	$0.08-0.12$
C	$1.5-4$	286	$3.2-4.8$	$3.1-4.7$

Table 5: BH-NS results from population synthesis models

Model	$\mathcal{M}/M\_\odot$ range	$d_{eff-sight}$Mpc	merger rates Myr^{-1}	AdV det. rate yr^{-1}
A	$5-8$	613	$0.02-0.03$	$0.2-0.3$
C	$2.5-8.5$	545	$7.7-11$	$52-75$

Table 6: BBH results based on population synthesis models

envelope phase: for BH-NS sytems, galactic merger rates in $[3.2-4.8]\mathrm{Myr}^{-1}$, and for BBH systems galactic merger rates in $[7.7-11]\mathrm{Myr}^{-1}$ result.

In order to turn the galactic merger rates into predictions for AdV detection rates, the following crude formula can be adopted

$$R = \rho_{gal} \times \frac{4\pi}{3} d^3_{eff.sight} \times \mathcal{R}_{MW} \tag{7}$$

where the $d^3_{eff.sight}$ is an effective volume scale, reminiscent of a sight distance but which takes into account a population averaging. The authors of [11] scale the sight distance d_{BNS} by the factor $(\mathcal{M}/M_\odot)^{5/6}$ in Eq.5, then average the volume factor d^3 over the synthetic mass population[6]. This scaling can be roughly carried over on the AdV estimation, and we report the resulting effective sight distance in Tab. 5, 6.

To compute the last column of Tab. 5, 6 we again assume $\rho_{gal} \sim 0.01\mathrm{Mpc}^{-3}$, neglecting cosmological effects which start to be relevant for BBH systems. Again, the results we obtain are, not surprisingly, about 8 times smaller than the AdLIGO network, which we should remind comprises three equal detectors located at two sites, each with a sensitivity for BNS $d_{sight}(BNS) \sim 174$ Mpc. This scale alone boosts the observable volume, over AdV, by a factor $\sim (174/155)^3 = 1.4$. The estimates in [11] assume coherent analysis over the LIGO detectors, which scales up the sight distance by about a factor $\sqrt{3}$, and therefore boosts the observable volume by another factor ~ 5; together the two effects fully justify the factor 8 in the rates.

Besides the large variability of the models, which calls for caution by itself, another potential pitfall of population synthesis models is that they are not extended easily to higher masses, essentially because very large mass stars have a tremendously complex evolution, marked by explosive events and very large mass losses over short periods. However, as we will shortly see, larger mass systems might be a very interesting target.

[6] Please note that this estimate does not take into account the upper frequency cutoff at f_{ISCO}, see Eq.4; however, this effect can be neglected for the AdV sensitivity curve and for the range of masses simulated by the authors

Rate based on empirical observations Besides the systems simulated by binary evolution codes, there exist a very few but tremendously important observations of very massive binary systems, which lead to believe that high mass BH pairs are actually formed and are detectable by Advanced GW detectors.

In particular, the IC10 X-1 X-ray source is a binary tight system comprising a $24M_{\odot}$ BH (the largest known stellar BH) and a $35M_{\odot}$ Wolf-Rayet star, whose future evolution has been studied in depth in [17]. The authors predict that the system will evolve in a BH pair with a chirp mass $\mathcal{M} \sim 14M_{\odot}$; systems with such a mass are detectable by AdV up to about 1.1 Gpc.

The other important prediction in [17] is that the system will remain tight enough to coalesce in a few billion years. The authors are able to estimate the abundance of such systems and predict a rate of detection, for the three combined Advanced LIGO detectors, of 2300 events / year. Even AdV alone would see about 250/year events of this kind.

4.2.3 Rotating neutron stars

A rotating compact object, like a NS, distorted so as to possess a variable mass quadruple moment, would emit essentially monochromatic GW radiation, with a stability comparable to the one of the rate of pulsar electro-magnetic pulses.

The strength of the GW signal is essentially parametrized by the degree of asymmetry of the star, the so called "ellipticity" parameter ε; a typical estimate for the gravitational strain at Earth could be

$$h \sim 10^{-26} \frac{I}{10^{38} Kgm^2} \frac{10kpc}{d} \left(\frac{\nu}{100Hz}\right)^2 \frac{\varepsilon}{10^{-6}}. \quad (8)$$

where 10^{-6} is at the upper range of what is believed plausible for a neutron star, while "strange stars" might sustain higher asymmetries, even as large as 10^{-4}.

The weakness of the signal, and the need to integrate it over O(1yr) periods, lead to data analysis complications, due to the Doppler effect and the resulting line widening; however, the signal remains conceptually relatively simple and provides a clean laboratory for GW study.

Scientific payoff The detection of continuous GW signals from galactic pulsars would be a tremendously clean test of GR.

The strength of the signal is proportional to the ellipticity parameter ε, and this in turn to the rigidity of the NS crust.

For pulsars, the relationship between the GW emission frequency and the rate of e.m. pulses would help discriminating among competing mechanisms generating this asymmetry.

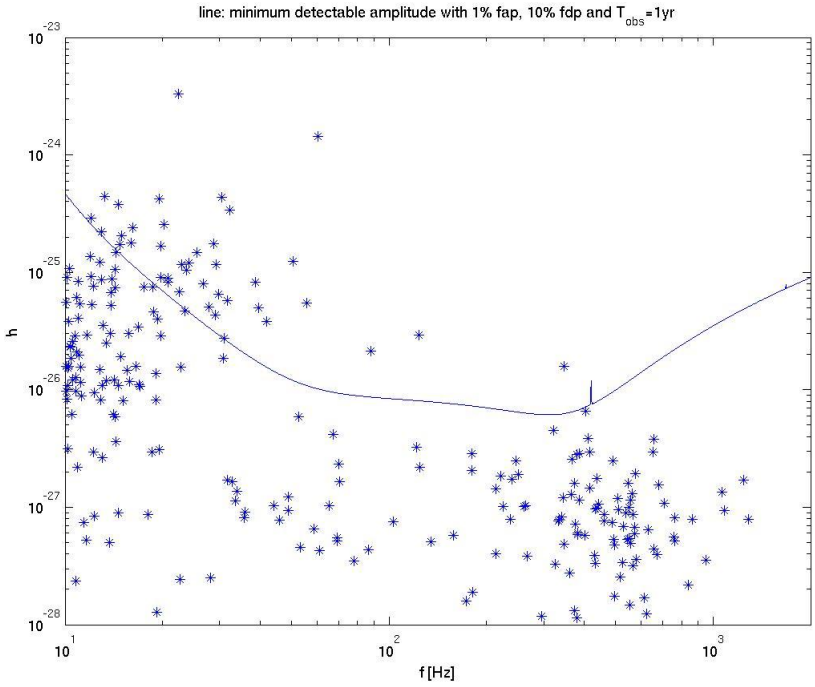

Figure 6: The curve shows the minimum value of h detectable by AdV, assuming a 1% false alarm rate, a 10% false dismissal rate, and an observation time (integrated) of 1 year. The dots represent the h value corresponding to the hypothesis that all the pulsar braking is due to GW emission.

Moreover, it is well known that pulsar rotation may undergo sudden phase discontinuities, believed to be related to "starquakes", or rearrangements of the NS crust stresses. If such events could be related with analogous losses of phase coherence in the GW signals, this observation could shed light on the nature of the deformation and ultimately on the rich physics of these stars, which possess huge magnetic fields and are believed to contain a superfluid core.

Known pulsars The Doppler effect due to Earth rotation and revolution can be fully corrected for known pulsars, for which position and frequency are sufficiently known; for these sources, it is possible to estimate the chances for AdV of detection.

In Fig. 6 we show the minimum value of h that AdV can detect with 1 year of integrated observation, and the assumption of 1% false alarm and 10% false dismissal probabilities. The dots represent the upper limits to the h values that individual known pulsars can emit, assuming that their loss of rotational energy is entirely due to the GW emission. This is the so called "spin-down limit". The figure shows that even in a configuration optimized for BNS, AdV will be able to beat by orders of magnitude the spin-down limit for about 40 of the pulsars presently known, mostly at low frequencies.

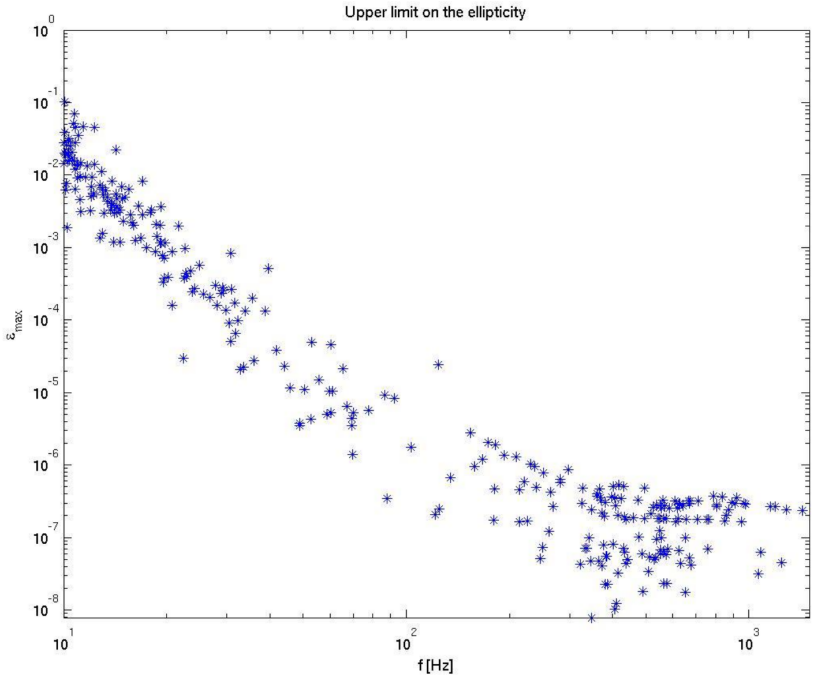

Figure 7: The plot shows the upper limits placed on the ε ellipticity of known galactic pulsars on the basis of 1 year of AdV observation time.

In Fig. 7 we show the upper limits that it is possible to place on the ellipticity ε by exploiting 1 year of AdV observation time, under the same assumptions leading to reach the h_{min} limit discussed. If we believe that the realm of plausible ε values is rather $\leq 10^{-6}$, this clearly reduces somewhat the interest of the low frequency upper limits. However, it is also clear that at higher frequencies it is possible to reach plausible ε values, although it would be necessary operating the detector in SR mode optimized around 1kHz in order to also beat the spin-down limit for some millisecond pulsars.

Unknown rotating neutron stars We detect as pulsars only a tiny fraction of the galaxy NS's; in fact, on the basis of the neutron star birthrate [18] it is possible to estimate that there exist $O(10^5 - 10^6)$ electromagnetically quiet NS in a radius of 1kpc; it makes therefore sense to perform non-targeted searches, at a reduced sensitivity, which may allow to discover close enough NS. The LIGO Scientific Collaboration has recently published a search [19] which uses part of the LIGO S5 run data which has been able to constrain $\varepsilon \leq 10^{-6}$ for the NS in a 500pc radius around Earth. Advanced detectors will improve over these limits: in Fig. 8 we show the distance, as a function of the frequency, at which a rotating compact object could be detected with one year of AdV operation, assuming $\frac{f}{\dot{f}} > 10^4$yr and under the assumption of having 10^9 candidates selected after an uncoherent search, to be followed coherently.

We actually plot a family of curves, corresponding to different values of the "ellipticity" ε,

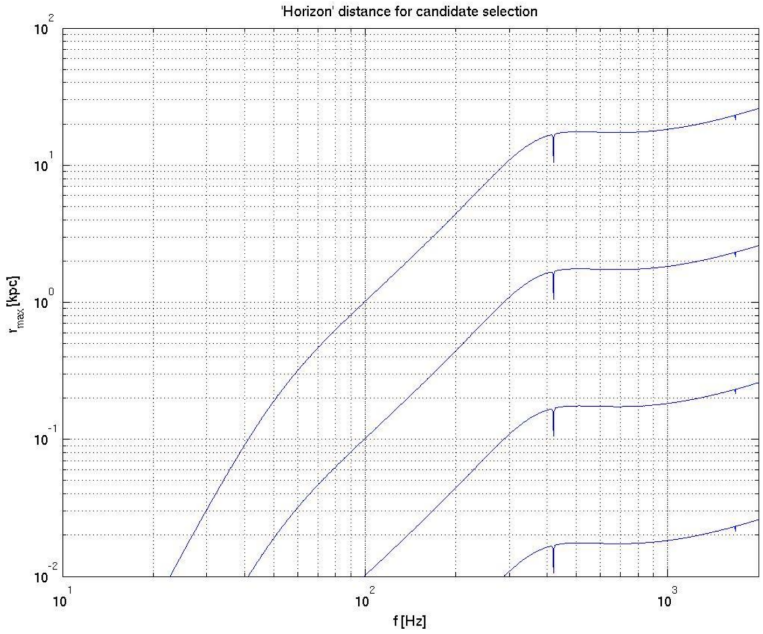

Figure 8: The plot shows the maximum distance at which a distorted, rotating NS could be detected during a non-targeted search, for given values of the ε ellipticity, from 10^{-8} (lower curve) to 10^{-5} (upper curve), on the basis of 1 year of AdV observation time.

from $\varepsilon = 10^{-8}$ (lower curve) up to $\varepsilon = 10^{-5}$ (top curve). It is on one hand clear that even in advanced detectors the uncoherent search will be unable to cover the entire galaxy (distance scales $O(10kpc)$), still the chances of detection will be increased by 2 - 3 orders of magnitude.

Low Mass X-ray binaries We should mention another potentially interesting class of spinning neutron stars; the Low Mass X-ray Binaries, constituted by a NS which is spun-up by the infall of material through an accretion disk. The evidence is that the spin of this systems results from the equilibrium between the torque due to the accretion mechanism and some braking mechanism, the most likely being the GW emission. The resulting GW frequencies are stabilized by this feedback mechanism and are expected in the range 600 - 1200 Hz; these sources could be targeted especially well operating AdV in narrow band mode, except Scorpius X-1 on which interesting limits (or a detection) can be placed also operating in wide-band mode.

4.2.4 Core collapse Supernovae

The collapse of the core of a massive star, the so called Supernova Type II events, has long been considered one of the most interesting sources of GW emission, with optimistic values for the energy emitted in GWs, of the order of $10^{-2}M_{\odot}$, quite comparable to the energy emitted by a BNS coalescence.

More recent estimates of the energy emitted in GWs have shown, though, that the GW energy emitted is likely to be $\leq 10^{-8} M_{\odot}$, and this fact, together with the limited knowledge of the waveform emitted, reduces the prospects of detection by first generation interferometric detectors to galactic events, at best.

Galactic events are known to be rare: the latest galactic supernova observed has been the explosion of the blue star Sanduleak, which led to the famous 1987a event. The estimates of less than 1 event per two decades in the Milky Way and in the local group of galaxies is supported by indirect evidence, provided by the Integral experiment. Integral has detected γ rays emitted in the radioactive decay of the ^{26}Al isotope, copiously produced in Supernova explosions; the galactic abundance of this Al isotope, about $3 M_{\odot}$, is consistent with the supernova rate quoted above [20].

A recent review [21] recalls however that there may be 1 SN occurring about every other year between 3 - 5 Mpc from Earth.

The recent SN 2008bk, which exploded roughly 3.9 Mpc away, is an example SN from this region of space. Initial LIGO and Virgo class detectors had no chances, though, of detecting GWs from SN 2008bk.

Advanced detectors, however, could put some constraints on the GW emission strength, but still would probably not allow detailed GW observations. It is argued that the GW signatures of the neutrino, magneto-hydro-dynamic, and acoustic SN mechanisms may be mutually exclusive and that the mere detection, or, in fact non-detection, of GWs from a nearby SN can constrain significantly the core-collapse explosion mechanism.

It should be added that the standard model for SN core collapse indicates that the burst of neutrinos from the inverse β-decay, leading to the core neutronization and collapse, and the emission of GW radiation, are separated by a very small delay, of a few ms. This opens the way to very tight coincidences between neutrino and GW detectors, that would increase the detection confidence enormously.

An additional time delay between the GW signal and the neutrino flash is introduced during the propagation because of a non-null neutrino mass: this delay can be expressed as [22]

$$\delta t_{prop} = 5.2 ms \frac{d}{10 kpc} \left(\frac{m_{\nu}}{1 eV} \right)^2 \left(\frac{10 MeV}{E_{\nu}} \right)^2 \tag{9}$$

which means that a 1ms accuracy would constrain neutrino masses $< 1 eV$.

The newly formed proto-neutron-star (or black-hole actually, depending on the starting mass) will be in an excited mechanical state, with oscillations that will gradually damp by internal friction and by the emission of GW as well. Some of these oscillations, like those of the so called $r-$modes, can last for months, thus being in principle detectable as a transient source of essentially monochromatic GW radiation.

4.2.5 Soft γ-ray repeaters

Soft gamma repeaters ("SGRs") are X-ray stars that emit bright, repeating flashes of soft (i.e. low-energy) gamma rays. While four SGRs have been identified in our galaxy so far, many other millions almost certainly exist, and a similar number probably exist in every other galaxy. According to the "magnetar" model, SGR are associated to neutron stars (NS) with very intense magnetic fields. The intensity is such that the star crust breaks under accumulated magnetic stress. A hot fireball forms which cools down through the emission of bursts of electromagnetic (EM) radiation. During the crust quake, the star's nonradial seismic modes can be excited, thus leading to emission of a GW burst. Theoretical estimates predict comparable EM and GW energy release (within few orders of magnitude). The best upper-limit on the strength of the GW emission placed with current LIGO data is 10^{45} erg, which is within the range 10^{44}–10^{46} erg for the observed EM emission. With a sensitivity improvement by a factor of 10, it is possible to cover this entire range. SGR are thus detectable sources by advanced detectors and if they are not observed, stringent constraints on the underlying model will result from the upper-limits.

At times (though rarely), SGRs undergo "giant flares" during which the emission is dramatically increased with a total energy about a thousand times higher than in a typical burst. This has been the case the 27 December 2004 for SGR 1806-20. Quasi periodic oscillations (QPO) in the tails of the giant flares have been observed. QPO are thought to be driven by the star's seismic modes, the same that are expectedly sources of GW. This information can be used to narrow down the search in the GW spectrum to the observed QPO frequencies, leading to an improvement in sensitivity. For hyperflare events occurring at the time of advanced detector operation, the observable GW energetics at 100 Hz would lie in the range 10^{43} erg, leading to stringent constraints on the magnetar model [23].

4.2.6 Gamma Ray Bursts

The gamma-ray bursts, detected by instrumentation on board satellites, might be originated by shocks in matter rapidly accreting onto newly formed black holes.

The events are divided in two broad classes, a minority of *short* bursts (lasting less than about 2 s) and a majority of *long* ones, lasting anywhere between 2s to several minutes, with an average of 30s duration.

There is mounting evidence (see for instance [24]) that long GRB, or at least those with a softer γ spectrum, are associated with a type of core-collapse supernovae; more precisely the collapse of massive, rapidly spinning Wolf-Rayet stars, which end up in massive Kerr black-holes with accretion disks. Instead, good arguments (see for instance [25]) exist to assert that short bursts are related with coalescing BNS or NS-BH. It has also been argued in the past that NS-BH coalescences could be an alternative mechanism for long γ-ray bursts, although the collapsar model is now favored.

The γ rays would be powered by the accretion disk orbiting around the newly formed

Kerr black hole; a disk, for instance, formed by material resulting by the tidal disruption of part of the two colliding objects, in the case of short GRB's[7].

If the pictures for *short* and *long* gamma ray bursts are correct, GW observatories may be able to detect the GW signal from the inspiral and merger event, or by the supernova explosion respectively. Such events have already been searched for in the data of the first generation detectors (see for instance [26] for a search triggered by a long γ-ray burst), finding no evidence of a correlation.

It should be underlined that for most of the short GRB one has observational evidence, by way of measuring faint X-ray afterglows, that they occur at cosmological distances (for which $z \geq 0.1$), which lowers the chances of detecting the progenitor BNS or BH-NS event by means of first generation detectors.

Advanced detectors will have greater chances, and a confirmed association of GRB and BNS events would have tremendous consequences:

- the GRB trigger could give a greater confidence in the GW event, thanks to the tight time association. The models show that it is necessary to allow only for about 2 minutes before and after the GRB maximum in order to over-cover the time windows where a GW event is expected. Considering a GRB rate ~ 1/day, false alarms can be abated by factors $O(10^6)$. At fixed FA rate, the coincidence with GRB's allows to lower the SNR thresholds applied to GW events, for instance from 7 to less than 6, thus gaining a 60% increase in GW event rate.
- The BNS (or NS-BH) GW event would allow reconstructing the mass parameters of the progenitors, through observation of the inspiral phase, and potentially also the mass and spin parameters of the formed Kerr BH, by observing its Quasi-Normal-Modes; this would serve input for modeling the GRB process and could help understanding the complex dynamics in the accretion disk.
- The GW event would also constrain the distance, thus allowing to precisely calibrate the energy emission.

4.2.7 Cosmological stochastic background

The vacuum fluctuations of the early universe are expected, in the inflationary models, to have been amplified during the inflationary era giving rise also to a stochastic background of gravitational waves.

The models in general foresee a spectral density for these perturbation in form of a power law

$$\Omega_{GW}(f) = \Omega_{f_0} \left(\frac{f}{f_0} \right)^n \tag{10}$$

[7] It is worth recalling that the infall of matter on a BH is about the most efficient mechanism for turning matter in energy, far more efficient than thermonuclear reactions.

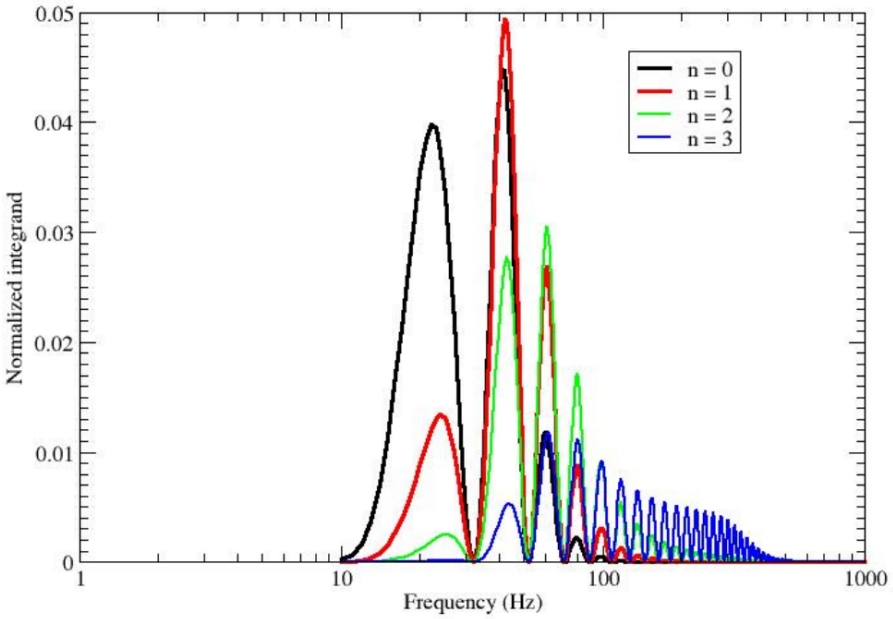

Figure 9: The plot shows, for different values of the power law index, the frequency dependency of the integrand $I(f)$, for AdV and the Hanford Advanced LIGO detector. It is evident how the relative weight of higher frequencies becomes more important for larger n values.

Standard inflationary theory foresee a flat spectrum $n = 0$, while other models, including string models, foresee $n > 1$, and therefore spectra increasing with the frequency.

It is well known that detecting a stochastic background requires cross-correlating the output of at least two detectors. An upper limit may result in the form

$$h_{100}^2 \Omega_{f_0} < \beta \frac{10\pi^2}{3H_0^2} \frac{1}{\sqrt{T \int I(f) df}} \tag{11}$$

where h_{100} is just the Hubble constant in units of 100 km/s/Mpc. The factor β is a statistical factor related with the false alarm and false dismissal probabilities. The integrand $I(f)$ is in turn

$$I(f) \equiv \frac{\gamma^2(f)}{f^6 S_1(f) S_2(f)} \left(\frac{f}{f_0} \right)^{2n} \tag{12}$$

where $\gamma(f)$ expresses the coherence between GW background detected at different sites, where detectors having noise spectral density $S_i(f)$ are operated.

We show in Fig. 9 the function $I(f)$, normalized to unit integral, for different values of the exponent n. Since the upper limit in Eq. 11 depends upon the inverse of the integral of $I(f)$, the frequency regions where $I(f)$ is larger are also those most contributing to the integral, thus signaling portions of the frequency spectrum where more significant upper limits can be set.

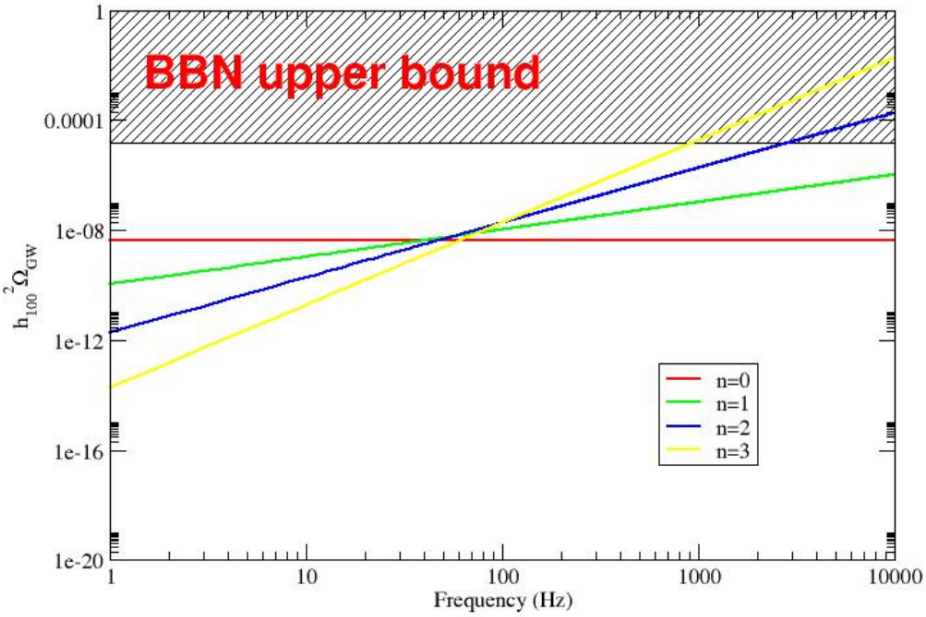

Figure 10: The plot shows, for different values of the power law index, the frequency dependency of the smallest spectral density limit that could be detected by integrating for one year data by AdV and one of the Advanced LIGO detectors.

For larger values of n, the integrand $I(f)$ is dominated by higher frequencies.

Limits on the spectra of background We show in Fig. 10 a comparison of the different models of stochastic background spectral dependence, as a function of frequency. The Ω_{f_0} scale is set as the upper limit which could be set by operating AdV and one of the Advanced LIGO detectors (the one at Hanford to be precise) for one year. The different curves show that for larger n the high frequencies become more important and so the role of AdV in an LSC-Virgo network.

However, note that the stochastic background is robustly bound by the big-bang nucleosynthesis limit: gravitational waves energy exceeding the bound would have led the Universe to evolve too quickly through the primordial nucleosynthesis phase and alter the observed balance of barionic matter.

Moreover, the LIGO S5 run should end up setting a limit shortly below the BBN bound.

4.3 AdV operation in a network of GW detectors

The AdV detector will harvest the best of its detection and GW science potential in cooperation with other GW detectors, and most notably with the Advanced LIGO detectors, which will be operating in a coordinated fashion with AdV, having a comparable sensitivity for most of the sources.

We have already discussed briefly how AdV would be exploited, in cooperation with Advanced LIGO detectors, to place upper limits or detect a stochastic background of gravitational radiation.

Another important role will be played in the detection and parameter estimation of signals emitted by point sources.

4.3.1 Coherent analysis

The reason why a network of GW detectors is on one hand a necessity, on the other hand a unique opportunity, lies in the simple nature of gravitational waves. As it is well known, in the theory of General Relativity the gravitational waves can be expressed as perturbations of the metric which are transverse and described by two polarization states $h_+, h_\times$, as appropriate for massless fields.

Now point sources of GW, like coalescing binaries or supernova explosion, have the property that this signal is fully coherent at any terrestrial site; each detector will be sensitive to a certain linear combination

$$h(t) = F_+(\theta, \phi)h_+(t) + F_\times(\theta, \phi)h_\times(t) \tag{13}$$

of the $h_+(t), h_\times(t)$ GW polarizations coming from the direction θ, ϕ, weighted by the antenna patterns $F_+, F_\times$.

While the antenna patterns depend upon location and orientation of each detector, the same h_+ (or $h_\times$) is received at any detector site, apart delays introduced by the finite speed of wave propagation, and small [8] Doppler effects due to Earth rotation.

It is possible to exploit this Earth-scale coherency to use a minimum of three detectors to reconstruct the two polarization components, as well as the source direction θ, ϕ, even without any knowledge of the waveform, as first shown in [27].

More in detail data generated by a network of n detectors reside in a n-dimensional space. Since GW have two polarizations and the detectors see a linear combination of them, the signal lies in a two-dimensional subspace. Therefore, the signature left by a GW in the data is zero when projected onto the complementary so-called "null" subspace (i.e., the $n-2$ remaining dimensions). This implies that when we have $n \geq 3$ (misaligned) GW detectors, the "null" subspace has at least one dimension: there exist at least one linear combination of the data such that the GW signal is canceled out. Those combinations are referred to as "null streams"; the larger the network, the greater the number of null streams.

Null streams are useful to veto false triggers due to instrumental artifacts, which do not obey this cancellation property. In a coherent search, it is required that the GW candidate has a large "coherent amplitude" (amplitude of the projection onto GW plane) as compared to its "null amplitude" (amplitude of the projection onto the null space).

[8] But significant for pulsar signals

In gaussian noise, a coherent operation of AdV and of the Advanced LIGO detectors achieves the maximum possible detection probability, at a fixed false alarm rate [28].

Adding AdV coherently to a network of Advanced LIGO detectors leads therefore to an increased detection rate. A quantitative estimate of the benefit is possible under the assumption of gaussian noise [29], and has been recently carried out [30], showing that the detection rate for BNS could be increased by about 35%. Similar or greater benefits are possible for burst events [28].

It should be remarked, though, that the increased detection rate is of secondary importance with respect to the benefits resulting by having included a third site in a network of advanced GW detectors; this will make possible the solution of the inverse problem.

In particular, it will be possible by way of coherent analysis to reconstruct in an optimal way the source parameters, for instance for BNS signals [31].

4.3.2 Coincident analysis

The presence of non-gaussian noises may limit to some extent the applicability of coherent analysis techniques, even though the null streams requirements can help rejecting in large part the resulting extra false candidates.

However, much of the benefit of the detectors network can be harvested just on the basis of standard coincidence analysis, augmented by coherent follow-ups.

For instance, it can be shown that coincidence analysis using a LIGO-Virgo network can lead to pinpoint the source location of burst events, with an accuracy depending on the inverse SNR and generally smaller than 1^o already for moderate SNR values [32].

Analogously, it can be shown that a detection strategy of BNS based on a two-fold coincidence, followed by a coherent follow-up, is competitive with the coherent analysis starting at $SNR_{network} \geq 7$ [29].

In fact, detailed studies for burst [33] and BNS events [34] have demonstrated that a two-fold coincidence strategy in a three site detector network is an efficient strategy, which allows to increase the chances of detection by about 25% over a LIGO network, and to reconstruct the source location as well.

If one considers a three-fold coincidence strategy, the Advanced LIGO + Advanced Virgo network, which comprises four detectors at three sites, has a detection probability increased by 40

The other advantage of coincidence analysis is the robust rejection of spuria, as well as the possibility to estimate the background noise by introducing relative time shifts among the data by the various detectors.

It is also possible to show that the bulk of information leading to the reconstruction of source direction is contained in the time delays across the detector network [35].

It is important to underline that a successful operation of AdV in a network of GW detectors requires that its sensitivity is comparable to its partners [28].

4.4 Multimessenger opportunities

In this section we would like to underline that a host of collaborative work with other observatories will be needed, in the Advanced Detector era, to fully exploit the detector potentialities.

4.4.1 Radio observatories

We would want just to mention that radiotelescopes are instrumental for carrying out succesfully a detection program for continuous signals emitted by pulsars.

As discussed already, the targeted search of GW emitted by known pulsars relies on the assumption that the phase evolution is coherent over long time scales. If a "star quake" occurs, it can introduce a "glitch" both in the series of EM pulses and in the GW signal. Knowing whether a glitch has occurred is possible, if the radiotelescopes regularly check the count of pulses for slight variations in the expected arrival of the event.

The Advanced detectors will need this information at least for the most interesting pulsars, ensuring that sufficient coverage of the targets is in place throughout the observation phase.

Needless to say, a confirmed correlation between GW and EM glitches would tell us a lot about the structure of the NS crust and its dynamics.

4.4.2 Optical observatories

Ground based optical detectors remain the most important source of information in the e.m. spectrum for a variety of sources, including the light curve of supernova events.

Robotic detectors are sufficiently inexpensive to be dedicated to systematically follow-up a reasonable number of triple coincident triggers issued by LIGO and Virgo detectors, for which a source position could be reconstructed with sufficient accuracy.

We expect such a program to be potentially rewarding, while being affordable in terms of human and monetary resources.

4.4.3 X-ray observatories

A range of X-ray satellites, including Chandra [36] by NASA and X-MM Newton [37] by ESA, are operating in Earth orbit and provide data of interest also for the GW community.

Indeed, although γ-ray events have captured most of the interest, it is well known that also X-ray prompt bursts or longer tails have been observed in conjunction with core-collapse supernovae and GRB events.

While both Chandra and X-MM Newton missions can be expected to last until the beginning of the Advanced GW Detectors era, we can hope that the joint ESA-NASA X-Ray Evolving Universe Spectrometer (XEUS) [38] will be operating as a successor.

4.4.4 Gamma-ray observatories

Probably Gamma Ray Bursts constitute the most exciting recent discovery in astrophysics, and the most likely source of events correlated with GW signals.

The NASA's SWIFT [39] satellite, which is a veritable multi-messenger observatory, carrying also optical and X-ray telescopes, will carry on its mission during the Enhanced GW detectors era, but is not expected to be alive in the AdV era. It will be replaced by the recently launched international Fermi Gamma-ray Space Telescope (formely known as GLAST) [40], which retains the capability of "swift" pointing towards GRB sources, while providing greater sky coverage and sensitivity over a much wider range of energies, up to ~ 300 GeV.

We have already underlined the importance of γ-ray events as potentially correlated with coalescing binaries and core-collapse supernovae. It is expected that advanced detectors will both search for events at times triggered by GRB observatories, but also issue alerts for triple or quadruple coincident events that could be worth investigating by pointing satellite based instruments.

4.4.5 Low energy neutrino observatories

The so-called "thermal" neutrinos, having energies of a few tens of MeV, are produced in short bursts (a few seconds) in the core-collapse supernovae, through the inverse β-decay process of neutronization. They are copious and carry out some 99% of the gravitational energy released, so that the existing detectors, like Super-Kamiokande [41], LVD [42] and IceCube [43] can detect them within the Milky Way and beyond the magellanic clouds [9].

These detectors operate under the agreement [44], exchanging time information about events, and regularly searching for coincidences which could correspond to a real SNe [10]. Both Super-Kamiokande and IceCube are expected to be in operation in the AdV era.

A correlated detection of an event by neutrino detectors and by GW detectors would first of all strengthen the case of a real detection, which means that at fixed FA rate the detector thresholds could be lowered and events originating further out in space could

[9] Even though IceCube is designed for high energy ν, it can detect SN neutrinos in the Large Magellanic Cloud with a 5σ significance

[10] The Sudbury Neutrino Observatory (SNO) [45] was also part of the agreement snews, and has been recently decommissioned. Plans are underway, though, to upgrade it to SNO+ [46]

pass the first trigger level and be detected. Further, such a coincident detection would provide information about the collapse mechanism, and the relative GW - neutrino timing would allow probing the neutrino masses.

4.4.6 High energy neutrino observatories

In the Advanced detectors era we expect to have at least two large scale neutrino observatories in operation; IceCube [43] at the south pole, which is under realization as a successor to AMANDA [47], and the large scale KM3Net detector [48] in the Mediterranean sea, successor to the existing detector Antares [49] and to the R&D projects NEMO [50] and NESTOR [51].

These neutrino detectors use an array of photomultipliers, regularly spaced in a large volume of water, to collect and detect the Cerenkov light emitted by charged particles which result from the collision of the high-energy ν's with the nuclei in water. The simultaneous excitation of several photomultipliers allows to reconstruct the direction of the charged particles and to infer the one of the incoming ν. The angular resolution is expected to be of the order of 1^o, therefore comparable with the one expected for the LSC-Virgo network of advanced detectors.

There is a range of potential sources of joint ν - GW emission; among the most promising we just list

Short GRBs High Energy ν's might be emitted during the binary mergers [25].

Long GRBs HE νs are expected to be produced in the shocks by accelerated protons, with fluxes sufficient to be detected at cosmological distances by km^2 scale ν detectors like IceCube and KM3NeT.

Soft Gamma Repeaters giant flares the violent crustal reorganization occurring in magnetars is believed to emit both GW and ν's, with fluxes that might be detectable or at least allow to constrain the models.

As with other joint observation, the simultaneous detection of GWs and HE ν's would give enormous insight into the generation processes, and also increase the reach of both instrument classes to fainter, further out events.

Advanced Virgo Baseline Design:
PART 2:

Interferometer

5 Advanced Virgo: interferometer configuration

5.1 Introduction

This section describes the optical parameters and configuration of the AdV interferometer. The optical layout and the main parameters of the design are briefly summarised first, followed by a more detailed description of selected topics.

The design of the AdV core interferometer falls within the scope of the *Optical Simulation and Design* (OSD) subsystem. The optical layout and the nomenclature of the core interferometer, including the Michelson interferometer, its arm cavities and the mirrors forming the Power- and Signal-Recycling cavities is shown in Figure 11. Compared to the optical layout of Virgo, the AdV design features three main changes: the inclusion of Signal Recycling, the change in the arm cavities' geometry from a flat-concave to near-symmetric design and the move from marginally stable recycling cavities to non-degenerate recycling cavities. These topics will be described in more details in the following sections.

5.1.1 Optical layout

The optical layout of the main AdV interferometer is shown in Figure 11, with the main or core interferometer being defined as the long-baseline Michelson interferometer formed by the central beam splitter (BS) with arm cavities (X-arm and Y-arm) and the so-called recycling mirrors (PRM, SRM) in the input and output ports of the Michelson interferometer.

The laser light, after being filtered by the input mode-cleaner (IMC, not shown in this figure), is injected into the interferometer through the semi-transparent Power-Recycling mirror. Arm cavities as well as the Power-recycling mirror are used to enhance the light power circulating in the arm because the signal-to-shotnoise ratio of the optical readout scales with the square root of the circulating power. The main output port of the interferometer is the so-called *asymmetric port* (AP), with the Michelson set such that this port is on the dark fringe. Before being detected on a high-power photo diode the signal is optically enhanced and filtered in the Signal Recycling cavity (formed by SRM1 and the Michelson) and then spatially filtered by a small rigid mode-cleaner cavity (OMC). The other optical outputs depicted by photo-diodes in figure 11 are detection ports that can potentially be used for interferometer control or monitoring purposes.

5.1.2 Design summary

The current configuration of the main interferometer is defined by the parameters given in table 7. This section provides a brief explanation of the optical parameters, in the same order as the following sections with a more detailed description.

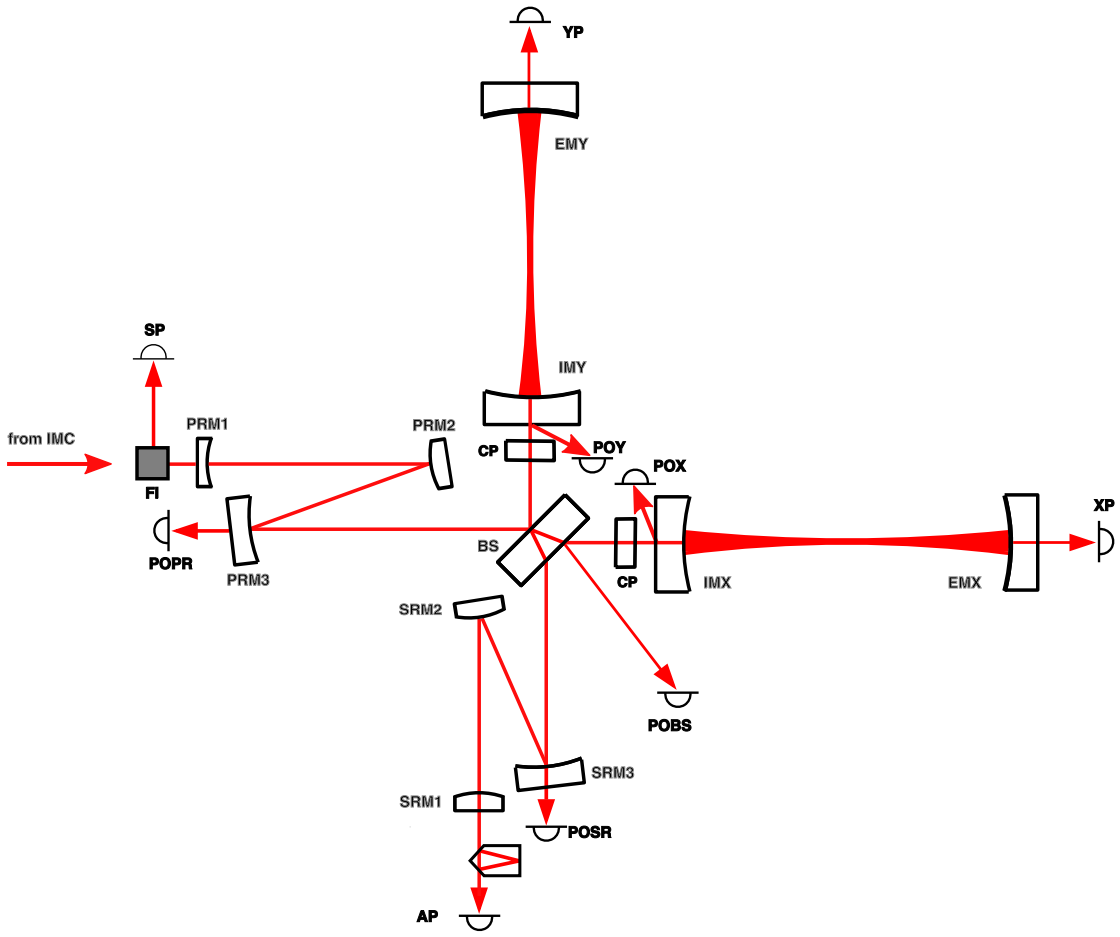

Figure 11: Optical layout of the AdV core interferometer: A new, clear nomenclature has been chosen [52] for Advanced VIRGO in order to avoid inconsistencies and possible confusion with the ongoing work on the Virgo interferometer: The interferometer arms will be identified by the letters *X* and *Y*, with the North arm, in-line with the input beam, being the X-arm. Cavity mirrors are called input mirror (IM) or end mirror (EM). Thus the North arm cavity (X arm) is formed by IMX and EMX. Compensation plates (CP) are located between the beam splitter (BS) and the cavity input mirrors. The recycling mirrors are called power recycling mirror (PRM) and signal recycling mirror (SRM). The dark fringe output port the Michelson interferometer is the *asymmetric port* (AP). The *symmetric port* (SP) denotes the back reflection from the Michelson (in-line with the X-Arm). Other readout ports are named after the optical component providing the beam: the light transmitted by the X-Arm cavity is called XP. So-called 'pick-off' beams will be labelled with *PO*, i.e. the reflection from the anti-reflective coating of the beam splitter will be detected in POBS. The folded optical path inside the Power- and Signal Recycling cavities increase the cavity lengths, which is required to achieve non-degeneracy for these cavities. The curvatures of the Recycling mirrors and of the folding mirrors are determined by cavity length and the required Gouy phase, see section 5.5.

Light power The light power circulating in the arms is maximised by increasing either the finesse of the arm cavity and/or the finesse of the Power Recycling cavity (see below) to reduce shotnoise.

Arm cavity geometry Both arm cavities have the same geometry, with the beam waist being close to the center of the cavity. This minimizes the thermal noise contribution. Care has been taken to reach a stable cavity suppressing higher-order modes.

Arm cavity finesse Both cavities have the same finesse. High-finesse cavities help to suppress the coupling of noise originating from within the central interferometer as well as to reduce the thermal load on substrates of the input mirrors, beam splitter and compensation plates.

Geometry of mirror and beam splitter substrates The size of the mirrors should be as large as possible to minimise thermal noise and is limited by technical constraints. The thickness does not influence the optical design. So far the design has been kept open on whether to include wedges in the substrates. In some configurations wedges can create extra pick-off beams or can help to separate such beams from the main beam.

Power Recycling cavity The Power Recycling mirror is used to further enhance the circulating light power and thus to reduce shotnoise. The finesse of the cavity is designed following the arm cavity finesse. The current design features a non-degenerate cavity with two turning mirrors and a folded path. This design should make the interferometer more robust against thermal deformations and misalignments.

Signal Recycling cavity The Signal Recycling mirrors allow to tune and shape the quantum noise limited sensitivity of the detector; the SRC finesse affects the detector bandwidth and the SRM tuning the frequency of the peak sensitivity. The only drawback of Signal Recycling is a more complex control system. Also the Signal Recycling cavity is designed to be non-degenerate.

AdV Optical Configuration			
Light Power			
arm cavity power	760 kW	power on BS	2.7 kW
Arm cavity geometry			
cavity length L	3000 m		
IM R_C	1416 m	EM R_C	1646 m
Beam size on IM w	56 mm	Beam size on EM w	65 mm
waist size w_0	8.5 mm	waist position z	1385 m
Arm cavity finesse			
finesse	900	round-trip losses	75 ppm
transmission IM T	0.7%	transmission EM T	5 ppm
Power recycling			
transmission PRM T	4.6%	finesse	70
PRC length	28 m	Beam size on PRM1	1.8 mm
Signal recycling			
transmission SRM T	11%	finesse	40
SRC length	28	SRM tuning	0.15 rad
Mirrors			
IM diameter	35 cm	EM diameter	35 cm
IM thickness	20 cm	EM thickness	20 cm

Table 7: Parameters of the AdV interferometer.Throughout the text we quote numerical values for several optical parameters. In many cases the exact value for such parameters will be adjusted during later stages of the design or during implementation. Therefore the values given in this table have been rounded to a few significant digits.

5.2 Beam size and waist position in the arm cavities

The beam sizes at the IM and EM as well as the position of the cavity waist are determined by only two parameters, the radii of curvature (ROC) of IM and EM. In order to find the optimal ROC values a trade off analysis was performed taking into account the following aspects:

- Coating Brownian noise
- Clipping losses of the mirrors
- Mode-Non-Degeneracy

The power spectral density, $S_x(f)$, of the coating Brownian noise can be expressed as [53]:

$$S_x(f) = \frac{4k_\mathrm{B}T}{\pi^2 f Y}\frac{d}{r_0^2}\left(\frac{Y'}{Y}\phi_\parallel + \frac{Y}{Y'}\phi_\perp\right) \tag{14}$$

where f is the frequency, d the total thickness of the coating, r_0 describes the beam radius, Y and Y' are the Young's Modulus values for the substrate and coating respectively. $\phi_\parallel$ and $\phi_\perp$ are the mechanical loss values for the coating for strains parallel and perpendicular to the coating surface.

As indicated by Equation 14 the amplitude spectral density of the coating Brownian noise decreases proportional to the beam radius, r_0, at the mirror. Since the contribution from the coating Brownian noise (together with the quantum noise) directly limits the AdV sensitivity in the mid-frequency range (see Figure 2), the overall detector sensitivity increases with larger beam size at the IM and EM. That is the reason for moving the cavity waist from the IM (where it is placed in initial Virgo) towards the center of the arm cavity, resulting in roughly equal beam sizes at the IM and EM.

In addition one can see from Equation 14 that the amplitude spectral density of the coating Brownian noise of a mirror is proportional to the square root of the coating thickness. Due to the fact that for the very high reflectance of the EM a thicker coating is required than for the IM, the coating noise contribution of the EM would be higher than the one of the IM (assuming identical beam sizes). However, the lowest overall coating thermal noise of all four IM and EM is obtained for equal coating noise contribution of all four mirrors. This can be achieved by positioning the cavity waist not directly in the center of the arm cavities, but slightly shifted towards the IM.

However, technical constraints, such as the actual size of the dielectric coatings or the free apertures of the reference masses limit the maximum beam size for a certain amount of tolerable clipping losses. There are two problems connected to clipping losses: If the laser beam is too large for the mirror or its coating some light will be clipped, thus reducing the achievable power enhancement inside the interferometer. In addition if the clipped light is not properly destroyed or dumped, it might cause scattered light noise. A detailed analysis of the maximal coating size to beam size ratio can be found in [54]. For the

	input mirror	end mirror
beam radius [mm]	56	65
ROC [m]	1416	1646

Table 8: Design parameter of the AdV arm cavity geometry.

baseline mirror diameter of 35 cm clipping losses are going to limit the maximum beam radius at the test masses to about 5.0 to 6.5 cm.

In order to prevent light to be scattered into higher order optical modes (HOM) it is important to choose the mirror ROCs in a way to ensure that no lower order HOM is resonant inside the arm cavities. Furthermore, considering inevitable manufacturing inaccuracies of the ROC, we have to find ROC values sufficiently separated from the resonances.

In the following we will define a figure of merit for the cavity non-degeneracy. The Gouy phase of the HOM of the order k is defined as [55]:

$$\phi_k = k\frac{1}{\pi}\arccos\sqrt{(1-\frac{L}{R_{c,i}})(1-\frac{L}{R_{c,e}})}. \tag{15}$$

with L being the length of the arm cavity and $R_{c,i}$ and $R_{c,e}$ being the radii of curvature of the input and the end mirrors, respectively. The mode-non-degeneracy for a single HOM of the order k, Ψ_k, can then be expressed as follows:

$$\Psi_k(L, R_{c,i}, R_{c,e}) = |\phi_k - \mathrm{round}(\phi_k)|. \tag{16}$$

In case Ψ_k equals zero any optical mode of the order k is degenerate with respect to the fundamental (TEM_{00}) mode. Finally in order tor provide a comprehensive figure of merit for the non-degeneracy of a cavity we have to combine the Ψ_k for all different HOM of interest. Taking into account all HOM up to the order N, we can now calculate the inverse quadratic sum of the individual $1/\Psi_k^2$ weighted by a factor $1/k!$:

$$\Theta_N(L, R_{c,i}, R_{c,e}) = \frac{1}{\sqrt{\sum_{k=1}^{N}\frac{1}{\Psi_k^2}\frac{1}{k!}}} \tag{17}$$

Θ_N can then be used as figure of merit for the non-degeneracy of the Advanced Virgo arm cavity design.

Using $\Theta_{15} > 0.085$ and a maximum beam size of 6.5 cm as boundaries we derived the optimal beam sizes and ROC values listed in Table 8. For these set of parameters the lowest order HOM close to resonance inside the arm cavity is of order 11 [56].

5.3 Arm cavity finesse

The power enhancement inside the arm cavities is determined by their finesse, i.e. the refelctivities of the cavity mirrors and the round-trip losses inside the arm cavity. In

contrast to initial Virgo where the interferometer response (bandwidth and peak sensitivity) is determined by the actual arm cavity finesse, the AdV sensitivity is determined by a combination of the signal recycling parameters and the arm cavity finesse [58]. This means that the AdV sensitivity can be optimised independently of the arm cavity finesse by choosing the signal recycling parameters properly. This also means that the direct sensitivity optimisation does not serve as a strong criteria for defining the arm cavity finesse.

The main advantage of using high-finesse arm cavities for AdV is a reduced coupling of several noise sources, originating from within the central interferometer (such as for instance lateral movement of optical sustrates featuring wedges [57]), to the GW channel. In addition a high arm cavity finesse decreases the thermal load on the substrates of the input mirrors, the beam splitter and the compensation plates. On the other hand, due the their reduced linewidth, lock acquisition of high finesse arm cavities using the main laser will be more demanding. However, since the lock aquistion procedure of the arm cavities will be based on auxiliary lasers (see Section 11.3.1), the choice of the arm cavity finesse will not influence the performance of the lock acquisition system.

A detailed analysis of the main factors relevant for the final trade-off decision of the AdV arm cavity finesse can be found in [58]. Featuring input mirrors with a power transmittance of 0.7 %, the AdV arm cavity finesse was chosen to be 888.

5.4 Signal Recycling

The term Signal Recycling [59] (SR) refers generally to a Michelson interferometer with a semi-transparent mirror in the asymmetric port. It has been developed and demonstrated over more then ten years from table-top experiments, via implementations on prototypes [60] to being used routinely in the GEO 600 detector today [61]. The main aim of Signal-Recycling is to increase the signal-to-quantum-noise ratio of the detector. Depending on the arm cavity finesse, Signal Recycling comes in two different flavours. If the arm cavities have a low finesse, Signal Recycling can be used to further *decrease* the detector bandwidth to increase the peak sensitivity. This represents to ordinal Signal Recycling configuration. Instead the arm cavities can be designed to have a very high finesse and then the Signal Recycling cavity can be tuned differently in order to *increase* the detector bandwidth again. The latter configuration is often called *resonant sideband extraction* (RSE) and represent the setup chosen for AdV.

Figure 12 shows the effect of the Signal Recycling parameters on the quantum-noise limited sensitivity of AdV for various parameter options. The top plot illustrates how a low transmittance of the Signal Recyling mirror (SRM1) can be used to increase the peak sensitivity by reducing the bandwidth. The lower plot shows, how the quantum-noise limited sensitivity changes shape when the SR tuning is changed. The tuning can be easily changed during operation.

The Virgo vacuum system already includes a vacuum tank for the Signal Recycling mirror. The main challenge of Signal Recycling is the more complex control system. Not only

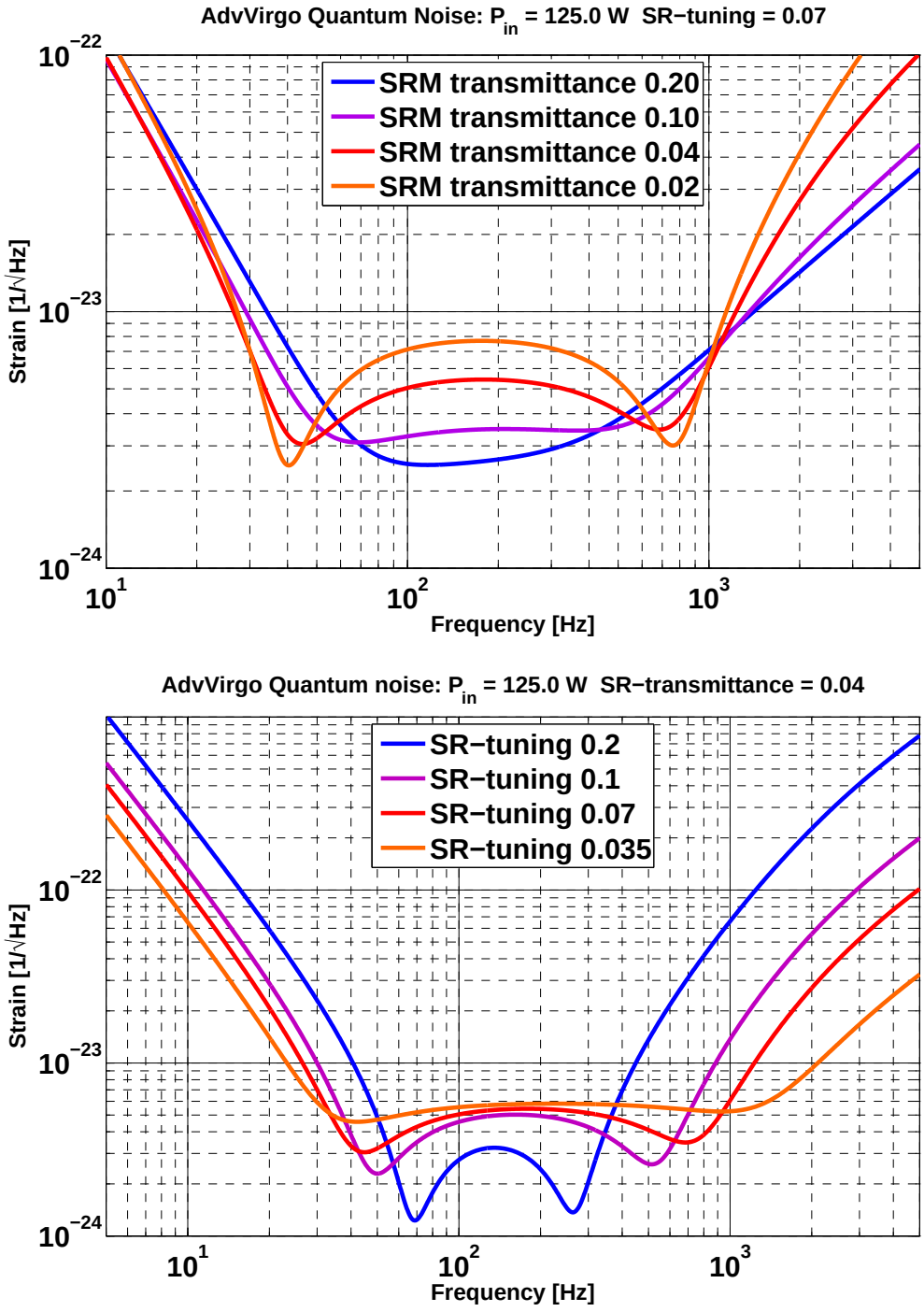

Figure 12: The two plots illustrate the impact of the two Signal-Recycling parameters, *transmittance* and *tuning* of the Signal-Recycling mirror, on the AdV quantum noise. This shows that the exact change of the quantum noise is complex, mostly due to the optical-spring effect. However, the first order effects are that the transmittance changes the finesse of the SRC and thus the bandwidth of the detector, whereas the tuning changes the center frequency of the SRC and thus the frequency of the peak sensitivity of the detector.

does it add three new degrees of freedom (1 longitudinal and 2 alignment) but it forms a very complex split, coupled four-mirror cavity with the Power-Recycling mirror and the arm cavity input mirrors and in consequence the control signals for these mirrors can become more strongly coupled.

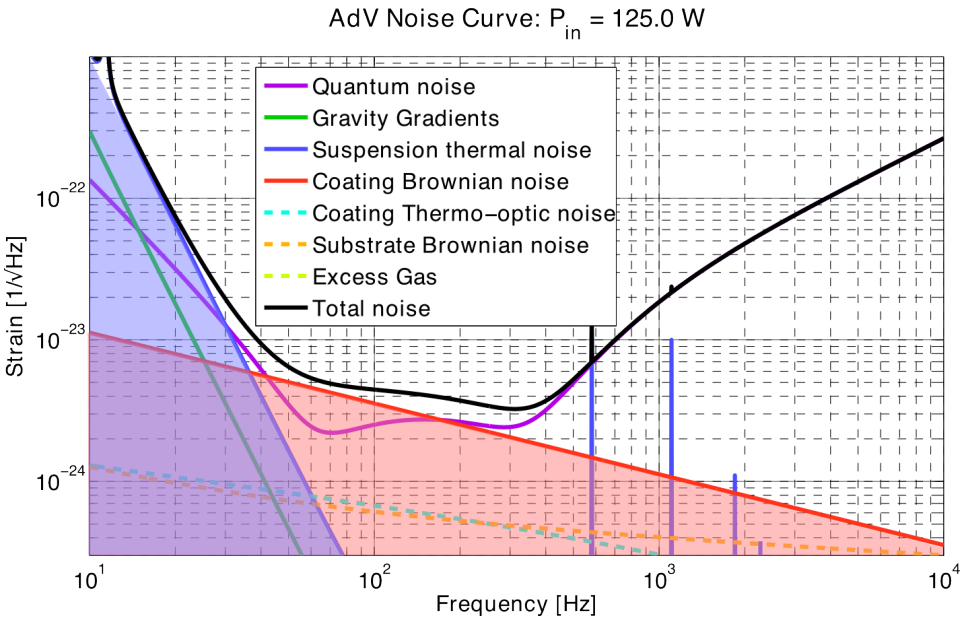

Figure 13: Fundamental noise contributions to the AdV sensitivity. The pink trace indicates the quantum noise for one specific set of Signal Recycling parameters. It is possible to optimise the Advanced Virgo sensitivity for different figures of merit (such as BNS range), by changing the Signal Recycling detuning and the Signal Recycling mirror transmittance. The coloured areas indicate regions which are not accessible via any Signal Recycling optimisation because they are buried by other fundamental noise sources.

5.4.1 Optimisation of the Signal Recycling parameter

As shown in Figure 12, the shape as well as the level of the quantum noise varies strongly with the actual Signal Recycling parameter. Therefore, the variation of the two Signal Recycling parameter (together with the circulating optical power) offers the possibility to optimise the AdV sensitivity for different figures of merit, such as the binary neutron star (BNS) inspiral range.

The sensitivity range available by such an optimisation is shown in Figure 13. At low frequencies the boundary is given by the level of gravity gradient noise, while in the mid and high frequency range coating Brownian noise restricts the achievable sensitivity.

Automated optimisation routines have been developed, based on the OSD-tools [55], [62] and a GWINC model of AdV [63],[8]. These software routines can be used for multi-parameter optimisation (Signal Recycling tuning, Signal Recycling mirror transmittance

and circulating optical power) of the AdV sensitivity for any desired figure of merit. The detector configuration optimised for binary neutron star inspiral range [6] was chosen to be the AdV reference configuration (see Figure 2) featuring a Signal Recycling detuning of 0.15 rad and a Signal Recycling mirror transmittance of 11 %.

5.5 Non-degenerate recycling cavities

One of the major evolutionary step during the development of the optical layout of AdV was the inclusion of non-degenerate (or stable) recycling cavities. This is also a major difference with respect to initial Virgo and initial LIGO, which have a marginally stable (or degenerate) power recycling cavity.

A Fabry-Perot cavity is stable when the transversal mode spacing is much larger than the linewidth of the cavity itself. In these kind of cavities the high-order modes cannot simultaneously build-up when the fundamental mode is resonant. On the contrary, in a degenerate cavity, the optical power is easily transferred from the fundamental mode to the higher-order modes in presence of misalignments, thermal deformation of the mirrors or any other defects in the mirror geometry.

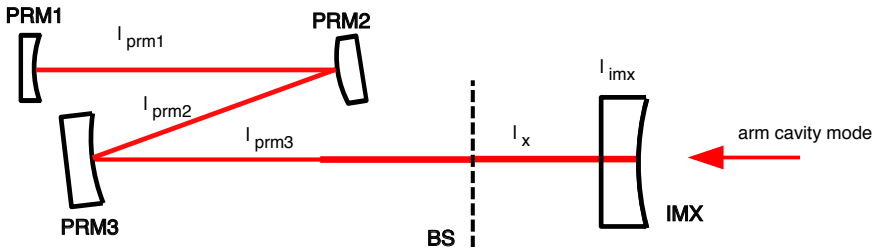

Figure 14: Simplified layout for a non-degenerate power recycling cavity. IMX represents the X-arm cavity input mirror, PRM1 is the power recycling mirror and PRM2 and PRM3 are turning mirrors that act as a kind of mode-matching telescope.

Typically non-degeneracy can be obtained if the length of the cavity is larger than the Rayleigh length of the eigenmode. The Rayleigh length of the beam inside the arm cavities is several hundred metres, while the lengths of the recycling cavities is only of the order of 10 metres. Therefore the optical design for a non-degenerate cavities increases the length of the recycling cavities and employs focusing elements to reduce the Rayleigh length of the beam. The distances between the mirrors in the recycling cavities are largely defined by the location of the vacuum tanks. Therefore the length of the recycling cavities cannot be increased significantly except by folding them. Various options for folded beam paths [64] have been evaluated.

Figure 15 shows a sketch of the mirror positions in the Power Recycling cavity: The Power Recycling mirror PRM1 is located on the suspended injection bench while the telescope (or turning) mirrors PRM2 and PRM3 are located in the BS tank and the PR tank

respectively. The optical layout of the Signal Recycling cavity is equivalent, but refers to the SR tank and to the suspended detection bench instead of PR tank and injection bench. Therefore in the following we only describe the numerical parameters exemplary for the Power Recycling Cavity.

The optical layout of the Power Recycling Cavity has the following approximate distances between optics[11]:

	l_{prm1}	l_{prm2}	l_{prm3}	l_{x}	total
length [m]	10.5	5.5	6	5.5	≈ 28

This optical layout puts the optics into the existing vacuum enclosure but requires a redesign of several suspension systems: the injection and detection bench now must accommodate a suspended recycling mirror and the beam splitter tank now hosts three large suspended optics.

The quantitative parameter to describe the non-degeneracy numerically is the Gouy phase of the cavity eigenmode. Gouy phases at 0 and 180 degree mark a marginally stable cavity while values in between indicate non-degeneracy. At the moment the ideal value for the Gouy phase (and whether it should be identical in both recycling cavities) is not yet determined. However, the optical design presented here can be easily adapted to any required value for Gouy phase between 0 and 180 degrees.

We have further used the following criteria to define the parameters of the optical layout:

- the eigenmodes of the recycling cavities are matched to the arm cavity eigenmode (in the sagittal plane at least), given by the Gaussian beam parameter inside the arm cavity at IMX of $q = 1382.573 + 214.9768\mathrm{i}$.
- the absolute radii of curvatures of PRM2, PRM1 and SRM2 and SMR1 are to be as large as possible
- the beam size on PRM1 and SRM1 is to be as large as possible to reduce the impact of thermal noise [65]

Following these criteria the radii of curvature for all mirrors in the recycling cavities can be computed. The resulting parameters for the Power Recycling Cavity for a Gouy phases of 160 and 20 deg are exemplary shown in Table 9.

[11] Please note that for compatibility with RF modulation frequencies the lengths of the recycling cavities must be adjusted further. However, this has only a small influence on the cavity parameters presented here. The exact cavity length and the exact radii of curvatures will be determined at a later stage.

Gouy Phase 160 deg:

	IMX AR	BS	PRM3	PRM2	PRM1
ROC [m]	flat	flat	12.55	-1.79	1.81
w [mm]	55.5	55.8	56.2	7.24	1.42
w0 [mm]	6.19	6.19	0.0381	0.414	0.414
z [m]	1.01e+03	1.01e+03	-6.31	-8.84	-1.66

Gouy Phase 20 deg:

	IMX AR	BS	PRM3	PRM2	PRM1
ROC [m]	flat	flat	12.80	-2.04	-2.03
w [mm]	55.5	55.8	56.2	8.2	1.25
w0 [mm]	6.19	6.19	0.0388	0.505	0.505
z [m]	1.01e+03	1.01e+03	-6.44	-12.2	1.7

Table 9: Mirror curvatures and beam parameters for Gouy phase of 160 deg and 20 deg. ROC is the radius of curvature of the respective mirror. w refers beam size on the respective component; w_0 and z give the beam parameters for each beam segment in the form of waist size and position. These parameters refer to the beam *leaving* the respective component.

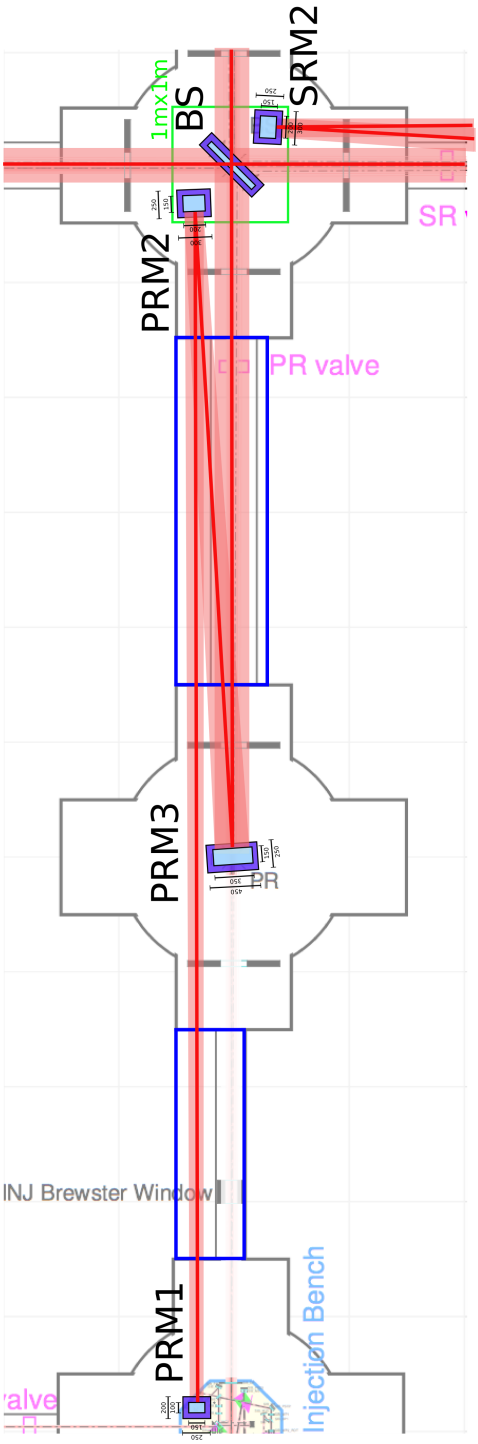

Figure 15: Sketch of the optical layout, highlighting the positions of the mirrors in the Power Recycling Cavity. (Please note that the large beams and the mirrors PRM1, PRM2, PRM3 etc have been drawn over an old CAD file of the optical layout to illustrate their position and geometry. Additional details in the underlying CAD drawing are not necessarily those of the baseline design.)

6 Pre-stabilized laser

6.1 Overview

The Power Stabilized Laser (PSL) system will deliver at least 165W[12] in TEM_{00} mode at the input of the INJ subsystem. It will be pre-stabilized in frequency and amplitude to bring down the noise of the laser to the level required at the entrance of the suspended Input Mode Cleaner (IMC), and should respect a set of requirements concerning beam geometry and beam jitter.

The system consists of the following elements :

- the high power laser including the power supplies for pumping diodes, the cooling system and the injection locking optics and electronics;
- the frequency pre-stabilization loop locking the laser frequency on the suspended IMC, and the fast photodiode utilized in that loop;
- a triangular pre-mode-cleaner (PMC) for spatial and frequency filtering of the beam, housed in a vacuum vessel to avoid acoustic noise and mirrors contamination, and its control optics and electronics;
- the power stabilization of the laser with a control loop utilizing a special photodiode (100mA standing current and good uniformity) mounted after the input mode cleaner and on a seismically isolated table under vacuum;
- the positioning of the electro-optics modulators (EOM) and Faraday isolators (FI) used between the Master laser and the high power amplifiers or injection-locked lasers;

All the parts of the PSL are summarized on Fig. 16 below; the functions of the SS will be detailed in the following paragraphs.

The PSL system does not include:

- the optics and mechanics of the IMC;
- the design of the external detector table will be shared with INJ subsystem, for matching and steering optics used by both.

6.2 Specifications

In order to reach the AdV sensitivity, the laser has to fulfill a number of specifications among which there are the beam requirements, in term of output power, stabilities. Its location at the front end of the interferometer results in very few interferences with other subsystems. Actually, the SS PSL needs some inputs for the requirements and except a

[12] Such a power corresponds to what has been obtained so far for the Advanced LIGO laser.

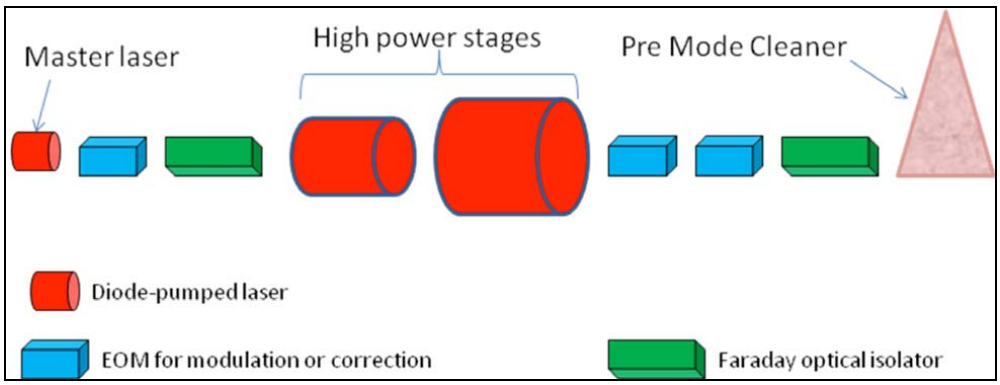

Figure 16: Synoptic of the different hardwares of PSL (no stabilization hardware on this figure)

few interfaces with INJ and is completely independent for the construction and installation of other SS.

Requirement	**Value**
Power	165 W on TEM_{00} at the input of INJ
Frequency noise	$PSD(f) < 10/f$ Hz/$\sqrt{\text{Hz}}$ above 10 Hz
Power noise	$RIN(f) < -170$ dB/$\sqrt{\text{Hz}}$ (for 10 Hz$< f <$10 kHz)
Beam jitter	$< 10^{-8}$ rad/$\sqrt{\text{Hz}}$

Notice that:

- the frequency noise figure referes to the prestabilized laser at the entrance of IMC and will be refined as part of the first deliverable of the Interferometer Sensing Control system (ISC);
- since AdV will use a DC detection scheme, the laser power noise at RF frequency will not be significant. Instead, if RF detection is used, the requirement will be $RIN(f_{\text{mod}}) < -185$ dB/$\sqrt{\text{Hz}}$ (shot noise for 1W detected power);
- the beam jitter is also specified at the entrance of the INJ SS, as likely there will be filtering by IMC and Recycling cavity.

6.2.1 PSL location

As with the initial Virgo, the PSL will be located in the Laser Lab that houses the laser bench and the EIB shared with the Input Optics system. The Laser Lab needs to be

a class 1000 clean room to ensure dust free and clean conditions with a temperature regulated to better than 0.5 °C for stable environment. The external detectors table will be arranged and specified once the layout of the Injection bench (and the Input Mode Cleaner) will be done. The high power laser will be enclosed in a sound proof enclosure as it has been done for the initial Virgo, because the laser frequency and the beam jitter have been found to be very sensitive to local acoustic noise. The electronics racks will be placed inside the Laser Lab following the requirements of noise and bandwidth of the lasers controls. The chillers of the laser system which are noisy will be located in a separate room behind the Laser Lab.

6.2.2 Interface with the other subsystems

The PSL subsystem will interface with other systems for:

- ISC to define the frequency range and the dynamics of the pre-stabilization;
- the high power (HP) standing EOM and FI tested by the INJ subsystem and the position of power stab photodiode on injection bench;
- the monitoring issues, by DAQ subsystem;
- the sound proof enclosure and the maintenance of laser Lab cleanliness, by IME subsystem;
- the HP standing mirrors realization, by MIR subsystem;
- the vacuum tests of PMC, by VAC subsystem.

6.3 The baseline Diode-Pumped Solid-State laser

In the following, we will describe the AdV PSL baseline with the DPSSL technology, as it the technology tested completely so far in the LIGO Science Collaboration The DPSSL consists of a Master laser, two stages of amplification, a medium power stage injection-locked to the master, and a high power stage amplifying the output of the intermediate stage. This technology is based on the Advanced LIGO laser and delivers 180W before any mode cleaning.

6.3.1 The Master laser

The master laser is a monolithic stable structure and the power needed for AdV is 2W. It is a commercial NPRO laser produced by Innolight-Hannover. While the 1W product has a reliability and a reproducibility largely demonstrated in the initial Virgo or LIGO, the long term operation of the 2W product is under test in the LSC collaboration.

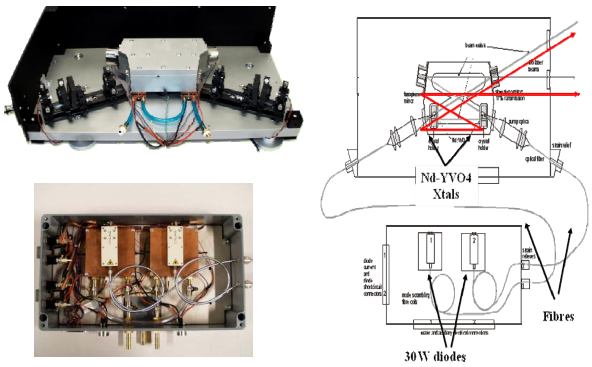

Figure 17: Medium power stage of 20W in bow-tie configuration.

6.3.2 The Medium power stage

The medium stage for the AdV Laser (fig. 17) is based on the 35W laser used for the e-LIGO (LZH design). It is a ring resonator in bow-tie configuration and involves two conductively cooled Nd:YVO4 crystals, each being longitudinally pumped by a fiber coupled laser diode at a rate of $< 60\%$ output power . Temperature stabilization of the laser crystals and the pump diodes is performed by computer-based PID controllers. The employment of a low thermal expansion steel for the resonator block in combination with the negation of adjustable resonator components results in a high intrinsic stability and a reduced acoustic sensitivity of the slave oscillator. The resonator is equipped with three transducers to control its length (one piezo-electric transducer (PZT) with large dynamic, one fast PZT with small dynamical range and one thermally controlled mounting). It is injection-locked to the output radiation of the 2W power of the Master laser and a Pound-Drever-Hall control loop acts on these three transducers to increase the gain of the injection locking process in the servo-loop bandwidth.

6.3.3 The injection-locked process

In the injection locking process, the stability of the master laser is transferred to the slave laser in the following range named locking range:

$$\Delta\nu_{\text{inj}} = \frac{\gamma_{\text{osc}}}{\pi}\sqrt{\frac{P_m}{P_s}} \tag{18}$$

where γ_{osc} is the cavity decay rate, P_m is the injected master power and P_s is the slave power. We can see that the stability requirements of the slave are given by the locking range of the slave which is function of the ratio of slave internal power and the power injected by the master. To increase the locking range, the ratio of the HP to the master powers should be kept low, requiring then a double-stage injected lasers while Pound-Drever-Hall locking scheme help stabilizing the oscillator resonator for each stage by

increasing the gain of the injection process. The frequency noise of the slave laser is then governed by the master laser well below the locking range and dominated by the slave noise at frequencies higher than the locking range.

6.3.4 High power SSL stage

The 180W (power level with a few low order modes) high power stage is a ring resonator with four pumped Nd:YVO4 heads combined in a birefringence compensation scheme. This configuration (see fig. 18) is different from the 60W amplifier provided by LZH for Virgo+ but the thermal management of the crystals is the same. Thermally induced mechanical stress results in stress induced birefringence and causes depolarization, bifocusing: this stress can be compensated by involving two identically pumped rods and a 90° quartz rotator. A relay optic consisting of two identical lenses images the principal planes of the rods onto each other while keeping the laser field unmodified. Therefore a nearly perfect birefringence compensation can be achieved. In the laser tested so far by LIGO, two birefringence compensated pairs are formed to a ring square resonator design.

A three lens optic images the end surface of the homogenizer into the laser crystal (see fig. 18). The laser crystal consists of a 3 mm diameter multi-segmented Nd:YAG rod with two 7 mm long undoped segments at both ends and a 40 mm long low-doped center segment. The undoped end caps reduce the thermally induced mechanical stress on the end surfaces of the rod and eliminate any mechanical deformation of the ends. Further on, the complete doped region of the rod can be effectively cooled, which is essential for the end-pumped geometry in connection with direct water cooling. During propagation, the pump light is mixed and guided by total internal reflection at the rod surface. The crystal involves a double pass for the pump light in order to reduce the longitudinal thermal gradient and reduce the overall mechanical length.

6.4 SSL control strategy

Fig. 19 shows the control scheme for the AdV PSL [66] based on the Virgo experience. The definition of the final specifications will need more calculations and modeling studies to refine the numbers in table 1, taking into account the design changes. For instance, the numbers given above assume the same filtering of the IMC as for Virgo and the same prestabilization scheme (i.e. a laser prestabilized on the IMC and a power stabilization performed after the IMC). They also assume that the contrast and asymmetries of the interferometer, and the precision of alignment and longitudinal controls, will remain the same as they are in Virgo, and that the OMC (output mode cleaner) is unchanged. The possible change to the DC detection might relax some constraints in RF range compared to Virgo while needing some relevant effort in the low frequency range.

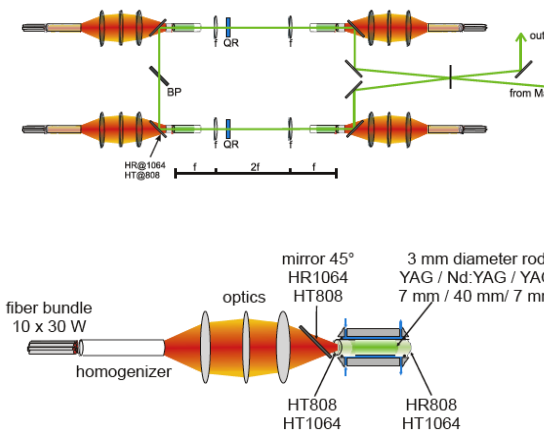

Figure 18: TOP: schematic layout of the Advanced LIGO HP stage. BOTTOM: schematic layout of an end-pumped laser head designed by GEO-LZH

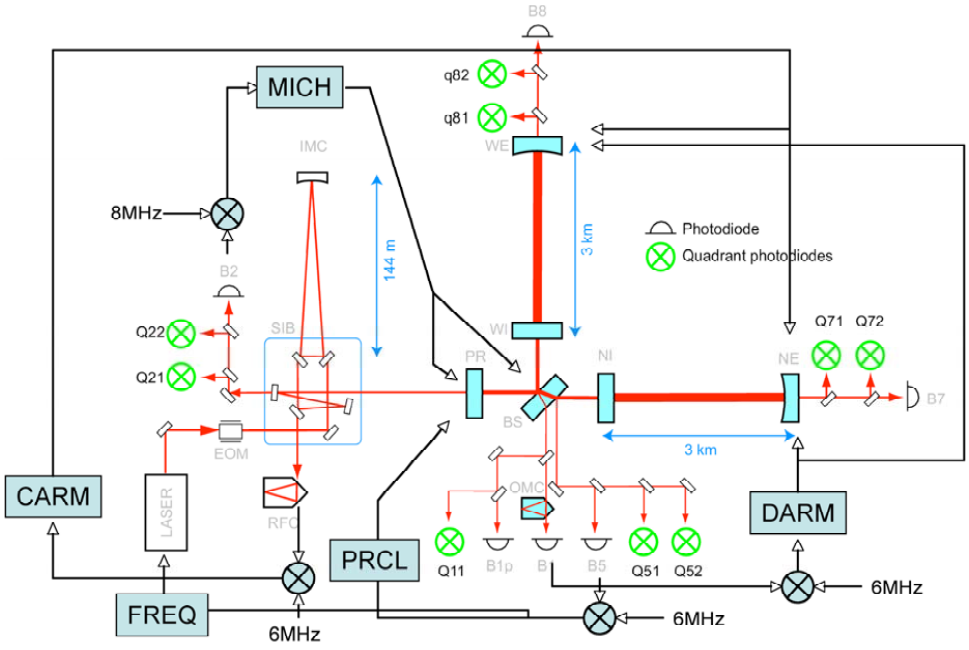

Figure 19: A schematic of the optical layout and control strategy for the AdV PSL.

6.4.1 Frequency pre-stabilization

The only reference for frequency stabilization below a few tens of Hz is the common mode of the two Michelson arms. A short rigid cavity would have an important thermal noise and would not fit the requirements. The frequency stabilization scheme for AdV is likely similar to the one used for the initial Virgo, The global interferometer stabilization scheme utilizes nested loops incorporating error signals from the arms Fabry-Perot cavities, the recycling cavity, the common-mode of the long arms. The equivalent filter of this composite cavity is a first order pole of 10 Hz for the frequency fluctuations of the laser. This loop is not sufficient because its unity gain is limited to 20 kHz (50 kHz is the free spectral range of the cavities) and would not fit a very large loop gain in the detection band up to 10 kHz. A first stage of stabilization is needed, the so called prestabilization stage, which locks the laser frequency to the IMC length, controlled itself by the long baseline cavity. This strategy is detailed by the ISC system and the first delivery of this system will be to specify the requirements for the prestabilization of the laser at the input of the IMC. An EOM at the output of the Master laser serves to impress modulation sidebands on the laser to lock the medium power and HP cavities as well as the PMC length with a Pound-Drever-Hall loop. The prestabilization locks the laser frequency on the IMC length and the feedback loop will act on the master laser s: the fast actuator, a piezo-bonded to the crystal, the slow actuator which is the temperature control of the crystal. Then its stability will be transferred to the HP stages by injection locking and Pound-Drever-Hall loops described above. Another possibility to avoid sidebands HP laser is to use the technique of tilt-locking [67] to control the injected stages and the PMC cavities. This method requires no more R&D and could save extra sidebands on the laser beam.

6.4.2 Power stabilization

The damping of relaxation oscillations is implemented on the Innolight master laser (Noise Eater); it uses a photodiode just at the output of the master laser. Though this loop seems to be enough performant for initial Vigo, in collaboration with Innolight, we have improved this loop by adding more gain between 0-20 kHz range and it can be implemented on the AdV Master laser if needed. To reach the -170 dB required, the laser needs to be stabilized via a photodiode capable of detecting more than 35 mA (shot noise limit for a noise of $3\,10^{-9}/\sqrt{\mathrm{Hz}}$). The sensitivity of beam jitter on the photodiode and the effects of acoustics and of dust particles in the optical path have been highlighted many times in table-top experiments, and consequently this photodiode has to be inserted under vacuum at the point where beam jitter is minimized. The location after the IMC has been proven convenient in initial Virgo and this position is taken as the baseline solution. In addition the plan is to add a second, out-of-loop photodetector to measure the real performance of the servo.

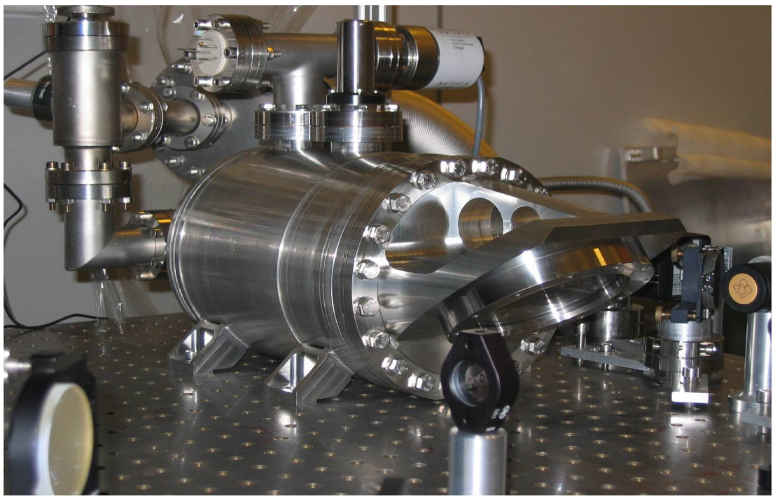

Figure 20: AdV PMC will look like the Virgo+ pre-mode-cleaner, here in the vacuum housing and sitting on the laser table.

6.5 The pre-mode cleaner

The pre-mode cleaner (PMC) is used to filter out the high order modes inherent to the HP stage. Depending on the main modulation frequency (f_{mod}) value, the PMC could be used also to filter the power noise around this f_{mod}. Following the measurements done on a GEO 180W prototype [68], the laser is shot noise limited above 10 MHz, then $f_{\mathrm{mod}} < 9$ MHz will encounter some technical noise of the laser. Consequently the PMC should be designed to act as a low pass filter for f_{mod} in the range of 5 to 10 MHz if necessary. The PMC is a three mirror ring-cavity (two-plane and one curved) inserted into the main beam path and has a high transmission for the fraction of the light in the TEM_{00} mode. A length control system based on a PZT-mounted-curved mirror is needed to keep the cavity resonant with the incoming beam and to compensate for large drifts over long periods of time. A Pound-Drever-Hall loop or a Tilt locking loop will be used to pick up the signal reflected by the PMC. Following the amount of power distributed on high order modes, the finesse of the PMC will be designed by a trade-off between spatial filtering, noise filtering and circulating power. Today the PMC of Virgo+ (fig. 20) stands a power of about 60W without mirror damage thanks to high quality coated mirrors by LMA-Lyon and a vacuum enclosure to keep it air-free and dust-free. The PZT mounting sits behind the curved high reflectivity mirror and will encounter serious heating unless a careful design of negative/positive expansion type could be designed for it.

7 Injection system

7.1 General requirements

The Injection system (INJ) of AdV takes care of the optics after the high power laser, and of the interface between these optics and the laser itself. The whole system must deliver a beam with the required power, geometrical shape, frequency and angular stability. Considering the 180 W power delivered by the High Power AdV laser and AdV sensitivity goal, the general requirements for AdV INJ subsystem are given in the following table (see also [69]):

Requirement	**Value**
Transmission to the ITF	$> 75\%$ TEM_{00} (165 W TEM_{00} after the PMC)
Non-TEM_{00} power	$< 5\%$
Intensity noise	$3 \times 10^{-9}/\sqrt{\text{Hz}}$ at 10 Hz (from PSL)
Beam Jitter	$< 10^{-10}$ rad$/\sqrt{\text{Hz}}$ ($f >$10 Hz)
Frequency noise (for lock acquisition)	<4 Hz r.m.s (from ISC)

An Electro-Optic Modulation (EOM) system will provide the needed RF phase and amplitude modulations (for control and sensing purposes). A power adjustment system (Input Power Control), consisting of a half waveplate and a polarizer (as it is done for Virgo+ power adjustment) will be used in order to tune the interferometer (ITF) input power (important for ITF lock acquisition). A matching and steering system in air will be used to couple the beam into the in-vacuum suspended input mode cleaner cavity (IMC). The IMC will geometrically clean the beam and reduce its amplitude and lateral fluctuation. The resonant IMC for which the length is locked on the reference cavity (RFC) will also serve as a first stage of frequency stabilization. After the IMC an intensity stabilization section will provide the signal for stabilizing the laser RIN (Relative Intensity Noise) and reach the requirements. An in-vacuum Faraday isolator will prevent interaction of the interferometer (ITF) rejected light with the IMC and laser system. An ITF mode matching telescope will give to the beam the correct dimension for matching it with the interferometer. Finally, INJ should provide a way to monitor laser beam properties at different points of INJ subsystem to keep track of every change and be able to accurately adjust the beam provided to the ITF.

7.2 Baseline design overview

This baseline design has been built according to INJ preliminary design study document results [70]. INJ baseline design scheme is given in Fig. 21.

INJ subsystem will include an in-air (outside vacuum) part and an in-vacuum part, namely:

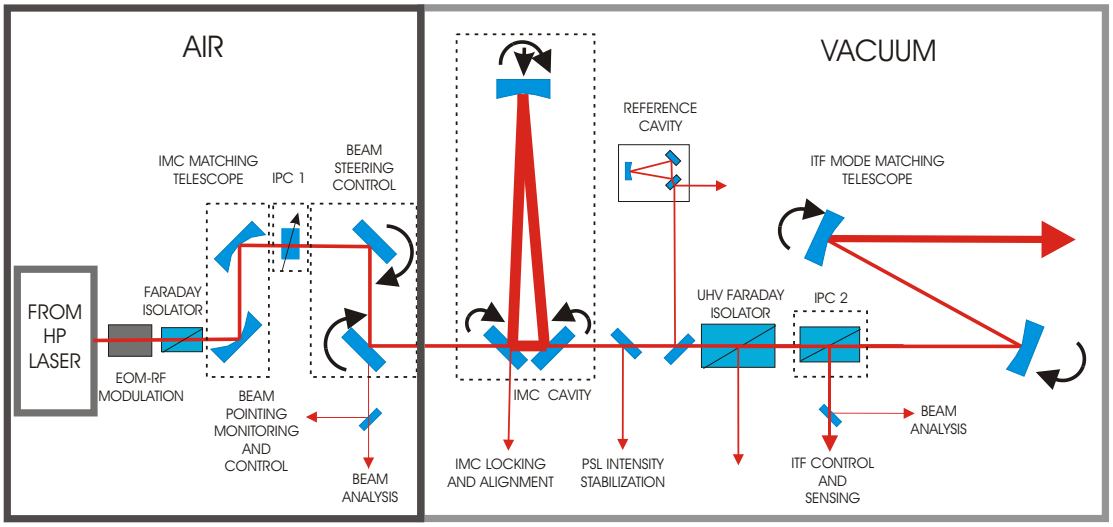

Figure 21: Schematic of AdV INJ subsystem baseline solution.

- In-air

  - EOM for RF modulation (ITF and IMC sensing and control)
  - Faraday isolator
  - IMC Mode Matching Telescope
  - Input Power Control (IPC 1)
  - Steering optics
  - Beam pointing monitoring and control systems
  - Beam Analysis System

- In-vacuum

  - Input Mode Cleaner
  - Power stabilization photodiode
  - Reference Cavity
  - Ultra High Vacuum Faraday isolator
  - Input Power Control (IPC 2)
  - Interferometer Mode Matching Telescope
  - Steering optics

Going a bit more into the details we propose to have the following parts in INJ.

- Electro optical modulation: An EOM system should provide the Radio-Frequency modulations of the laser beam as required by ISC subsystem (for ITF and IMC control and locking purpose). This system should fulfill AdV requirements in terms of phase noise, RFAM (residual amplitude modulation at the modulation frequencies),... (to be provided by ISC)

- Input Power Control (IPC): (see 7.5 for more details) It is used to remotely tune the laser power from low (a few watts) up to full power. This system will be based on Virgo+ IPC system. We propose to adjust the laser power in two places of INJ subsystem:
  - Before the IMC cavity
  - On the suspended injection bench after all the optical elements that are sensitive to laser beam heating in order to adjust the laser power at the interferometer input port.
- Beam Pointing Control: The aim of this control loop is to reduce angular beam jitter and shifts of the beam at low frequency before entering the vacuum vessel. A particular care will have to be dedicated to the actuator selection and actuator mounts design in order to fulfil AdV requirements in terms of beam jitter.
- Input Beam Jitter Monitoring: This system aims to monitor beam shifts and tilts on the whole sensitivity curve bandwidth.
- Input Beam Monitoring system: (see 7.8 for more details) It should provide some useful tools to characterize ITF input beam properties. This system should be used to:
  - Adjust laser beam properties in different places of INJ.
  - Characterize thermal effects in INJ.
  - Potentially provide error signals for a thermal compensation system.
- Input Mode Cleaner cavity: The laser light must be frequency and spatially stabilized before it can be used in the interferometer. The input mode cleaner (IMC) provides active frequency stabilization through feedback to the laser, passive frequency noise suppression above its cavity pole frequency, and passive spatial stabilization at all frequencies. The input mode cleaner also reduces higher order mode content of the laser beam, suppressing beam jitter. We propose to use a 144 meter long triangular cavity with a finesse of 1000 as baseline (see 7.3 and [70] for further details).
- Faraday Isolators: A High power compatible 20mm clear aperture in-vacuum Faraday isolator compensated in terms of thermal lensing and depolarization with the possibility to remotely tune the isolation should also be provided. Its optical isolation at full power should be higher than 40 dB (see 7.7 for further details). Other Faraday isolators to be used in air with a smaller clear aperture.
- Reference cavity (RFC): We propose to keep Virgo RFC that is already compliant with AdV requirements for the first stage of laser frequency stabilization. More details are given in 7.4.
- Mode Matching Telescopes: Two telescopes of this kind should be part of INJ. One should be used to match the beam onto the IMC cavity and the other to match the beam onto the ITF. These devices should be remotely adjustable and use the Input Beam Monitoring system for the fine adjustment of the matching.

A detailed description of a few important parts of INJ is given in the following sections.

7.3 IMC

The main requirements are: to get a throughput higher than 90 % and a residual beam jitter after the cavity of lower than 10^{-10} rad/$\sqrt{\text{Hz}}$ (f >10 Hz). The main issues for this cavity are: thermal lensing effects, throughput and round-trip losses, IMC and PR mirror spurious cavity, radiation pressure.

7.3.1 Geometry of the IMC

The present Virgo IMC is a triangular ring cavity with a high finesse (about 1200). The cavity configuration is flat-flat-curved. Two flat suspended mirrors define the base and act as the input and output couplers. The third mirror (curved one) is suspended in the Mode-Cleaner tower 143.5 m from the injection tower.
For AdV, the triangular configuration is still preferred over other configurations. In order to be compliant with a possible further upgrade of AdV with LG modes, the IMC cavity should consist of an even number of mirrors. But, a 2-mirror linear configuration would require a huge modification of the system and its infrastructure around. A 4-mirror Bow-Tie configuration would make the small angle scattering issue quite problematic as well as the control system. No mature studies push for a change of geometry configuration.
The effect of thermal lensing induced in the substrate of the input mirror of the cavity on the coupling into the cavity is to the first order, independent of its geometry (waist size and length). The astigmatism issue, intrinsic to the triangular configuration, can be considered as negligible for a 150 m long cavity as well as for a 15 m long cavity. The IMC behaves as a first order low pass filter for amplitude and frequency fluctuations. But the pole is as high as 500 Hz for a finesse of 1000 and a length of 150 m, so that this property has to be considered just as a bonus. In conclusion, these 3 criteria, thermal lensing, astigmatism and low pass filtering effect, are not driving the choice for the geometry of the IMC cavity.
A 150 m long cavity implies a FSR of 1 MHz. So, all multiples of 1MHz can be chosen as modulation frequencies for controlling the interferometer. Having a 10 times shorter cavity may be a not so negligible constraint for the choice of these frequencies of modulation.
The light scattered by the IMC end mirror in the opposite direction inside the cavity is a serious issue (see section 7.3.4). Shortening the cavity by a factor of 10 would increase the angle of incidence by a factor 10 but would require the beam to be more divergent into the cavity by a factor of $\sqrt{10}$. At the end, the back-scatter re-coupling factor would be at least a factor of 10 lower depending on the quality of the R.M.S. roughness at large scales of the IMC end mirror. But a shorter IMC would require a huge modification of the current infrastructure (very costly modification). This issue should be mitigated by other means: better polishing of IMC end mirror and better isolation of the Faraday.
The beam waist size is currently 5 mm. Other sizes which respect the properties of non-degeneracy of the cavity are possible (3.7, 4.3 or 5.6 mm). But they don't offer any particular big advantage with respect to the current size.
In conclusion, the geometry of the IMC for AdV should be unchanged. Shortening the

cavity would bring a too small benefit with respect to its actual cost.

7.3.2 Thermal effects

Using the last models of the thermal lensing induced by the power absorbed in the coating, it is possible to set a higher limit for the power absorbed by the coating in order not to affect the coupling of the input beam into the IMC cavity. To get a coupling higher than 90 %, the power absorbed should be lower than 100 mW. For a finesse of 1000 and an input power of 180 W, the power absorbed by the coating does not exceed 100 mW if its absorption is 2 ppm. That is feasible considering the experience of LMA. But that sets a higher limit for the finesse of the cavity if one wants to keep the thermal effects introduced by the IMC cavity negligible.

7.3.3 Throughput and losses

One can easily compute what is the throughput of the cavity depending on its finesse and its round-trip losses. This is represented in the Fig.22.

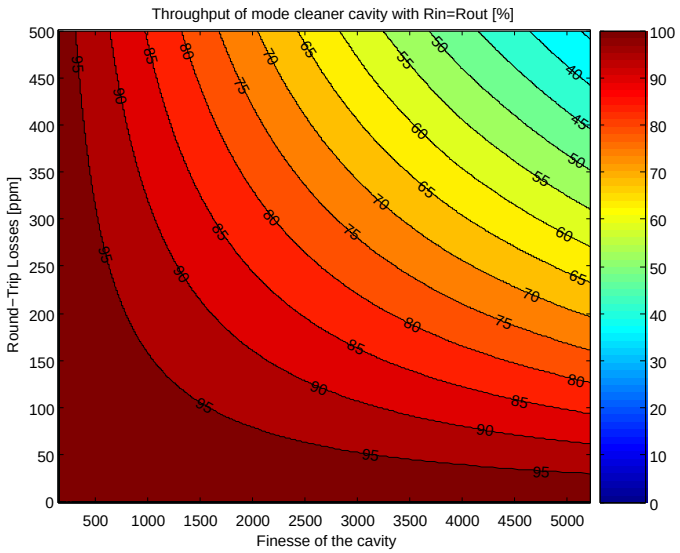

Figure 22: IMC throughput with respect to the finesse and the round-trip losses.

So the throughput is higher than 90 % if the losses are lower than 300 ppm. Recent results with the DarkF simulation program reproduced quite well the actual losses measured in the current cavities. Using the current map of the mirrors, and dividing their amplitude by a factor 3, it demonstrates that the losses should be lower than 100 ppm in this case. So, the best effort should be required for the polishing of the substrates in order to have losses having a limited impact on the throughput of the cavity.

7.3.4 Scattered light in the IMC

The incoming light impinging on the mode cleaner end mirror is scattered by the mirror surface, which is not perfect. Thus, due to the small angle of the mode cleaner (about $3\,10^{-4}$ rad), a part of the scattered light can propagate in the opposite direction and be sent back to the laser. The biggest problem is that this light can interfere with the light reflected by the ITF and create fringes on the sensors in reflection of the IMC. This interference can spoil the performances of the IMC control and add some noise to the laser beam sent to the ITF [71]. This problem can be modeled by a spurious cavity IMC-PR. The effective reflectivity of the IMC is proportional to the square of the finesse and the backscattered coupling factor. It can be then reduced by the Faraday isolation ratio. The backscattered coupling factor is the key parameter. For the same mirror, this parameter can vary by one to two orders of magnitude depending on the angle around its axis of symmetry due to the asymmetric phase map defect. For the current mirror, the factor has been estimated to be 2.5 10^{-7}. And with the current Faraday isolation of around 37 dB, the backscattering issue is circumvented. Assuming that the isolation ratio for AdV should be a bit lower due to the increase of power passing through the Faraday (40 dB demonstrated), the polishing of the IMC end mirror should be done with the maximum care to decrease drastically the amount of light scattered in the opposite direction.

7.3.5 High order mode filtering

The high order mode filtering depends directly on the finesse. In particular this is important for the beam jitter noise filtering. Beam pointing noise specifications for AdV are 10^{-10} rad/$\sqrt{\text{Hz}}$ after the input mode cleaner, considering that the input mode-cleaner controls are stable enough not to reintroduce beam jitter noise due to suspended Mode-cleaner motion. This is 10 times more stringent than for Virgo. This will probably require the external benches to be suspended as well in order to avoid the current resonances of the system (optical bench+legs). On the other hand, the requirement may be relaxed once everything has been taken into account: the final requirement should be derived from the requirement on power fluctuations after the OMC and depends on the additional filtering effect of the NDRCs. Final computations will drive the final choice for the IMC finesse.

7.3.6 Radiation pressure

The IMC and ITF mirrors will be subjected to increasing radiation pressure as the input power is increased. For a finesse of 1000, and an input power of 180 W, the force applied is 400 μN inducing a frequency shift of 35 MHz for an IMC end mirror of 1.4 kg. The dynamic of the master laser correction is largely sufficient, so that there is no problem for the lock acquisition. On the other hand, one should particularly pay attention to alignment control issues as the radiation pressure torque effect. A detailed analysis of the problem has been done in the vertical plane cross-checked with measurements. This

control should be stable for an IMC end mirror mass of 1.4 kg [72]. Further analysis is required for the control in the horizontal plane. Some safety margin should therefore be considered for the time being. An IMC end mirror of 3 kg is advised since it should not require a complete modification of the payload.

7.3.7 Conclusion

No change of geometry is advisable for AdV IMC. On the other hand, the best effort should be made to have a low absorption of the coatings (around 1 ppm), and the best polishing available (roughness below 1 nm RMS) to avoid thermal effects, significant losses and a large backscattered light re-coupling factor. The finesse should be around 1000, its exact value will be adjusted once a better modeling has been established for assessing the beam jitter noise requirements. More technical details are given in INJ Preliminary design study document [70].

7.4 Reference cavity (RFC)

The reference cavity should be used as in initial Virgo in the first stage of frequency stabilization. According to the requirements given by ISC (see 7.1) there is no need to change the RFC since the current one is already compliant with AdV requirements for the lock acquisition of the 3km long Fabry-Perot cavities (Measured laser frequency noise (first stage of frequency stabilization) = 3 Hz rms). We propose to keep the RFC (32 cm long rigid triangular cavity made in ULE) in the lower part of the suspended injection bench. This will ensure a good isolation of the reference respect to acoustic and seismic noise. On figure 23, there is a picture of Virgo RFC. The laser frequency prestabilization loop will be carried out by PSL subsystem (see sec.6 for more details).

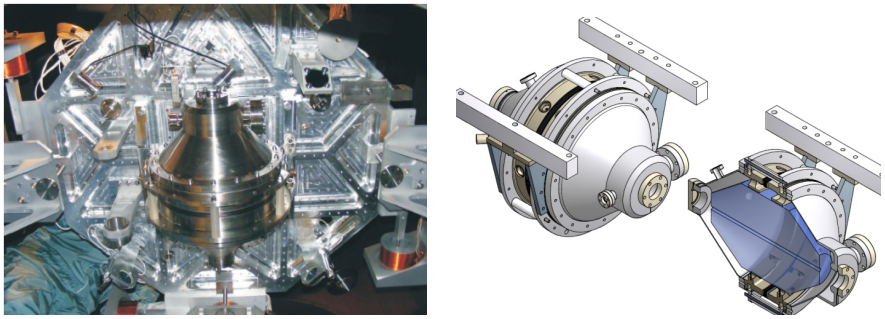

Figure 23: Left: Picture of Virgo RFC attached to the lower part of the Suspended Injection Bench : in AdV baseline solution, the RFC should remain the same and should be put under vacuum and suspended as for Virgo; Right: 3D view of the reference cavity (rigid triangular cavity).

7.5 Input Power control

We propose to include in INJ subsystem, a dedicated system that enables to change the interferometer (ITF) input power, while keeping the INJ system always with the same power level [70]. This will insure to keep the same thermal effects in INJ and the control loops at a constant and optimized power level. In order to save commissioning time, we also propose to install such a system just before the IMC cavity to facilitate its commissioning. This system consists of a remotely controllable half wave plate placed between two polarizers. It will be associated with two high power and low diffusing beam dumps that dump light reflected by the two polarizers (light going to and coming back from the ITF). The technical realization will include two Thin Film Plate polarizers in fused silica of two inches aperture and an optically contacted wave plate. In this way, we will reach an extinction of higher than 40 dB, which means a minimum of transmitted light by the system of 20 mW for an input power of 200 W. This system will not introduce any noticeable thermal focusing (higher than 100 m at full ITF power). The associated beam dumps should withstand a power of 200 W without breaking and exhibit scattering in the 100 ppm range [73] (further details on this kind of beam dump is given in [70]). The IPC 1 and related beam dumps should be placed on the external bench (see figure 21). Concerning the IPC 2, it should be placed under vacuum while its associated beam dumps should be placed outside the vacuum vessel for thermal concerns.

7.6 EOM and RF Modulation

DC detection is baseline for AdV. Nevertheless, RF modulation will be used for the control of the interferometer, both for longitudinal locking and alignment. The main difference between the EOM to be used in AdV and Virgo resides in that the power that the first EOM will have to withstand will be almost 10 times higher (180-200 W instead of 20 W). Thermal effects will become more significant [74], and the choice of RTP (Rubidium Titanyl Phosphate) or KTP (Potassium Titanium Oxide Phosphate), less absorbing materials than Lithium niobate (LiN_bO_3) currently used in EOM systems, would be recommended [75]. Some measurements given in [70] confirm that KTP and RTP are the most suitable candidate Electro-optic crystals for use in AdV since they exhibit less thermal lensing than other materials due to their low absorption (of the order of 50 ppm/cm). A careful selection of the crystals will be required since there could be significant differences from one sample of RTP or KTP to the next. Requirements in AdV for EO modulation will also be different: many of these parameters will affect the driving electronics and signal generator choice. Indicative numbers for the single sideband noise requirements (modulation phase noise) can be found in [76], and for modulation index noise (amplitude noise) in [77]. Four modulation frequencies will be used in AdV (three for ITF control and one for IMC lock), either for control and for monitoring. In ISC baseline design, two amplitude modulations and two phase modulations of the laser beam are required. The general principle schemes of phase and amplitude modulators proposed for AdV are presented in figure 24.

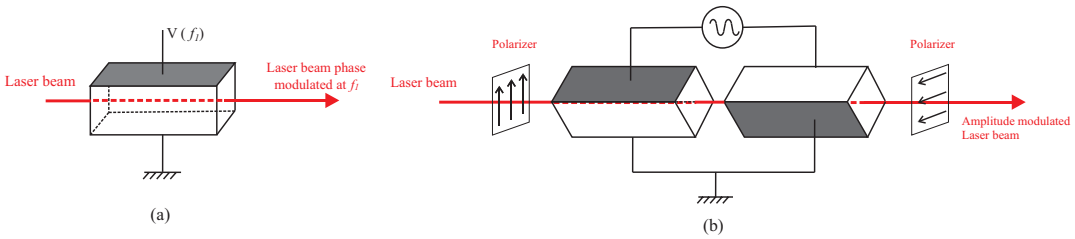

Figure 24: a. Phase modulator principle; b. Amplitude modulator principle.

The phase modulator should be based on the Pockels effect as it is done in Initial Virgo. Prototypes are being built and should be ready and characterized before the end of 2009. For the amplitude modulator, it basically consists of an electro-optic modulator followed by a polarizer. If the input polarization is oriented at 45° to the crystal axes, the applied voltage will produce a variable phase delay between the ordinary and extraordinary field components, simulating a voltage-tunable waveplate. Thus, the modulation of the intensity is a square sine function after the polarizer. Birefringence variations due to temperature changes is an issue for this kind of modulator especially in the case of AdV since the laser power passing through the crystal should be of the order of 180 Watts. In order to suppress this spurious effect, we can use two matched crystals arranged in series with their applied electric fields oriented at 90° relative to each other (see figure 24.b). A prototype amplitude modulator compliant with AdV laser power should be built by 2010.

7.7 Faraday isolator

Light back reflected by the ITF towards the IMC has already been an issue in Virgo. The solution for this problem is the use of an in-vacuum Faraday isolator placed between the IMC cavity and the ITF.
With the higher AdV laser power (180 W input power), a standard Faraday isolator will exhibit loss of optical isolation due to thermally induced birefringence and very high thermal lensing [73]. It will also experience a variation of its mean rotation angle due to heating of the magneto-optic medium (TGG) that also induces a loss of isolation. In order to reach a good level of optical isolation (> 40 dB) a specifically designed Faraday isolator has to be used, including depolarization compensation and a passive correction of its thermal lensing.
Such a system will be developed in collaboration with Novgorod IAP group that has extensive experience in this field [78], [79] and developed a prototype for LIGO that demonstrated 49 dB of isolation with more than 100 W of input power [80]. The schematic of the AdV Faraday isolator that will be based on the same design is shown in figure 25. It consists of an input polarizer, a half waveplate, two TGG crystals rotating the polarization by 22.5° and separated by a -67.5° quartz rotator, an end polarizer and a DKDP plate.

By using two TGG crystals separated by a quartz rotator, it is possible to limit the effects of thermal depolarization [81]. The variation of mean angle rotation of the two TGG crystals can be compensated by slightly turning the half wave plate (this can be done remotely). This also enables to account for the modification of isolation observed with the whole setup when it is tuned in air and then placed in vacuum [82] (where thermal dissipation is very different). Finally, a DKDP (Deuterated Potassium Dihydrogen Phosphate, KD_2PO_4) plate is used to compensate the thermal lensing created inside the TGG crystals, thanks to its large negative thermo-optic coefficient [83]. A prototype of this isolator will be carried out in 2009 and should have the following characteristics:

- withstand high average power (300 W) on long periods;
- an optical isolation higher than 40 dB at full power;
- residual thermal lensing higher than 100 m;
- provide good transmission (at least 95%)
- clear aperture of 20 mm.

A design study of this device has already been completed [84] and its expected dimensions make it feasible for use on the Suspended Injection Bench (see a candidate prototype on figure 25 with L=d=130mm, weight=12 kg).

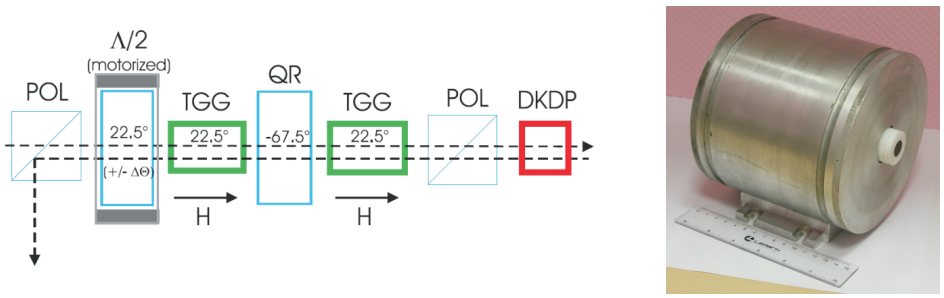

Figure 25: Left: principe of the compensated High Power in-vacuum Faraday isolator. Right: prototype of central part of the isolator (Faraday rotator) with TGGs and magnetic housing.

7.8 Input Beam Monitoring system

Beam monitoring is an essential part of INJ. It will allow to assess the quality of the beam at all stages of the injection system. It will be used for the optimization of the optical alignment, for the monitoring of thermal effects and may be used as an error signal for any subsequent active compensation. The principal aberrations that will be present

in the injection system are focus and astigmatism. In addition it will be important to measure also higher order modes, as it is the global quality of the beam that defines the efficiency with which it is coupled into the IMC and ITF. The beam comprises the carrier and sidebands. These fields could be modified differently due to the numerous cavities in the system. Therefore, in order to have a comprehensive understanding of the system and the necessary error signals to compensate, it is necessary to have a complete picture of the amplitude and phase for each of the fields in the beam. The beam monitoring system will comprise two complimentary instruments:

- Shack-Hartmann Wavefront Sensor: This instrument uses a lenslet array to measure local wavefront tilt. It has no moving parts and gives real-time wavefront measurements with an absolute accuracy of $\lambda/100$. It is a mature technology for which EGO has hands-on experience.
- Phase Camera: This is a scanning heterodyne interferometer developed by the Pisa group which is currently installed in Virgo+. It is capable of measuring the spatial distribution of amplitude and phase for each individual field.

The beam will be measured at four different stages of the INJ subsystem in order to decouple the different effects:

- Output of EIB: Thermal effects on EIB, Beam quality entering IMC.
- Transmission of IMC: Thermal effects in IMC, Potential error signal for active compensation.
- Input of ITF: Thermal effects in Faraday, Beam quality entering ITF
- Reflection of ITF: Thermal effects inside ITF.

All four beams will be sent to the EIB where they will be monitored by one common beam monitoring system (see Fig. 26).

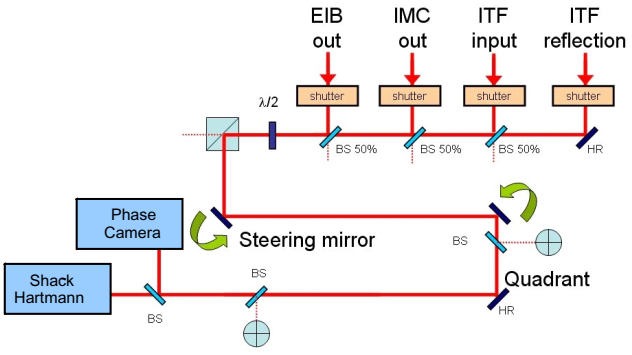

Figure 26: Input Beam Monitoring system

8 Mirrors

As it is shown in fig. 2, mirrors play a crucial role in the sensitivity of AdV. On one side the mechanical losses in the coating determine the quality factor of the mirror and as a consequence the displacement of the mirror surface due to its thermal vibration. On the other side the optical losses in the coatings determine the amount of power which is lost in the Fabry-Perot cavity and as a consequence the power that is stored in the recycling cavity. This quantity determines the quantum noise which is expected to limit the sensitivity at the higher frequencies. R&D was done at LMA to improve the mechanical performances of coating without degrading the optical performances. Titanium doped Ta_2O_5 coatings recently developed at LMA are the best solution known so far [85]. The AdV baseline design foresees the use of mirrors, for the Fabry-Perot cavities, 35 cm in diameter and 20 cm thick i.e. mirrors having the same diameter as Virgo but twice as thick. A larger substrate is likely to be required for the beam-splitter as this component lies at 45 degrees with respect to the beam axis. A substrate 55 cm in diameter and 6.5 cm thick has been considered. In the AdV baseline, non degenerate cavities will be used for the power recycling and signal recycling. Instead of a large mirror (35 cm in diameter and 10 cm thick) like in Virgo, three smaller mirrors will be used to realize these two cavities (diameter between 5 and 15 cm). Although there are 6 mirrors instead of 2 for these cavities, the cost will be comparable: the cost increase of the polishing will be compensated by the decrease of the bulk silica cost. At last, due the thermal compensation implemented in AdV, two compensation plates (CP) will be necessary.

8.1 Substrates

The AdV baseline foresees the use of fused silica for the mirror substrates. Tests on sapphire were done at LMA in the context of the Advanced LIGO pathfinder. The results obtained favored the choice of fused silica [86]. No alternative material is being considered today by Virgo. On the other hand a new type of fused silica with smaller absorption is available today. The bulk absorption for this material is 3 times smaller than the one used for Virgo (measurements made at LMA) and the other performances (Quality factor, index homogeneity, residual strain) are still the same. The cost of this new type of Silica is comparable to the one used for Virgo. Reducing the absorption in the substrates is certainly of interest as the power absorbed causes thermal lensing in all transmissive optics. The problems increases with the power stored in the interferometer and with the thickness of the substrates. On the other hand one should remind that so far thermal effects are dominated by coating absorption, and this will be enhanced by the high finesse of AdV. From this point of view it is more important to improve the absorption of the coatings than to improve the losses of the silica. Both for the old type of silica used for Virgo as for the new one recently developed, it is possible to obtain pieces of the size requested by the AdV baseline.

Reference solution for AdV substrates For the AdV baseline, it has been decided to use a high quality fused silica for the input mirror and the beam splitter (respectively Suprasil 3002 and Suprasil 3001) as these optics transmit a relatively large amount of power (of the order of 2 kW). Other transmissive optics (compensation plates CP, mirrors PRM 1 and SRM 1 of the non degenerate recycling cavities) will be also in Suprasil 3002. Fused silica of a lower optical quality will be considered for the end mirrors as in this case the mirrors are reflecting most of the light (baseline Suprasil 312). The only constraint in this case is the substrate mechanical quality factor that has to be sufficiently high to avoid increasing the thermal noise above the level determined by the mechanical losses in the coating. Fused silica of lower mechanical and optical quality (baseline Herasil 102) can be used for the mirrors of the power and signal recycling cavities which will work in reflection (PRM 2 and 3, SRM 2 and 3) as a relatively small power is transmitted trough this optic and the interferometer output is less sensitive to the thermal noise affecting these masses.

8.2 Polishing

Traditionally, the quality of polishing is characterized by two different parameters: the flatness and the micro-roughness. The first parameter gives the rms of the difference between the perfect surface (typically a sphere) and the actual surface as measured by phase map interferometer (i.e. for spatial wavelengths going from about 1 mm, up to the radius of the mirror). For Virgo this parameter was measured to be in the range of a few nm [87, 88]. The second parameter gives a measurement of the mirror surface roughness at small scale lengths (from a few microns, up to about 1 mm). For the Virgo mirrors this parameter was found to be of the order of 0.05 nm. The distinction between these two different length scales originates in the fact that different instruments are used to measure them: both effects contribute to scatter the light from the fundamental mode to higher order modes. They generate losses and extra noise. These polishing losses will play an even more important role in AdV due to the higher finesse of the cavities. Depending on the difference in the losses between the two cavities they could be the source of finesse asymmetry and contrast defect thus modifying the constraints on other subsystems. According to the simulation of the Virgo interferometer recently done at Nice and ESPCI [89], using the real mirrors maps measured at LMA, the lack of flatness represents one of the main origin of losses in the cavity. The value deduced from the simulation amounts to 250 ppm per round trip. For comparison the measured losses per round trip, as deduced from the measurement of the recycling gain, amount to 500 ppm. The additional losses measured are thought to be due to the mirror contamination (this remains to be verified). Anyhow the losses foreseen by the simulation alone exceed by a large fraction the losses assumed in the AdV baseline ($\sim$75 ppm per round trip).

Reference solution for AdV polishing For AdV, the polishing strategy has been defined as follows. The classical steps of polishing will be done by external companies. Then, the second step will consist in improving the mirror surface figure by using the so-called

corrective coating technique. This technique, originally developed at LMA, consists in measuring the mirror surface map and correcting it by adding an additional layer of silica wherever is necessary. An R&D program about corrective coating had been supported at LMA during the first R&D program launched by EGO back in 2002. The corrective coating technique was tested on a 150 mm diameter flat mirror with good performances (RMS wavefront: 0.9 nm, Wavefront PV: 9 nm). In order to reach the AdV specifications on the flatness, an additional investment will be required to develop a new robot for the Virgo large coater in Lyon. This study is done with the LAPP group. But this is an investment for the future as other mirrors upgrades can be done using this technique.

8.3 Coating

The mirror coatings are certainly the most sensitive component of the mirrors and among the most important in the interferometer as they determine both the total mechanical losses of the mirrors and their optical losses. As mentioned above an R&D program is ongoing since several years at LMA and is still supported by EGO. At present, the lowest mechanical losses measured for Ta_2O_5 coating are those obtained with Ti doped Ta_2O_5 and amount to about 1.6 to 1.8 10^{-4} (the typical value is 2 10^{-4}). [85].

Reference solution for AdV coatings It is clear that a further decrease of the mechanical losses will directly benefit to the sensitivity of the detector. One of the main difficulties in this context is to find materials with lower mechanical losses without degrading the performances in terms of optical losses. The best available recipe will be used for the AdV mirror coating. Another option to reduce the mechanical losses consists in optimizing the thickness of the different coating layers (Ta_2O_5 and SiO_2). Since the Ta_2O_5 is the more lossy material, it is possible to reduce the mechanical losses of the multi-layer by reducing the amount of Ta_2O_5 and increasing the amount of SiO_2. For a given required reflectivity it is possible to find an optimum combination. Recently at LMA a mirror was coated using this technique and delivered to Caltech. Nevertheless, the reference solution for the coating design is the quarter wave stack as the AdV sensitivity curve is calculated with this assumption. Moreover, with a quarter wave design it is easier to adjust the reflectivity needed at the wavelength of the auxiliary laser used for lock acquisition.

The absorption losses of the coatings play also an important role as they determine the power absorbed in the test mass and thus the thermal lensing effect. The lower are the losses in the coating the lower is the required thermal compensation. Since the first generation of VIRGO mirrors the absorption in the coating has been reduced. An absorption level around 0.3-0.4 ppm is done currently on high reflectivity mirrors (IM, EM) thanks to the use of Ti doped Ta_2O_5 (baseline value). Nevertheless, due to the increase of the finesse, the absorption in the coating is likely to remain the main origin of the mirror heating. At the present time, we can not know if it is possible to decrease more this level of losses. Due to the higher reflectivity of the input mirrors it will be important to check that the transmission of the two mirrors and, more critical, the losses in both arms are equal. Otherwise, the asymmetry in finesse and power on the dark

	Input Mirror IM	End Mirror EM	Beam Splitter BS	Compensation Plates CP	Non degenerated Power and Signal recycling Cavities		
					PRM3/SRM3	PRM2/SRM2	PRM1/SRM1
Number of parts	4	4	3	4	3	3	3
Fused Silica Nature	Suprasil 3002	Suprasil 312	Suprasil 3001	Suprasil 3002	Herasil 102	Herasil 102	Suprasil 3002
Diameter	350 mm	350 mm	550 mm	280 mm (TBC)	350 mm	150 mm	150 mm
Thickness	200 mm	200 mm	65 mm	100 mm (TBC)	100 mm	100 mm	100 mm
Roughness Reflective side	<1 Å RMS	<1 Å RMS	<1 Å RMS	<1 Å RMS	<1 Å RMS	<1 Å RMS	<1 Å RMS
RMS Flatness Reflective side	0.5 nm RMS (TBC) ∅ 150 mm	0.5 nm RMS (TBC) ∅ 200 mm	3 nm RMS (TBC) ∅ 250 mm	3 nm RMS (TBC) ∅ 150 mm	3 nm RMS (TBC) ∅ 150 mm	3 nm RMS (TBC) ∅ 100 mm	3 nm RMS (TBC) ∅ 100 mm
Transmission Reflective side	0.7 % (TBC)	# 10 ppm (TBC)	50 %	100%	# 10 ppm (TBC)	# 10 ppm (TBC)	TBD

Figure 27: A summary of the main features of the AdV mirrors.

fringe might be too large. Specifications for these parameters will have to be defined. In case the asymmetry is too large, then an imperfect AR coating on the other face of the substrate provides a way to improve the symmetry by tuning the reflectivity of the input mirrors. In case this is not required, 'perfect' AR and a wedge between the two faces of the substrates might be used. In both cases the specification for the AR coatings will have to be determined. In the second case the presence of larger wedges will have to be taken into account when designing the tools required both for the coating and for the metrology. The table in fig. 27 summarizes the main characteristics of the different type of mirrors for AdV.

8.4 Metrology

The metrology tools, necessary to completely characterize the Virgo mirrors, have already been developed for the first mirror generation (absorption, scattering, transmission, wavefront, radius of curvature, roughness, point defect detection). Since 2002, improvements of these benches have also been obtained. The size (diameter greater than 400 mm for the beam splitter) of the AdV mirrors will impose modifications of the several sample holders to be able to map the scattering, the transmission, the reflection and the absorption losses, because of the weight increase. But these changes are possible and not too expensive. To be able to measure the flatness of the AdV substrates and mirrors at the level required (RMS flatness lower than 1 nm), a new bench will be developed to measure wavefronts at 0° and 45° (for the beam splitter) below 1 nm RMS with a better accuracy and reproducibility. It will be coupled with a stitching software to measure large components. This bench is also crucial for the "corrective coating" to be efficient. New

mechanical mounts have to be manufactured for the metrology purposes.

8.5 Cleaning

During the coating process the mirrors are cleaned several times. Due to safety reasons, the cleaning procedures used for Virgo cannot be simply transposed to the larger mirrors that will be used in AdV. A different cleaning procedure will have to be developed. A new procedure has been identified and its development had been already proposed and supported by EGO in the context of the 2nd R&D program. The implementation of this new cleaning procedure will require some investment at LMA. Before being sent to the site the mirrors will have to be protected against contamination and properly packed. Special boxes adapted to the larger size of the AdV mirrors will have to be procured.

9 Thermal compensation

9.1 General requirements

The TCS will correct for a wide range of thermal effects in core optics. It must reduce thermal effects to a level that allows AdV to acquire the lock and such that the sensitivity of the detector is not spoiled. TCS should provide as much flexibility as possible for corrections, to help in case some optics should not meet the specifications (mirror radius errors, higher or non-uniform absorptions). Based on the experience of Virgo/Virgo+, it should be designed so that most of the apparatus lives outside vacuum and can be easily upgraded as new understanding of the IFO is realized. The system will comprehend sensors to monitor thermal effects in core optics.

9.2 TCS baseline design

In the test mass, the optical power is predominantly absorbed by the HR coating and converted into heat, producing a gradient of temperature inside the substrate. Two different effects originate from the heating of the test mass:

- nonuniform optical path length distortions (thermo-optic effect, also termed thermal lensing) mainly due to the temperature dependency of the index of refraction.
- change of the profile of the high reflective surface, due to thermal expansion (thermo-elastic deformation).

In the case of Virgo/Virgo+ the main thermal effect is the thermal lensing, affecting the Power Recycling Cavity (PRC): in presence of thermal lensing, which changes the cavity mode, the input laser no longer matches the PRC cavity, the coupling coefficient between the laser TEM_{00} and the cavity TEM_{00} is less than one. In the case of Advanced Virgo, the other thermal effect will also be relevant due to the much higher circulating power in the FP cavities. Thermal expansion will change the profile of the high reflective surface. A bump will raise in the center of the test mass faces, making their surface profile non-spherical. Given uniform absorption at the .5 ppm level expected in advanced detectors, this departure from sphericity will not make the arm cavity resonant modes significantly non-Gaussian. The cavity becomes less concentric, and the spot sizes at the mirrors will shrink. The resulting increase of thermal noise has been estimated to be of the order of 15% [90]. To maintain the arm cavity mode structure, it is necessary to control the radii of curvature of all test masses.

The thermal effects will then create distortions both in the recycling and in the Fabry-Perot cavities:

- wavefront distortions in the SRC and PRC cavities;
- HR surface elastic deformations in both ITMs and ETMs.

TCS needs to compensate for both effects, by acting on both input and end test masses.

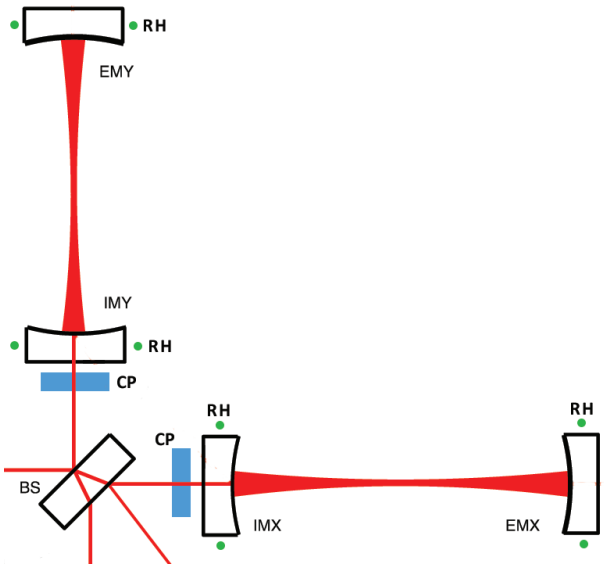

Figure 28: AdV TCS layout: the green dots represent the ring heaters, the blue rectangles represent compensation plates.

The TCS actuation scheme in shown in Figure 28. The wavefront distortions in the recycling cavities are corrected by shining a suitable heating pattern generated by a CO_2 laser on the Compensation Plate (CP), a transmissive optic placed in the RC. To control the radii of curvature of the test masses, a shielded ring heater (RH), placed around each TM, will be used.

Thermal effects will arise also in the beam splitter. The BS contribution to thermal lensing in the recycling cavities is of the order of 5-10% of the total effect, depending on the RC gain (23.5 or 46) and it can be compensated by the compensation plates [91]. For this reason, no direct actuation on the beam splitter is proposed.

Each optic will be monitored in reflection to measure HR surface deformation, while each ITM-CP pair will be monitored in transmission to measure phase profiles (see section 9.5).

9.3 Ring heater

Compensation and control of the test mass HR surfaces will be done by ring heaters, embedded in the reference mass. There will be four of these: one around each test mass, toward the AR face. The test mass ring heaters control the arm cavity mode shape. The input mirror ring heaters also provide limited compensation of thermo-optic effect in the recycling cavities.

Position of a simple RH along the barrel of the test mass has been optimized through a coupled thermal-structural finite element analysis [92].

It has been found that if the position of the RH is at about 15cm from the TM HR surface, the power required to recover the cold state ROC is minimized. This will minimize any heating of the reference mass. It must be underlined that the simple ring heater is a very unefficient solution, since only a small fraction of the emitted power reaches the TM. By putting the ring heater into the focus of a parabolic reflecting shield, the amount of emitted power reaching the TM will increase, thus decreasing the required total emitted power, and avoid unwanted heating of the reference mass.

The design with the RH around the TM is less sensitive to actuator noise fluctuations than designs that heat the HR surface, because the heating is entirely on the substrate far from the ITF beam, and the radiation pressure averages to zero over the test mass. However, there is a slight coupling of overall power fluctuations to HR surface displacement. A test mass ring heater changes the radius of curvature of a test mass's HR surface by flexing the mirror. Since the position of the centre of the HR surface relative to the test mass centre of gravity varies with the flexure, any power fluctuation in the ring heater will create displacement noise [93]. The ring heater thermal inertia will passively smooth power fluctuations on its input supply, this should make easier to meet the noise requirements. Simulations to optimize the geometry, position and shielding of the RH, and to evaluate possible departures of the mirror surfaces from sphericity are in progress.

The ring heater can in principle compensate for thermal aberrations in the recycling cavity, as demontrated by R. Lawrence [94], thus avoiding the use of CPs and CO_2 laser projectors. But it cannot compensate at the same time for both thermal lensing and thermal effects in the Fabry-Perot cavity. Moreover, it cannot compensate wavefront distortions in case of non-uniform absorptions.

9.4 Compensation plate

A TCS has been installed in Virgo+, based on a pre-stabilized CO_2 laser projector, that shines a heating pattern onto the HR surface of both the input mirrors. The power stabilization level, necessary to be compliant with the Virgo+ sensitivity requirements, has been estimated to be of the order of $10^{-7}/\sqrt{\text{Hz}}$ @ 30 Hz [95].

It has been shown [96] that, in principle, it would be possible to act with a CO_2 laser on both faces of the ITM and correct both wavefront distortions and HR surface deformations. But, in order to keep the TCS noise below the sensitivity, it is necessary to reduce the RIN of the CO_2 laser at the level of $10^{-8}/\sqrt{\text{Hz}}$ @ 50 Hz. This level of RIN is one order of magnitude below what it is possible to achieve.

Thus the necessity to introduce a new transmissive optic (Compensation Plate), placed in the recycling cavity, which to act on with the CO_2 laser. Since CPs live entirely within the recycling cavity and have no HR surfaces, the effect of the actuator noise is much less important on a CP than on a test mass. The coupling of the carbon dioxide laser noise

to the IFO noise is much lower. Calculations of the noise coupling of the CP have been performed [93] and show that the power stabilization level required would be of the order of $10^{-6}/\sqrt{\text{Hz}}$ @ 100 Hz, less stringent than the Virgo+ case.

The CP interacts directly with the interferometer beam. As such, it must satisfy requirements like those of a core optics with respect to displacement noise, absorption and scattering, index homogeneity, antireflection coatings, and the like. In order to minimize etalon effect in the CP, a wedge is foreseen. The exact value will be defined in the frame of the general optical design of the interferometer. In the following considerations, a wedge in the range from 0 to a maximum of 17 mrad (1 deg) has been considered, taking in each calculation the most conservative value.

The noise injected by an individual CP is injected only into a single arm of the recycling cavities. Because the CP has no HR surfaces, the noise motion requirements for the CP are relatively modest. In particular, the IFO sensitivity to motion of the CP along the beam axis is negligible, assuming the CP motion is equal to the RM motion. This has been verified through an Optickle [97] simulation, set up with the same parameters used for the LSC design [98], considering the worst case, when the CP is not wedged.

It has been noticed [99] that if a plate with faces perpendicular to the beam is moving longitudinally in a cavity, it induces power fringes; with 100 ppm AR coating, the relative power variations will be 4%, on a time scale of 1 s. These variations may fool the DC locking of DARM. A wedged or tilted CP will avoid this effect.

Because the CP will be wedged, there will be sensitivity to transverse motion. If we assume a maximum wedge of 1 degree, the transverse noise requirement is $8 \cdot 10^{-17}$ $\text{m}/\sqrt{\text{Hz}}$ around 300 Hz, with a safety factor of 10 with respect to the AdV sensitivity. Since the CP is foreseen to be suspended from a long SA tower, this requirement is expected to be easily met.

The effects of the presence of a CP on the Automatic Alignment control system have been evaluated [98]. The major consequence of using a wedged compensation plate arises when the face of the CP looking at the F-P cavity is slightly misaligned with respect the IMX HR face. The misalignment produces an amount of higher order modes which corresponds to a not minor cavity mirror misalignment. If we lock the cavity, longitudinally and angularly, a CP front face misalignment induces the Automatic Alignment control loop to misalign the cavity mirror of about 1 nrad for a 10 μrad of CP misalignment. This effect disappears for CP misalignment larger than 0.1 mrad, thus in order to avoid it the CP front face should be misaligned, with respect the IMX front face, more than that.

The CP etalon tuning, also in the worst case with no wedge, produces a very small optical gain variation on the Automatic Alignment error signals, of the order of 1 per thousand.

The thermal effects on the CP mirror, which essentially modify the ROC of the CP to ~ 2700 m, when the ITF is operated at full power, do not introduce strong variations on the previous results.

9.4.1 CP geometry and position

The geometry and position of the CP have been defined by optimizing the TCS performances. The parameter used to describe the compensation level are the coupling losses, related to the mismatch of the FP cavity beam with the RC beam. This is the same parameter used to evaluate the astigmatism in the RCs.

Diameter of the CP has been fixed to 280 mm. In order to investigate the effect of the CP thickness on the TCS performance, we considered a setup where CPs are far from the TMs [91]. We considered different thicknesses of the CP (10 cm, 6.5 cm, 3.5 cm). In these set-ups the RH is always on to correct the ROC, the position of the RH is set to maximize its efficiency. RH power is fixed at 16.5W to recover the cold ROC. Results are summarized in the table below.

Thickness (cm)	**CP mass (kg)**	**Minimum losses (ppm)**
10	13.5	3000
6.5	8.8	1300
3.5	4.7	300

Table 10: *Minimum coupling losses as a function of the CP thickness*

These results clearly show that a thin and light CP is better than a thick and heavy one. This is due to the fact that a thick CP will radiate more heat from its lateral surface than a thin CP. For this reason, the CP thickness has been set to 3.5 cm. A preliminary analysis of the resonance mode for an unconstrained 3.5 cm CP, shows that the lowest mode (butterfly mode) is at 3 kHz.

The effect of thermal interaction between the CP and the test mass has been evaluated, by changing the distance between the test mass and CP. Consequences of the CP-TM radiative interaction are that:

- The heat falling on the ITM AR face is nearly uniform, but heat flow out of the barrel creates a radial temperature gradient

- This radial gradient adds to that due to the YAG absorption

- Thermal lensing is increased and ROC is reduced

- ROC depends also from the CO_2 power

- Less RH power is needed to keep the cold state ROC

- RH and CO_2 power are strongly coupled.

Results are summarized in the table below.

From the above considerations, the minimum distance between CP and TM must be about 20 cm. In order to further reduce the effect of the radiative coupling between CP

CP-TM distance (cm)	RH power (W)	dROC/dP$_{CO2}$ (m/W)	Minimum losses (ppm)
1	2	-0.9	$1.3 \cdot 10^4$
10	8	-0.5	$6.2 \cdot 10^3$
20	12	-0.26	$2.2 \cdot 10^3$

Table 11: *Minimum coupling losses as a function of the CP-TM distance*

and TM, the possibility to put a reflecting shield on the internal surface of the reference mass is under investigation.

The above results were obtained considering a CO_2 heating pattern produced by an AXICON based telescope. These profiles may not be the optimal ones [100, 101], an optimization of the heating pattern is ongoing.

In principle, the CP could be heated with a RH instead of a CO_2 laser. The reasons to prefer a CO_2 projector are:

- most of the apparatus lives outside vacuum and can be easily upgraded as new understanding of the ITF is realized;
- from previous studies [94] on CO_2 scanning laser system it seems that a laser could compensate non-axysimmetric thermal lensing. This is an option worth to be kept open for the future implementation of AdV.

Two possible solutions to introduce the CP in the recycling cavity are under investigation: fixing it on the back of the RM or independently suspending it from the SA. The first option seems to be simpler from the point of view of local controls. Since the clear aperture due to the coil-magnet actuators on the back of the RM is 280 mm, this is compliant with the diameter of the CP. The internal thermal noise of the CP must satisfy the AdV requirements. For an unconstrained CP, it is estimated to be more than an order of magnitude below the noise exiting the arm cavity [100]. Clamping to the RM must be carefully studied in order to keep CP thermal noise below AdV requirements and to avoid any unwanted excess of birifrangence.

9.5 TCS sensors

Each optic with a significant thermal load will be independently monitored. The HR face of each test mass will be monitored in reflection for deformation. The input test mass/compensation plate phase profile will be monitored on reflection (either on-axis or off-axis) from the recycling cavity side. On-axis sensing requires that the probe beam enter the recycling cavity through a pickoff port, such as the wedged AR face of the beamsplitter, while off-axis sensing would require the installation of extra optics in the input towers. Lastly, while no compensation on or near the beamsplitter is proposed, it does contribute about 10% of the thermal aberration in the interferometer, and so necessity of monitoring the beam splitter is being investigated. Knowledge of the phase

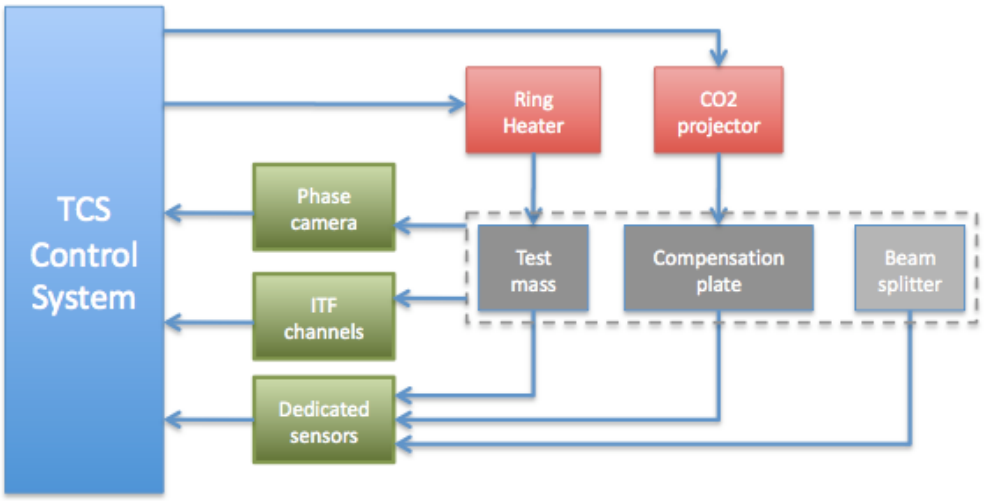

Figure 29: Block diagram of the TCS control system

profile of each optic is valuable, completing the information from the mode profile of the interferometer beam. This will be monitored, using phase cameras, at pickoff ports of the interferometer. The thermal aberrations will be sensed by several complementary techniques. To lowest order, the degree of aberration will be manifest in ITF channels, as it is in Virgo. These are scalar quantities that reflect only the overall conversion of light from the fundamental cavity mode. To sense the spatial structure of the cavity mode, phase cameras will sample the interferometer beam. However, the use of spatial sensors to actively control thermal aberrations has not yet been demonstrated, and the coupled cavity nature of the IFO will make extracting the aberrations of individual mirrors very problematic. Therefore, wavefront sensors will probe the input test masses and beamsplitter individually. The final TCS control will likely adopt a blend of these sensors as inputs (see fig. 29).

The possibility to dynamically correct thermal aberrations in high optical power cavities has been investigated at the GinGin High Optical Power Test Facility (HOPTF) [102].

The ITM-CP phase profile dedicated sensors consist of a wavefront sensing device, and a probe beam whose wavefront contains the thermal aberration information to be sensed. The wavefront sensor shall probe the central region of the ITM-CP pair to a radius not less than two times the YAG beam waist. An evaluation of the wavefront sensor RMS sagitta sensitivity requirement has been performed [90]. The required sensitivity must be better than 1.35 nm (equivalent to approximately $\lambda/600$ at a measurement wavelength of 800 nm) over a 230 mm aperture and a spatial resolution of less than 10 mm over this aperture.

The group led by Jasper Munch at the University of Adelaide, Australia, has been developing a Hartmann sensor for the Gingin experiment and as a potential wavefront sensor for Advanced LIGO. The University of Adelaide's Hartmann sensor [103] has been demon-

strated to have a shot-to-shot reproducibility of $\lambda/580$ at 635 nm, which can be improved to $\lambda/16000$ with averaging, and with an overall accuracy of $\lambda/6800$. This device has been used for measurement of wavefront distortion at GinGin HOPTF [104]. The results indicate that the Hartmann sensor is both sufficiently sensitive for the measurements of absorption-induced wavefront distortion in advanced GW interferometers and is accurate. The use of the Adelaide Hartmann sensor in AdV is proposed.

The change in the radius of curvature of the test masses will be monitored in reflection, measuring the change of the spot size of the probe beam. It is not possible to probe the HR faces of the test masses on-axis, since that would require pickoffs inside the arm cavities. Since the TM HR surfaces are essentially planes, there is no parallax, and off-axis sensors give unambiguous results.

The design of the layout of the TCS sensing beams will be finalized only after the definition of the core optics parameters and of the available viewports.

10 Detection system

The main task of the detection system is to convert the beams into digital signals. It is composed of telescopes for beam adaptation, the output mode cleaner, photodiodes and their electronics, tools for beam diagnostic (cameras, phase camera, scanning Fabry-Perot) and other smaller items like beam dumps, fast shutters and motorized mounts. Those items are located on optical benches in air or suspended under vacuum.

This section starts by describing the AdV features which will have consequences on the detection system. Then it focuses on components of the detection system which should be modified.

This section focuses on the foreseen changes of the detection system. Unless specified, the current design applies.

10.1 AdV features impacting the detection system

The following subsections describe the changes of the optical layout from Virgo/Virgo+ to Advanced Virgo which will require modifications of the detection system

10.1.1 DC detection

The main motivation for selecting the DC readout scheme is a smaller (about 20%) shot noise with respect to the AC readout. There are also advantages for technical noises:

- There is no demodulation noise which is usually one of the dominant source of noise at high frequency for the AC readout.
- Larger photodiodes can be used for the dark fringe since no demodulation is needed. They simplify the beam alignment and reduce the power density. They also make the detection much more insensitive to environmental noise coupling via beam jitter.
- The problem of reduced spatial overlap between the carrier and the sidebands is also not present with DC readout.

Switching to a DC readout scheme for the arm's differential control has several consequences on the detection system:

- The sidebands should be removed from the dark fringe by means of the Output Mode Cleaner (OMC) so that their contribution to the dark fringe is small enough and they do not increase the shot noise by more than a percent. This requirement is not compatible with the current OMC design which should transmit the sidebands and therefore the OMC must be changed.
- The power noise (from carrier and sidebands) can be a limitation. In Virgo the power is stabilized after the input mode cleaner using a photodiode located under vacuum. However the power noise observed in the interferometer (currently the

B5 photodiode which will be the POBS beam in AdV) is relatively high at low frequencies (below 50 Hz) due to the noise introduced by the control loops It seems therefore necessary that the power stabilization uses as error signal a measurement of the power stored inside the recycling cavity for the low frequency part (below 50-100Hz). The power stabilisation will therefore use the beam transmitted by the IMC (for high frequencies) and the beam reflected by the ITF (SP) or POBS (for low frequencies). This will imply to seismically isolate these photodiodes and to put them under vacuum. These photodiodes should also have a good uniformity.

The power noise of the sidebands is usually dominated by the modulation noise. The OMC should filter the sidebands well enough so that this noise does not contribute. This noise could also be measured by an appropriate photodiode and fed back to the modulator.

- The beam jitter is converted into power noise by the OMC. This coupling defines the specifications for the local control of the suspended bench hosting the OMC.

More details on technical noises in the case of AC or DC readout can be found in [105].

DARM offset: In the DC readout scheme a small offset is added to the dark fringe working point so that the DC channel of the dark fringe is sensitive to the gravitational wave signals. In first approximation the DC power on the dark fringe is given by:

$$P_{\rm car} = \frac{P_0 G}{2}\left[(1-C) + \frac{1}{2}\left(\frac{8\mathcal{F}}{\lambda}L_{\rm off}\right)^2\right] \times \frac{T_{SR}}{4} \tag{19}$$

where P_0 is the input power, G the effective recycling gain, C the contrast, $\mathcal{F}$the finesse, $L_{\rm off}$ the offset. The offset should be tuned so that the contribution of the contrast defect is small enough. The contrast defect is driven by the arm losses asymetry ΔP. Assuming $\Delta P = 20$ ppm an offset as small as $5 \cdot 10^{-12}$ m could be used. This offset also has to be kept well above the locking accuracy (it is of the order of 10^{-13} m in Virgo). The offset should not be too high in order to keep the carrier power noise under control: the power noise increases quadratically with the offset while the optical gain only increases linearly. The baseline value for the DARM offset is 10^{-11} m.

10.1.2 Signal Recycling

One additional longitudinal degree of freedom, the signal recycling cavity length, has to be controlled. This changes the length sensing and control scheme and additional modulation frequencies will be added (see the Interferometer sensing and control section). The modulation frequencies for the control signals are now going up into 50-80 MHz range (see section 11), a factor 10 higher than the current value. This will have an impact on the photodiodes and associated electronic used for the controls.

10.1.3 High power

The input laser power will be increased but this does not translate into a direct increase of the power seen on the output ports of the interferometer thanks to the signal recycling scheme and the tuning of the optical parameters. Assuming the parameters of the table 1 the power expected on the dark fringe beam after the OMC (and therefore the suppression of the side bands and higher order modes), is of the order of 100mW (see table 5 of [106]). Therefore we can still use just a couple of photodiodes for the main dark fringe beam ("AP").

For the other beams, the power depends on the choice of the value of AR coatings (pickoff beams) or of the transmission of the end mirrors. It has been shown [107] that powers of the order of 100 mW is sufficient for the controls. Therefore for all beams a couple of photodiodes will be sufficient.

During the locking procedure or unlock events, the power seen by the photodiodes changes a lot. Several (typically 2 as in Virgo) photodiodes, with different gain setting and optical transmission, will therefore be used on each beam. Remote tuning of the electronic gain will also be implemented. Fast shutters will also have to be developped to protect the photodiodes.

10.1.4 Non Degenerate Recycling Cavities

With the non degenerate recycling cavities (NDRC) the signal recycling mirror will have to be placed "on" the suspended detection bench (see section 5). These are sensitive objects which require a seismic isolation level better than the one needed just for the output mode cleaner (see [108]). This will impact the layout of the suspended detection bench and its seismic isolation. Space will be required, although space will be gained since the NDRC solution provides at the same time part of the beam matching telescope.

A side effect of the use of folded NDRC and the change of the BS wedge is the difficulty of sending the POBS beam on the suspended detection bench. Another optical bench might be needed for this beam.

10.1.5 Back scattering mitigation

Due to the improvement of the sensitivity, additional care should be taken with the issue of the backscattering. A study based on Virgo experience [109] has shown that it is not necessary to place the photodiodes under vacuum providing the mechanical structures of the optical benches are improved and the environmental noise is reduced (by typically a factor 2). Good optics quality will have to be used, especially for the telescopes.

10.1.6 Long term maintenance

By extending the life of Virgo, AdV requires a continuous effort to maintain the various components (hardware and software) up-to-date with enough spare parts. Experience has also indicated that more flexibility is appreciated and triggers redesigns. This is especially true for the photo-detectors and the associated electronic, as well as the software.

10.2 Photodiodes for longitudinal and angular controls

The electronic of the photodiodes (preamplifier, demodulation boards and local oscilators distribution) will have to be redesigned in order to work with the new modulation frequencies and to provide all the needed demodulated signals (see section 11). The signal from a single photodiode will have to be demodulated at several frequencies. The preamplifier will therefore provide several outputs corresponding to those frequencies.

Modulation frequencies up to 50-80 MHz will be used. The bandwidth of the photodiodes should therefore be in this range. The theoritical bandwidth of the longitudinal photodiodes is around 80 MHz. Therefore the present photodiodes could in principle be used but their bandwidth remains to be measured. It has to be mentioned that since the number of these photodiodes is limited and since they are no more produced it is foreseen to search for new photodiodes as part of the long term maintenance. A compromise will have to be found between the diameter, the quantum efficiency and the bandwidth. For the AP beam, only the DC component is measured and photodiodes with a larger surface will be searched. The present quadrant photodiodes could also be used if their bandwidth can be increased (it is about 50 MHz now and is limited by the frontend electronics).

In order to avoid the pollution of control signals by environmental noises all photodiodes used for the longitudinal controls in the steady state will be placed under vacuum: AP, SP and POBS beams. The quadrant photodiodes used for the angular controls might as well need to be placed under vacuum for the same reason.

As part of the Virgo+ effort to mitigate the seismic and acoustic noises, work is ongoing to put under vacuum the photodiodes reading the Virgo dark fringe beam (”B1” or AP in AdV labbelling) and recycling cavity beam (”B5” or POBS). Given the limited time/resources available for the Virgo+ preparation, the selected solution (see figure 30) was to build airtight tanks to host all the non vacuum compatible elements: the photodiodes themselves, their pre-amplifiers, the stepper motors used to fine position them, the shutters to protect them and the associated beam dump used during lock acquisition. Such big boxes are nevertheless not very flexible and use space on the suspended bench. Therefore the development of vacuum compatible components (photodiode, preamplifiers, beam dumps, shutters) is needed for AdV. The use of airtight tanks will be the backup solution.

10.3 The Output Mode Cleaner for DC readout

Virgo is currently using an OMC which is a triangular monolithic cavity of 2.5 cm with a finesse of 50 which filters the high order geometrical modes but transmits the sidebands. As discussed previously, a new output mode cleaner has to be designed to get rid of the sidebands in the DC modulation scheme adopted for AdV.

The parameters to be defined are: the finesse, the length, the waist, the geometry and the type of cavity (either a monolithic OMC as used in Virgo or an OMC consisting of individual mirrors rigidly connected by a spacer).

The main issues in the OMC design is first the finesse should be set so that the losses inside the cavity remain small enough. Then, the output mode cleaner has to filter not only the carrier higher order modes but also the sidebands from the modulation frequencies and their higher order modes in order to keep a low shot noise. The filtering should also be good enough to ensure a negligible contribution for the sidebands modulation noise. The light back-scattered by the cavity should be low enough in order to avoid to add any phase noise to the sensitivity. A four mirrors ring cavity will be used in order to be compliant with Higher Order Laguerre Modes. The use of a monolithic cavity will be decided on the basis of the needed length but also on the induced additional losses and thermal effects.

The Virgo note [110] discusses the OMC design and presents different solutions. The baseline approach is to select the OMC geometry by taking a geometrical length of 5.2 cm and then to adjust its finesse according to the final choice of AdV optical parameters and modulation frequencies. The table 12 presents valid OMC solutions for various AdV options. With these solutions, the sidebands contribute to less than 1% of the shot noise and the losses in the OMC are expected to be less than 1%. With this design the modulation noise of SB2 should be below $2 \times 10^{-7}/\sqrt{Hz}$ in amplitude. If this cannot be acheived either the filtering of the OMC should be increased (the finesse and/or length should then be increased) or a feedback loop could be used to cancel the modulator noise. With a length smaller than 10 cm a monolithic cavity can in principle be used. An R&D program is ongoing to test a monolithic mode cleaner with the Virgo geometry but with a higher finesse. The result of this study will help us in deciding wether a monolithic cavity can be used.

10.4 Telescopes for beam size reduction

At each output port telescopes will be installed in order to reduce the size of the beam down to less than a milimeter. They should therefore provide a reduction factor of about 50 for the pickoff beams and for the beams transmitted by the end mirrors. The aberrations and the back scattered light introduced by these telescopes should be small enough. In Virgo, big lenses (doublet) are used for the end benches. These might be replaced by parabolic mirrors if this can lead to a reduction of the back scattered light.

For the dark fringe part of the reduction will be provided inside the signal recycling cavity,

	F_{OMC}	l_{opt} (cm)	l (cm)	ρ (cm)	w_0 (μm)	f_{sc}	$\theta_{i,max}$ (deg)
AdV baseline	100	15.1	5.2	120	240	0.6×10^{-6}	12
$f_2 = 50$ MHz	130	15.1	5.2	240	280	1.5×10^{-6}	11
m=0.2	200	15.1	5.2	120	240	2×10^{-6}	13

Table 12: Characteristics of a monolithic cavity. F_{OMC} is the OMC finesse, l_{opt} the optical length, l the geomtrical length, ρ the radius of curvature of the curvate surfaces, w_0 the waist, f_{sc} the fraction of light back-scattered by the OMC, $\theta_{i,max}$the angle of incidence on the mirrors. The first line is for the AdV baseline parameters ($f2 = 66$ MHz, m=0.1), the second one corresponds to a reduced modulation frequency of about 50 MHz, the last one for a modulation index of 0.2 instead of 0.1.

therefore the reduction factor will be smaller. The aberrations should be such that the losses on the TEM00 remain below 1%.

10.5 Detection benches layout

The layout of the detection benches will have to be updated to accommodate the changes required for the AdV optical design and new benches will have to de installed for the pickoff beams.

10.5.1 Suspended detection bench

The most critical bench is the suspended detection bench which is under vacuum and has the prime task of providing the right environment for the output mode cleaner. The figure 30 presents the layout of this bench in the Virgo+ configuration once the photodiodes will be installed under vacuum. This layout has to be changed to accommodate at least:

- The signal recycling mirror. This mirror will have to be suspended, either from a structure attached on the suspended bench or from the marionetta located above the bench. The design of this local suspension will be carried out by the PAY subsystem and validated by the detection system. In addition the required increase of seismic isolation could be given by one or more filter stages (see the superattenuators section). The required control elements will add complexity on the detection bench.
- The larger OMC. Even if its length remains small (below 10 cm), its oven used to control will require a little more space than the current 2.5 cm long OMC.
- The photodiodes for longitudinal and angular controls with associated telescopes. At least the dark fringe photodiodes will be installed on the suspended bench (2 photodiodes and 2 quadrants). Since photodiodes are equipped with motors and come along with shutters, beam dumps and small telescopes, additionnal space will be needed for those items. Even more space will be needed if air tanks have to be

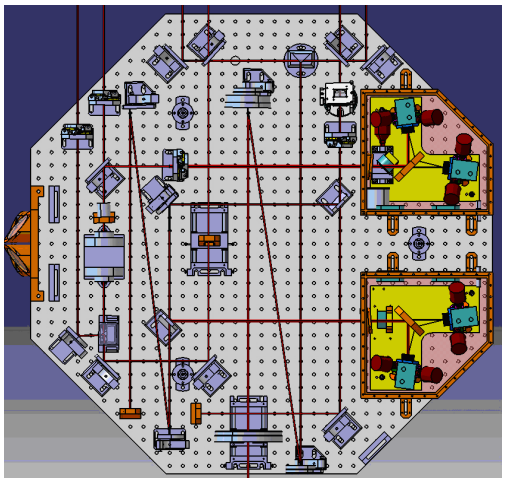

Figure 30: Layout of the Virgo+ suspended detection bench with the photodiode (right part). The OMC is in the lower left part of the bench. The central part is used for the input telescope.

used. The extraction scheme of POBS is not design yet but if it is sent to the same bench 4 more photodiodes will have to fit on this bench.

- As part of the Virgo commissioning activities, baffles and beam dumps have been added to dump the secondary beams produced by the optical elements. Some baffles are directly put on the detection bench and other are just attached around the bench to the vacuum chamber. The upgrade for AdV is the opportunity to have a better design which integrates them onto the suspended bench to benefit of the seismic isolation. Vacuum compatible beam dumps will also have to be developed.

All this will have to be accommodated on the detection bench. It is too early to make any drawing but it is very likely that additional space like the bottom part of the bench will have to be used. Nevertheless, this is a problem which could be solved once the elements to install on the suspended detection bench will be better known.

This reorganization is a good opportunity to apply to the suspended detection bench some of the improvements foreseen for the clean air distribution in the large mirror vacuum chambers.

10.5.2 External detection bench and other benches

The external detection bench will have to be reshuffled to accommodate the new layout of the suspended bench. The mechanical structure will have to be reinforced to avoid resonances at low frequency (now around 20 Hz) and to reduce the noise from the air conditioning system. This is also the right time to revisit the cleanliness of the bench.

Similar work has to be made for the end benches.

Since new pick-off beams from the input mirror or beam splitter will be available, they will require small additional optical benches to host the required telescopes, photodiodes, cameras or other devices. Their mechanical structure will also have to be carefully designed to avoid resonances at low frequency.

11 Interferometer sensing and control

11.1 Sub-system scope

The Interferometer Sensing and Control (ISC) system of AdV defines the required techniques to acquire and maintain the resonant conditions of the light fields in the cavities inside the interferometer, and defines a technique to acquire and maintain the alignment of the eighteen angular degrees of freedom. In the mode where the interferometer is acquiring science data, the noise of the control loops is required to be negligible.

With respect to the initial Virgo interferometer, the signal recycling cavity adds new complexity. A detuning of the km arm cavities realizes the "DC readout". The subsequent optical spring has large impacts on the control strategy of the interferometer, detailed further in this chapter. Some fraction of the 760 kW in the arm cavities, scattered on high order TEMmn modes, will excite the mirror resonances. The ISC will have to predict and mitigate these parametric instabilities.

11.2 Introduction

11.2.1 Operating point

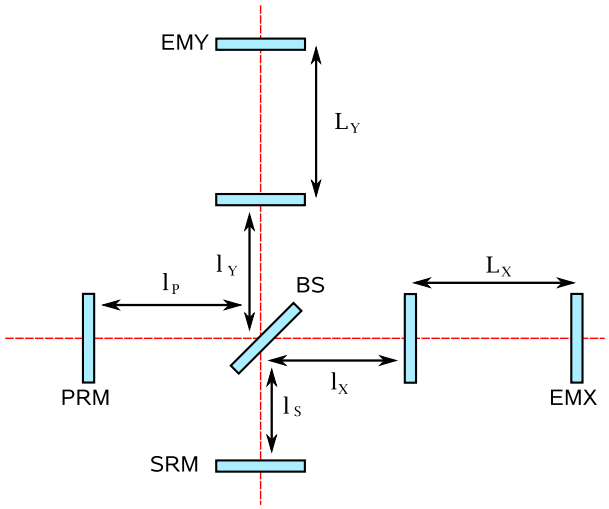

Figure 31: Definition of lengths in AdV. All lengths are considered between high-reflection coated surfaces, taking also into account the mirror substrates. For the non degenerate recycling cavities, the lengths sum up the distance with folding mirrors.

Referring to fig. 31, the microscopic motion of all lengths around the operating point are combined to form the following physical degrees of freedom:

$$DARM = L_X - L_Y$$

$$
\begin{aligned}
CARM &= \frac{L_X + L_Y}{2} \\
PRCL &= l_P + \frac{l_x + l_y}{2} \\
MICH &= l_x - l_y \\
SREC &= l_S + \frac{l_x + l_y}{2}
\end{aligned}
$$

The operating point in the linear state is defined as follows. CARM and PRCL are tuned to the resonant position and MICH to the minimum of power transmission to the dark fringe. DARM is slightly detuned from resonance for DC read-out [111]. SREC is also detuned by a static amount which is used to profit from the signal recycling shaping of the detector response [112]. This *signal recycling tuning* is of the order or 0.1 rad.

11.2.2 Optical spring

The detuning of the arm cavities adds an effective optical spring four order of magnitude larger than the longitudinal mirror suspension response [113]. This improves the locking accuracy by 4 order of magnitudes, at no cost. On the challenging side, we have to overcome the unstability when the actuation transfer function flips its sign while increasing the laser power. A rotational optical spring will also affect the angular degrees of freedom, and will also flip the response sign. We plan to compensate both angular and longitudinal optical springs with "digital springs": digital filters with same frequency response and opposite sign will hide the sign flipping of the actuation TF when the power increases.

Due to the optical spring, the dark fringe will be more sensitive to the shot noise limited resolution of the longitudinal auxiliary degrees of freedom will be re-introduced in the dark fringe; we plan to feed-forward this noise.

11.3 Longitudinal lock acquisition

The lock acquisition strategy deals with the actions needed to bring the interferometer from a un-controlled condition to the final science mode configuration. As a first step the two recycling mirrors are mis-aligned in order to avoid their reflection to interfere with the main beam entering the interferometer, and the arm cavities brought to resonance. Then the other degrees of freedom are brought into operation.

11.3.1 Arm cavity lock with auxiliary laser implementation

Two independent auxiliary lasers will be used to acquire the lock of the kilometric arms. As their wavelengths are different from the main laser, the reflectivities of the mirrors are much smaller (5-15%) and the finesses of the cavities are lower, allowing an easier lock acquisition. Once the arm is under control, it is brought in a deterministic way to

its working point where the error signals from the main laser can be used: an offset in the auxiliary laser error signals is introduced and a smooth transition is performed. The principle of this lock acquisition has been successfully tested in simulation on a single cavity.

The main constraint on auxiliary lasers will arise from frequency stability. The cavity width is c/2FL 50 Hz. Supposing that the transition between auxiliary laser and main laser is performed in 100 ms and assuming a safety factor of 10, this means that the RMS integrated down to 10 Hz has to be about 5 Hz. This requirement is reached installing a reference cavity for each auxiliary laser. Even if a special care has to be taken, such performances have been obtained by several groups and should not be critical.

The auxiliary laser locking technique allows an implementation with a minimal impact on other subsystems as only end tower optical benches will be impacted. On each bench, we need to install an auxiliary laser with its electro-optic, Faraday isolator and a rigid cavity for laser frequency stabilization. The auxiliary beam has to be superposed to the outcoming main beam and then injected in the arm cavity. The design of the telescope has to take care of the presence of this auxiliary beam but should not be critical since the input power is not a problematic issue. The reflected auxiliary beam will be used for the control of the cavity.

The installation on site will be performed by the LAL group with the support of ESPCI people who are deeply involved in CALVA.

While some simulations have been successfully performed for CALVA cavities, similar simulations will be done for AdV arms. Moreover, we will investigate the possibility to keep the arms locked on auxiliary lasers even when the central degrees of freedom are aligned. In case of success, it can allow to simplify the whole acquisition procedure.

11.3.2 Full interferometer lock acquisition

The strategy foreseen for AdV is an extension of the Variable Finesse technique successfully implemented in Virgo [114]. After the two cavities are on resonance, if the signal recycling mirror is maintained mis-aligned, the system behaves as a power-recycled interferometer and it can be locked up to the dark fringe condition with a Virgo-like technique [115]. After reaching the dark fringe configuration, the signal recycling mirror can be re-aligned and its control system activated.

The key point of this strategy is the choice of suitable modulation frequencies in order to decouple as much as possible the various degrees of freedom [112, 116]. When the interferometer is in its operating point, the carrier must be resonant in the power recycling cavity as well as in the arm cavities. It must also be anti-resonant (in the Resonant Sideband Extraction regime) in the signal recycling cavity. In this condition, a first modulation frequency f_1 is chosen in order to have the corresponding pair of sidebands SB1 resonant in the power recycling cavity and close to anti-resonance in the arms. Moreover, the Schnupp asymmetry must be tuned in order to have a small transmission

of SB1 to the anti-symmetric port. In this way the amplitude of carrier and SB1 inside the signal recycling cavity is small and the re-alignment of the signal recycling mirror has a small effect on these fields. If all the power-recycled-interferometric degrees of freedom are controlled using signals coming from the beating of carrier and SB1, it would be possible to maintain their control even during the re-alignment of the signal recycling mirror [112, 116]. A second pair of sidebands SB2 must be used to extract a suitable control signal for the signal recycling cavity length.

To avoid troubles from radiation pressure effect, the lock acquisition sequence must be carried out at reduced input power and the final level should be reached only when the interferometer is already stably controlled in its final configuration.

11.4 Linear locking scheme

11.4.1 Specifications

The length sensing and control design starts with the simulation of the optical response of the system. The large circulating power inside AdV induces large radiation pressure effects, which significantly alters the shape of the opto-mechanical response of the system. Optickle, developed by our LIGO colleagues, is a transfer function simulation tool capable of dealing with radiation pressure effects.

Once the interferometer has been brought to the final working point, the longitudinal control system must be tuned in order to reach low noise operations. The design of the science mode control strategy deals with the simulation of the entire system and the selection of the error signals that can give the best performance in terms of quantum-noise limited operation.

The specifications for the length sensing and control system can be stated in terms of maximum residual RMS fluctuation of all degrees of freedom around the operating point and in terms of sensing noise re-injected inside the observational bandwidth. The latter translates in the requirement that the quantum-noise-limited operations of the LSC system must not limit the detector sensitivity (at the design level) at any frequency.

The RMS fluctuations are instead clearly dominated by the very low frequency residual motions. Specifications can be set up considering the resonance width of the cavities and possible estimates of noise up-conversion [108]:

$$\begin{aligned} RMS_{DARM} &< 2 \cdot 10^{-14} \text{ m} \\ RMS_{CARM} &< 1.3 \cdot 10^{-14} \text{ m (1.3 mHz)} \\ RMS_{MICH} &< 1.1 \cdot 10^{-11} \text{ m} \\ RMS_{PRCL} &< 9 \cdot 10^{-11} \text{ m} \\ RMS_{SREC} &< 2 \cdot 10^{-10} \text{ m} \end{aligned}$$

11.4.2 Sensing and control design

The length sensing and control system for Advance Virgo is based on the use of three modulation frequencies, which corresponds to three pairs of sidebands with different resonance conditions at the operating point:

SB1 are resonant in the power recycling cavity and very close to anti-resonant in the arm cavities. A detuning is assumed from the cavity anti-resonance to avoid the second harmonics to be resonant. The Schnupp asymmetry is chosen to be small enough to make the transmission of these sidebands to the east port (toward the signal recycling cavity) of the beam splitter very small. SB1 are in any case close to be anti-resonant in the SRC.

SB2 are resonant in the PRC and simultaneously in the SRC. The Schnupp asymmetry is optimized to have an optimal coupling of these sidebands inside the signal recycling cavity. In other words, it is chosen to maximize SB2 power inside the SRC.

SB3 are not resonant in the PRC and close to the arm anti-resonance. In this way this pair of sidebands are almost completely reflected by the interferometer. Although the use of such sidebands is not strictly necessary for the longitudinal control, the Virgo commissioning profited a lot from their use.

In addition, all these sidebands must be transmitted through the input mode cleaner.

All these requirements can be translated in one set of lengths and modulation frequencies [117, 118, 106] for the *non-degenerate recycling cavities* (NDRC) situation. This set will be fully determined when the choice of NDRC will be completed; simulations have shown that whichever option is chosen for NDRC we can have SB1 and SB3 at 'low' frequency (6-10MHz) and SB2 in the range 50-80MHz.

As an example, a full simulation has been developed using Optickle, for one configuration of the NDRC. Details can be found in [118]. The outcome is the full optical matrix, i.e. the set of transfer functions from any degree of freedom to any demodulated signal. The baseline design consists of a "double demodulation scheme" (sensing of recycling cavities with the beating note among sidebands" rather than A "single demodulation scheme" (sensing with the beating of sidebands with carrier). This scheme gives higher shot noise levels, but better decoupling of the degrees of freedom.

The Optickle simulation computes the level of quantum noise for each output signal. This can be used together with the optical matrix to select suitable error signals to control each degree of freedom and to simulate the effect of the control loops. The list of error signals used for each degree of freedom is given in tab. 13.

The accuracy of each loop has been computed using as a reference the real motion of suspended test masses of Virgo [118]. The results are compatible with the requirement computed above.

The quantum noise of each error signal has been used to compute the noise re-injected in the gravitational channel. The result is shown in [106]. So far control loops have been

D.O.F.	error signal
DARM	ASY_DC
CARM	SYM_SB1_P
PRCL	SYM_3P1_P
MICH	SYM_2M1_Q
SREC	SYM_2M1_P

Table 13: Error signals used in the double demodulation scheme. Names containing 3P1 and 2M1 are given to signals obtained with double demodulation at $f_3 + f_1$ and $f_2 - f_1$. P and Q refers to the two signal quadratures. SYM refers to the symmetrical port (POPR port in figure 11) and ASY to anti-symmetric port (AP port).

designed to be robust and not at all optimized for low noise performance, for example introducing steep roll-off in the control filters.

The LSC system would be the limiting source of noise in a large bandwidth: the control noise is as much as a factor 100 above the target design sensitivity. This is similar to what happened in Virgo and the solution is the implementation of noise subtraction paths [119]. To bring control noise below the design sensitivity it would be necessary to obtain roughly a factor 100 of noise suppression, which seems easily feasible given the factor 1000 obtained in Virgo. The side-effect of the use of noise subtraction path is the amplification of seismic noise coming from the auxiliary degrees of freedom [108].

11.4.3 Status of LSC design

The foreseen lengths and modulations has a significant impact on the vacuum system, since the Schnupp asymmetry is reduced from 80 to 4 cm. The displacement of some towers would be needed.

The double demodulation scheme gives radiation-pressure-independent signals for MICH, PRCL and SREC, at the price of a larger level of control noise. This is not worrying, since it can be fixed using noise subtraction paths, which are in any case needed in both schemes.

11.5 Alignment

The goal of the alignment is to superpose the axes of the resonant modes of the cavities with the beams. The main differences with respect to the initial Virgo situation are given essentially by the presence of the Signal recycling mirror, the high circulating power and associated angular optical springs and the NDRC optical scheme.

The whole alignment control is based on the wavefront sensing scheme with a modulation-demodulation technique. The control scheme will be based on a Ward-like technique, using pick-off beams in reflection of the cavities for the cavities pre-alignment.

The additional complexity of the signal recycling cavity is recovered with:

- the use of the same set of modulation frequencies as for the longitudinal locking, which decouple SRC and PRC cavities;
- a further decoupling of the two recycling cavities by having different Gouy phases

The presence of angular optical springs is mitigated with the use of digital springs. The additional mirrors in the NDRC are kept under local control in addition to a global drift control which will use the experimented techniques used for the initial Virgo.

Some investigations have been already done or started:

- the influence of the Etalon effect of a curved/curved terminal mirror on the automatic alignment error signals [120]
- consequences of the presence of compensation plates for the thermal compensation on the alignment error signals
- preliminary control scheme for the cavity alignment [121]

11.6 Parametric instabilities

The parametric instability (PI), which consists in the coherent ringing of a mechanical mode of a cavity mirror by the circulating optical power[122], may significantly affect the performance of high-power signal-recycling gravitational-wave interferometers[123]. A great number of vibration of the mirror substrates are indeed likely to reach a very important vibration amplitude and therefore prevent any stable operation of the interferometer, eventhough most mechanical modes are outside the detection window.

Up to now, the PI has already been demonstrated in systems such as micro-toroids [124] or silicon micromirrors [125] in which a single optical mode interacts with a single mechanical mode, with a mechanical frequency much smaller than the cavity bandwidth. The instability of interest for gravitational-wave interferometers is slightly different, as it involves a 3-mode coupling between the main optical mode, a mechanical mode and a second optical mode, the frequency mismatch between the two optical modes matching or almost matching the mechanical resonance frequency. The Advanced large-scale interferometers, with their very high mechanical mode density at frequencies such as tens of kHz, unfortunately are very good candidates to display such an instability.

Such a 3-mode coupling has already been observed in the australian high-power laser facility [126]. Different experiments (Paris, Perth) are underway to demonstrate the instability in such a configuration, using almost degenerate optical cavities and micro-optomechanical systems such as silicon micromirrors or optical membranes.

Detailed simulations of the impact of the PI have already been performed by the Perth group and show that in the current Adv Ligo optical configuration, the number of unstable mechanical modes is unlikely to be below 5 for any set of optical parameters (mostly the

radius of curvature of the mirrors, the resonance condition being extremely sensitive to the Gouy phase).

The PI has up to now been mainly considered through its impact on the interferometer working point, but it also very likely to have a huge impact over the lock acquisition as well, with transient optical modes reaching the instability threshold for a brief time. A good understanding of the PI both in the steady state and in the lock acquisition process is therefore necessary in order to devise a proper PI-killing scheme.

The tasks to be completed for the AdV design include:

- development of a realistic and yet tractable model of the whole interferometer, taking into account the compound nature of the interferometer, signal as well as power recycling..., and possibly some control loops
- evaluation of the number of unstable modes for any given optical configuration, with a possible feedback onto the optical design
- evaluation of the impact of the PI over the lock acquisition process

In parallel, an experimental demonstration of the PI in a 3-mode configuration will be pursued in a table-top experiment (LKB, Paris). The currently underway experiment could be used as a test-bed for future tests of possible PI-cancellation schemes.

Once the first investigations are over, in the case where the stable operation of the interferometer is considered to be jeopardized by the PI, we will have to investigate how to circumvent the PI.

Possible solutions include:

- the use of lower Q mirrors (which increases the PI threshold and may dramatically decrease the number of unstable modes)
- thermal tuning of the cavities (to a favorable working point)
- monitoring and control of the instability, by either mechanical or optical feedback. The implementation of feedback will either take advantage of existing actuation techniques or require some additional equipment close to the substrates.

The design solution will have to be robust against small changes in the interferometer specifications, as discrepancies have to be expected between the design configuration and the measured values of the mirror characteristics.

Advanced Virgo Baseline Design:

PART 3:

Test mass vibration isolation, suspension and control

12 Superattenuators

12.1 Vibration Isolation and Test Mass Suspension

The isolation performance of the Virgo suspensions is expected to be compliant with the requirements of AdV. Therefore, no major changes to the vibration isolation system are required, and the general design with the Superattenuator (SA) chain will be maintained (see fig. 32). However, the experience of the Virgo commissioning has shown that some aspects of the design can be improved.

The inverted pendulum preisolator (IP) is controlled in 4 d.o.f. only (the three translations and the rotation around the vertical axis). It has been understood that the ground tilt, especially in windy days, can spoil the performance of the inertial damping and cause excess low frequency noise to be transmitted to the mirror. Therefore, the SA design has to be modified to allow tilt control.

12.2 IP Modifications and Tilt Control

The present Virgo pre-isolation stage, the IP, must be upgraded to be controllable in all six d.o.f., using tiltmeters as sensors for the rotational d.o.f. (see sec. 12.3). Since the beginning the mechanical structure of the IP was designed taking into account the possibility to implement a tilt control: an elastic element was embedded within its feet (see fig. 33) and the space for inserting PZT actuators was foreseen. Each IP leg can be thus acted upon in the vertical direction to compensate the tilt effect measured on the IP top stage. In this way, the IP top stage could become an inertial platform controlled in 6 d.o.f.. Moreover, a complete revision of the leg structure, changing it in a monolithic one with an increased sectional area (higher momentum of inertia) will move to higher frequency the annoying leg resonance now at about 10 Hz.

Also the low resonance mode of the Filter Zero (F0) crossbar falls in the same region. Such structures in the IP transfer function reduce the attenuation performance and make difficult to widen the control bandwidth of the inertial damping. Therefore, it would be helpful to revise the F0 design making the crossbar more rigid. The F0 mechanical system is beeing investigated to explore and optimize the various options of intervention on its crossbar centering wires, and on the position of the two vertical accelerometers accommodated over the same crossbar.

12.2.1 New IP Prototype Status

Starting from the present design, and reducing the impact of the changes at the minimum level, a new mechanical structure for a monolithic IP prototype with stiffer monolithic legs and increased sectional area has been designed and built. This prototype is beeing installed and tested in the SA facility at EGO (SAFE) [127]. This facility will host a complete SA chain operating also the tilt control and the other foreseen upgrades.

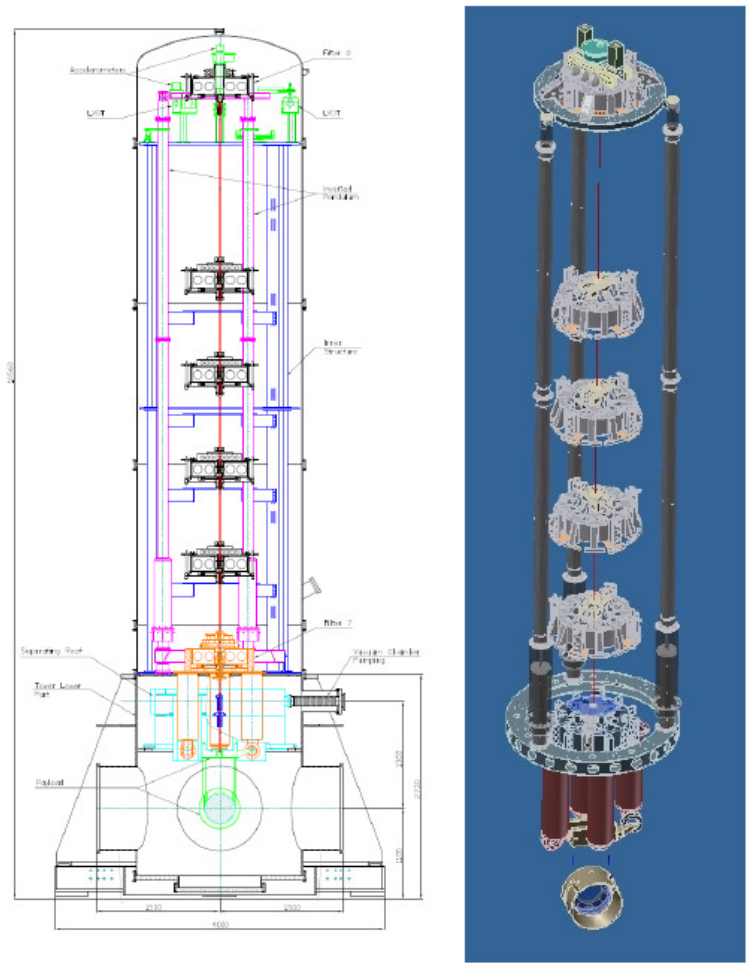

Figure 32: Drawing and rendering of the entire Virgo Superattenuator.

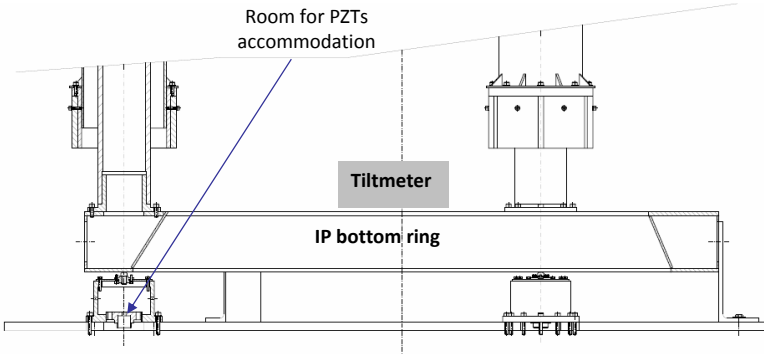

Figure 33: The IP bottom part is visible. A section of a foot supporting the IP bottom ring and the last part of IP leg is visible on left side. A schematic box representing the tilt meter accommodation is also shown.

12.3 Tiltmeters

The operation of Virgo has shown that the inertial damping performance is partly spoiled by strong wind. This has been explained as an effect of wind-induced ground tilt. The signal of the in-loop horizontal accelerometers is coupled to the tilt of the SA top stage around the horizontal axes, and this turns into low frequency noise transmitted to the mirrors. This makes the VIRGO lock acquisition more difficult with bad weather conditions and the effect will become even more relevant in AdV. An active control of tilt should then be implemented to make the detector more robust.

A direct way to deal with the tilt compensation is operating a feedback control with tiltmeter sensors, requiring a sensitivity of about 10^{-8} rad/$\sqrt{\text{Hz}}$ at 30 mHz [128]. The activity in progress is focused on the study and the development of tiltmeter based on a device conceived around a pivoted bar with LVDT sensors (linear variable differential transformer) placed at its ends (see fig. 34).

This sensor is effectively a force balanced angular accelerometer, consisting of a pivoted balance having its CM as near as possible to the rotation axis. This configuration is intended to make the tilt sensing less affected by the longitudinal acceleration, decoupling tilt rotations from the longitudinal motion. The sensor output is DC coupled for not spoiling its low frequency response. Being a force balanced angular accelerometer the balance arm is kept at a fixed position, with respect to the surrounding frame, by a feedback control system sensing a system of two LVDTs and driving a couple of coil-magnet actuators [129, 130]. The feedback signal itself is proportional to the angular acceleration, thus the tilt signal is extracted after a double integration process.

Two of these sensors, aligned along the main axis of the interferometer, will be installed within the vacuum vessel of each SA on top of the IP platform ring (see fig. 33).

12.3.1 TItmeter Prototype Status

Two identical prototypes have been build and assembled.

Two kind of cantilevered flex-pivot bearings have been installed on the rotation axes of the force balance system. This type of cantilevered flexural bearings has been chosen because are compact, relatively easy to be installed, frictionless, do not require lubrication and its mechanical properties are predictable and measurable. Similar joints have been already adopted satisfactorily in less demanding mechanisms to adjust the working position of the Virgo anti-seismic filters. The single-ended type was the first to be implemented, and it was later substituted with the double-ended one, trying to optimize the load stress distribution on the blades.

The experience made while operating the tiltmeter prototypes has shown that a very accurate mounting of these flex-pivots is required to avoid spoiling the low frequency performance. These joints have shown setup difficulties with low reliability and reproducibility.

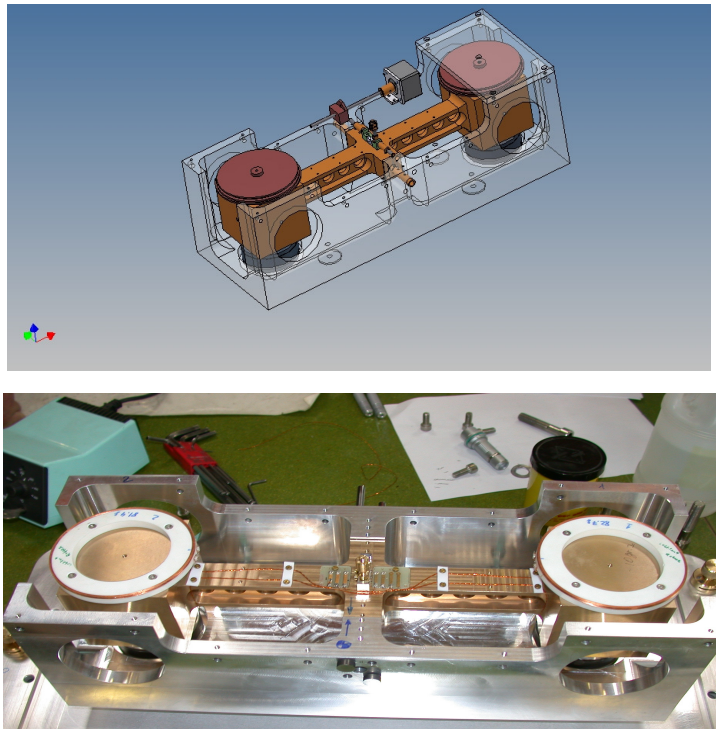

Figure 34: Rendering and image of one tiltmeter prototype.

The present activity is oriented towards the construction of some new flex-pivot prototypes implementing couples of very thin cross-wires under tension. This geometry looks simpler and more reliable than the cross-blades flex-pivot in use until now, and has the advantage to be quickly implantable in the current prototype. New tests will follow in the next months

12.4 New SR Construction and Upgrade of the Short Virgo SAs

The AdV optical baseline foresees the installation of a new SR suspension and the requirements about the residual seismic noise displacement, at the level of the suspended optics in the non degenerate cavities, will demand for an upgrade of the Virgo short SAs attenuation performances. SAT planning documents concerning the WBS, the time schedule, the allocation of manpower resources, and the risk management for carring on all the necessary activities have been delivered [131, 132].

12.4.1 SR Superattenuator

A complete long SA must be assembled to suspend the SR mirror to fulfill the requirement of a residual mirror displacement noise down to a level of about $6 \cdot 10^{-18}$ m/$\sqrt{\text{Hz}}$ at 10 Hz [133]. This suspension will essentially replicate the mechanics of the existing long

Virgo SAs and will be provided with all the upgraded parts (new IP legs, tilt control, new payload).

12.4.2 Short SA Upgrade

The adoption of non-degenerate recycling cavities in AdV will require the installation of some optics of the PR and SR cavities on the IB and DB benches. This upgrade will set new specifications for the anti-seismic attenuation of the IB, DB and IMC end mirror short SAs, up to requiring additional filter stages. These attenuation specifications are being investigated with optical simulations, evaluating the level of residual displacement noise in the AdV control signals.

AdV requirements foresee to add one more filter stage on the IMC tower, maintaining the same SA height. The need of more than one extra filter stage is foreseen for the IB and DB chains where the vertical seismic attenuation must be increased at least by a factor 10^5 [134].

Adding four more filter stages will necessarily change the heights of the IB and DB towers reaching that of the long Virgo SAs. The interventions will concern not only the upgrade of the first SA stage (F0) and of the IP flexible joints, but also the substitution of the whole IP, the upgrade of the safety structure and the complete cabling reshuffling.

Tilt control will also be implemented on all of these towers, while the IP legs of the IMC, being already monolithic, will not be changed.

12.5 Suspension Control Upgrade

A detailed planning document concerning the Suspension Control System upgrade for AdV has been delivered [135]. The main activity concerning the suspension electronics is the upgrade of the conditioning electronics used to manage the sensor and the actuators placed in the suspension stage, namely the accelerometers, the LVDTs, the stepping motors, the local control sensors and the coil working at different levels of the chain. Other components that will be likely implemented for the tilt control, like tilt-meters and PZT actuators, have been already introduced (section 12.2). Moreover, considering the AdV optical scheme a new complete suspension electronics, including the sensors and the actuators, have to be implemented for the control of the SR chain (section 12.4.1).

12.5.1 CRATES

Standard NIM used in Virgo will be abandoned since it is no longer available. VME Crate will be abandoned since no longer necessary for communication with other Virgo sub-systems.

At present we have 2 NIM crate + 1 VME crate for a total of 3 crates to be replaced for each suspension.

12.5.2 LVDT Electronics

The LVDT sensors actually used in Virgo to measure the position of the SA top stage and the relative position of the anti-seismic filters along the chain do not require any particular improvement. In fact, they are enough sensitive to be compliant with the AdV requirements. On the other hand the conditioning electronics of these sensors need to be upgraded.

A significant improvement in terms of performances is expected by using more recent and specific components. It is also foreseen to implement a digital output on the driver by using an onboard ADC to immediately digitize the position signal, and sending it to the processing and control electronics through a digital link. This solution has the clear advantage to greatly reduce the possible interferences and electrical pick-ups from the electromagnetic noise present in the environment. Finally it is foreseen to use such new drivers also to manage the LVDT sensors used inside the accelerometers of the top stage; this solution will avoid the development of hybrid electronic board and will make more logical and easy to maintain the full suspension electronics.

Studies of a new design for LVDT electronics are going on since a few years. A candidate ADC converter was selected and tested together with a DAC converter and a PLL circuitry capable of letting the two converters operate at different rates synchronously with VIRGO timing signal. Such studies were partially integrated in the activity for the upgrade of Virgo control electronics together with new DSP design [136]. Digital data link was studied taking advantage from a fellowship. The final report is available [137].

12.5.3 Accelerometer Design and Electronics

The upgrade of the accelerometers (sensors are force-balance accelerometers) used to perform the inertial damping of the top stage involves mainly the internal driver.

The upgrade foreseen for the driving electronics, apart from the use of an external LVDT driver, and the introduction of a digital output for the acceleration signal, as already stated in the previous section, is the replacement of a digital feedback instead of the analog one currently used. The implementation of such digital system would allow the design of more effective feedback for the internal loop, resulting in a wider frequency band, in an improved robustness and in improved noise performances. Of course for this aim some suitable additional electronics has to be hosted on the driver, namely an ADC to digitize the position signal coming from the LVDT, a DSP for the digital filtering, and a DAC for the actuation on the internal coil.

Concerning the actuation system inside the accelerometer, a few initial studies were carried on to evaluate the possibility to replace existing voice coil actuator (coil-magnet) with a coil-coil pair.

12.5.4 Coil Driver Electronics

The Coil Driver were upgraded for Virgo+ and their current performances, in terms of noise, linearity and frequency band are already compliant with the AdV requirements [138, 139].

The major upgrade is related to the introduction of a digital input, through a fast optical link connected to an onboard DAC and to a selection of a new DAC converter (the one in use is obsolete). The digital link is particularly important since the actuation signals of the coil are the most critical for the ITF sensitivity, and a connection between the control and processing electronics that is virtually unaffected by environmental interferences is strongly desirable.

12.5.5 Step Motor Driver

A minor changes is related to the control logic that is currently obsolete. A standard commercial solution seems the best choice since there are no special requirement on the performances of the system.

12.5.6 Control Electronics

The major upgrade in the architecture of the Processing and Control Electronics, namely the DSP, the real time CPU, the ADC, the DAC and the digital optical link, was already performed during the Virgo+ upgrade. In particular the new processing board [140], with its 6 DSP, allows a very high computing power with respect to the old Virgo single DSP board. Thanks to these changes it is possible to perform better control strategies and to design more effective digital filters.

Some improvement is still required for the analog/digital converters, ADCs and DACs, in particular about the effective number of bits, in order to reduce the quantization noise introduced during both the sensing and the driving.

DSP

No major change is foreseen on the processing board. Nevertheless a daughter-board has to be developed to manage the digital signals exchanged with the suspension electronics equipped with digital input or output. The architecture should be very similar to the one already implemented for the global control signal in Virgo and in Virgo+, but in this case it refers also to local control signals.

Digital data link was studied taking advantage from a fellowship [137]. A preliminary design of the board is already available.

ADC and DAC

The ADC of the suspension control electronics, in the Virgo and Virgo+ configuration, are located in the same unit of the processing electronics and are used mainly to convert

signals coming from the suspension electronics, located close to the respective tower. In AdV some of these converters will be placed directly in the suspension electronics. Despite of their location, an improvement of their performances, mainly in terms of quantization noise reduction, should be achieved.

As for the case of ADC, also the DAC performances need to be improved. The DAC noise is even more critical, since the current performances are still a limiting factor for the achievement of the Advance Virgo sensitivity in the low frequency region, due to the direct coupling with the coils actuating on the test masses. A specific R&D is dedicated to the selection of a suitable chip, with an higher number of bits with respect to now and higher sampling frequency to decrease the noise content.

A candidate ADC converter was selected and tested together with a DAC converter and a PLL circuitry capable of letting the two converters operate at different rates synchronously with VIRGO timing signal.. Such studies were partially integrated in the R&D activity for the upgrade of Virgo control electronics together with new DSP design.

12.5.7 Superattenuator Control Software

A redesign of the Superattenuator Control Software (SCS) is in progress and the documentation is already available on the web [141].

SCS have to allow maintenance, configuration and operation of the whole set of AdV Suspensions to handle the replacement of DSP currently in use conserving the existing functionalities.

12.5.8 Thermal Stabilization Control

A thermal stabilization system to control the temperature of the suspensions, and thus its length and filter operating points, is ready to be installed since a few years. For a proper operation the variations of the suspension enclosure temperature shall not exceed +/- 0.2 ^{o}C.

This requirement was up to now fulfilled stabilizing the temperature of the whole central hall and terminal buildings. It could be easily met using heating belts wounded around the towers, thus relaxing specifications on air conditioning system, allowing temperature variations into the building up to 2 ^{o}C.

13 Payload for AdV

The payload is the last stage of the mirror suspension, located in the lower part of the tower where there is a separated vacuum chamber connected through a thin conductance pipe to that hosting the superattenuator. The role of the last stage suspension is to compensate the residual seismic noise and to steer the optical components maintaining the relative position of the interferometer mirrors. In the current configuration, it is essentially a double stage branched system with the so called marionette as first pendulum, and as branches, the reaction mass and the mirror both suspended from it with steel wires. The position of the mirror is controlled by two sets of coil-magnet actuators. One set is between the F7 and marionette and the second one is placed between the reaction mass and the mirror.

The AdV payload must be compliant with the new mirrors having larger mass and different thickness, suspended with silica fibers (monolithic pendulum suspension). Moreover the whole payload must be compatible in shape and materials with the enhanced thermal compensation system required in AdV setup that will probably make use of a further suspended element (compensation plate) in the case of the input mirrors of long Fabry-Perot cavities (sec. 9).

A further improvement that could be introduced is to move the coils from the F7 to a separate reaction mass around the marionette. This could greatly simplify the payload installation and it is crucial in case the beam splitter will have a large diameter ($\sim$ 50 cm). The study of this new element is currently in its prototyping phase (fig. 35).

Figure 35: Schematic picture of the new payload in the configuration with the marionette reaction mass is adopted.

Moreover the optical scheme of AdV requires longer central cavities (both power and signal recycling) in order to remove the degeneracy of higher order modes (NDRC). The motivation of NDRCs is mainly related to the feasibility of high power implementation and does not concern the intrinsic noise sources of test masses.

The general approach adopted to merge all the issues mentioned above ad to depict a

redesign baseline for AdV payloads can be divided in two major sections (fig. 36) :

- monolithic suspension implementation;
- multi-mirror payloads.

While the feasibility study of monolithic suspension payloads had been started-up earlier in order to install suitable payloads in the context of Virgo+, the issue of NDRCs and related multi-mirror payloads has been treated later, through a trade-off among the requirements and specifications of several systems (OSD,PAY,ISC,INJ,DET) in order to enlighten its critical parameters.

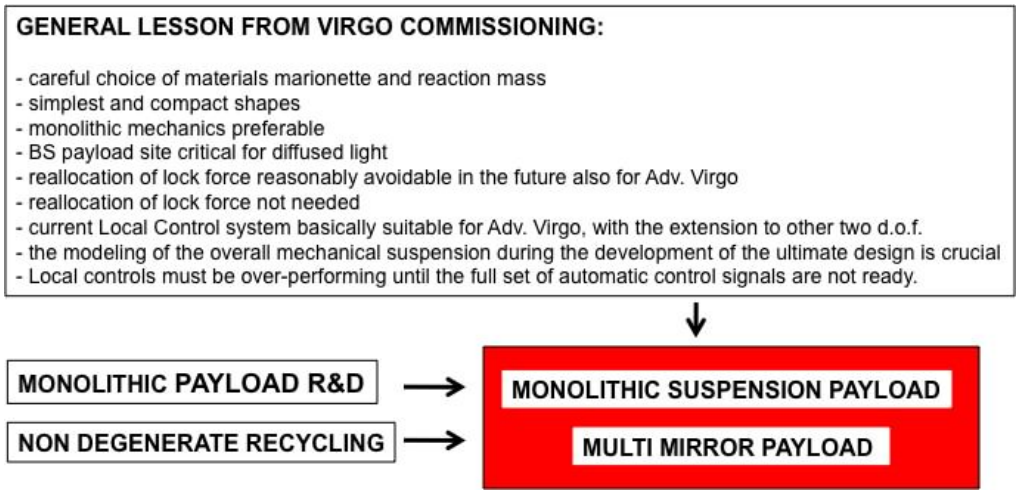

Figure 36: Schematic of the approach for the study of AdV payload

Provided that the positions of suspension vacuum chambers are constrained by the infrastructure of the building and that there is not the room to install further superattenuator towers, a preliminary study focused on two-folded beam schemes for power and signal recycling cavities OSD (5.5) have been performed to be compliant with perspective of PAY by considering the following items:

- exploiting the maximum distance available in the central cavity area in between the injection bench and the input towers;
- exploiting the experience gained in designing payloads with single-point suspension systems;
- limiting off-axis folding angle in order to spoil the central cavities' beams with astigmatism;
- avoiding further complication of payloads with monolithic suspensions of mirrors.

Such a baseline has been adopted to delineate few scenarios. Even though the ultimate design of NDRCs is not frozen we can say that a suitable solution that meets all the zero-order requirements have been selected according to a scheme coded as OSD2 (sketched for power recycling cavity in fig. 14).

That consists in the conservative and reasonable choice of completely redesigning the Beam Splitter payload, suitable for suspending two folding mirrors of NDRCs. Injection and detection benches will be fully re-designed taking into account the need of hosting the suspension for the first and last mirrors of of NDRCs. According to such a scenario the superattenuator towers of power recycling and the signal recycling will be used to suspend second folding mirrors of NDRCs by means of standard payloads that might be similar to those presently used for Virgo. In such a way monolithic suspensions and enhanced TCS elements will be not concerned by NDRCs. Therefore the impact of novel features will be reduced since the basic marionette design, suitable for both monolithic and steel pendulum suspensions, will be kept. Only the design of Beam Splitter payload, multi-mirror and reasonably equipped with specific marionette reaction mass, will be completely revised.

The main features of AdV payloads are resumed in the following table:

mirror	Tower Location	monolithic	TCS plate	Marionette RM
3km-FP input (x2)	Input (x2)	yes	yes	yes
3km-FP End (x2)	End (x2)	yes	no	yes
Power recycling	Injection Bench	no	no	no
PR cavity 1^{st} fold	Beam Splitter	no	no	no
PR cavity 2^{nd} fold	Power Recycling	no	no	no
Beam Splitter	Beam Splitter	no	no	yes
SR cavity 1^{st} fold	Signal Recycling	no*	no	no
SR cavity 2^{nd} fold	Beam Splitter	no*	no	no
Signal recycling	Detection Bench	no*	no	no

Table 14: *Locations and main features of the payloads. *TBC*

13.1 The New Marionette

In the new marionette design the usual requirements for cleanliness, vacuum compatibility, mechanical precision, magnetic and electrical properties apply. Moreover several new aspects must be considered: the use of the fused silica fibers and the change of geometry of the mirror.

In the case of the monolithic suspensions, the silica wires must be attached to the marionette by a new kind of clamps which must not introduce further mechanical losses in the interface between the silica and the marionette surface. These new clamps have to be placed in such a way the fibre bending point lays on the horizontal plane passing through the center of mass of the marionette to minimize the coupling between different degrees of freedom. As the wire bending section is different by the clamping section, because of the tapered fibre tip (sec. 13.6.2), this is carefully taken into account in the new design.

The coupling between the marionetta and the fibre also influences the mounting procedure of the payload and consequently the new assembly tool design.

Moreover the change of the position of suspension wires of the new reference mass, and, in case of need, of the balancing motor, are taken into account.

Finally, the design is conceived in such a way to avoid any risk of fiber rupture, both during the assembly and the operation.

A complete FEM analysis of the new marionetta, has been very helpful to ultimate the design (see figure 37).

Figure 37: A picture of the new marionette designed for Virgo+ monolithic suspensions. The black dielectric arms are in Peek CF30.

The AdV marionette, developed in the context of Virgo+, will be characterized by a relevant feature concerning its centre of mass that will be located closer to the suspension cable bending point (2 mm below) and will be adjustable at the level of payload assembly. This requirement arose from the experience of suspension control during Virgo commissioning.

13.2 The Mirror Reaction Mass

In the new mirror reaction mass (RM) design the usual requirements for cleanliness, vacuum compatibility, mechanical precision and magnetic and electrical properties apply.

The new design takes into account the bigger thickness and mass of the mirrors, the implementation of the mirror control and the thermal compensation system.

The RM surrounds the mirror in order to protect it by accidents and hosts its actuators. It is equipped with safety stops that must be redesigned taking into account the different shape and increased mass of the mirrors suspended with a monolithic structure.

The design is conceived to host the ring heater and compensation plate foreseen in the thermal compensation system. To this aim, the dielectric parts of the RM must work at high temperature because of the possible contact with the heaters.

The presence of a compensation plate (see sec. 9) could deeply affect the dynamical behaviour of the last stage suspension: the centres of mass of mirror and RM must coincide

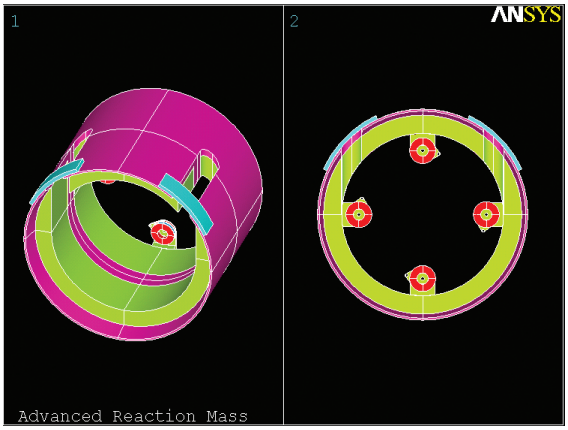

Figure 38: Schematic picture of the new mirror reaction mass. The various colours indicate the different materials used.

to reduce the coupling among the various degrees of freedom. The structure required to carry the compensation plate will make more difficult to satisfy this requirement. This aspect must be carefully studied.

The actuators have to be dimensioned to fulfill the displacement requirements for the locking purposes and consequently are related to the optical configuration. Moreover these actuators must not introduce extra noise that can spoil the sensitivity curve. Coil-magnet actuation [142], is currently the reference solution. Hence it is necessary to use a dielectric material for the reaction-mass in order to avoid eddy current dissipation and magnetization effects. The mechanical strength of the new insulating material must allow to use the reaction mass also as a safety structure for the mirror.

The design of the RM can be similar to the one of Virgo+ which is composed by different parts (see figure 38): an inner dielectric hollow cilinder wact with the mirror sides and an outer stainless steel part, far from the coils, which makes the RM structure stiffer and increases the overall mass. The dielectric material has been chosen to be UHV and cleanliness compatible. The use of a dielectric material could give rise to the problem of the mirror static electric charging by friction with the RM. The market offers several kinds of high technology plastic or ceramic materials that can be useful for our purpose. The reference solution, adopted for Virgo+, is the TecaPeek CF30, a kind of polimeric plastic, loaded by carbon and grafite particles to increase its density and have a slight electrical conductivity which is useful to avoid the static charges formation.

13.3 The Marionette Reference Mass

A new configuration for the last stage suspension system is being studied for AdV. It will include a new element: the Marionette Reference Mass (MRM). The implementation of that new element is essentially motivated by the need of simplifying as much as possible the installation of payloads with large mirrors and monolithic suspensions. Indeed AdV

payload installations must be performed safely and exploiting at the best the volume available in the vacuum chambers at the base of suspension towers.

In Virgo and Virgo+ four shafts (F7 legs), attached to the last superattenuator element (F7 steering filter) and holding the coils dedicated to marionette control are housed into the HV section (10^{-6} mbar). That upper vacuum chamber is prolonged downwards forming four large cylindrical pots. In between the coils and the magnets, meant for marionette actuation, the pots are made of metal-coated Kapton disks. In such conditions the mechanical clearance for the payloads and the room for human actions, as payload frame delivering, balance and pre-alignment, become critical for AdV.

MRM (fig. 35) is conceived as a body with axial barycentric suspension clamped just below the conductance pipe (UHV vacuum section, 10^{-9} mbar) to the same wire suspending the marionette. It has been conceived to

- act as reaction mechanical reference for marionette actuation by holding the coils formerly attached to F7;
- allow the suspension of mirror with larger diameters avoiding any mechanical interference between the marionette and the pots;
- simplify the payload installation and greatly simplify the preliminary alignment procedure;
- preserve high level of mirror cleanness by installing quasi-laminar air flux ducts in the upper part of the payload vacuum chamber (TBC).

Changes in the suspension system structure will also have an impact on the hierarchical control strategy of the mirror. A structural change of payload and F7 (that will be more compact) will require a detailed study of the dynamic behavior and a careful compensation of the recoil effect. The design has also to be exploited to reduce the coupling of suspension oscillations into payload tilt, leading to further overall improvement under the worst microseismic conditions.

A prototype suitable for being suspended to a real susperattenuator has been developed supported by detailed FEA [143] that allowed a preliminary characterization. The prototype has been shaped as a four-petal flower having structural internal modes in the high frequency range ($f > 200$ Hz). The MRM assembling, recently carried on, has been quite important to better define the wire suspension system to be adopted for the installation of the payload. In addition, even if the design is not the final one, MRM full-scale prototyping will greatly help in delineating the suspension feedback control strategy for AdV.

13.3.1 Multi-mirror payload

In this section a baseline limited to the actions to be performed pursuing in the direction of specific payloads dedicated to the NDRC is described.

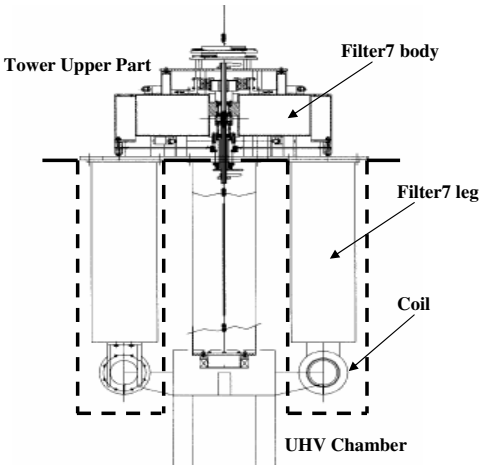

Figure 39: Technical drawing of the F7 body and legs. The dotted line in the picture represents the separation limit between the two vacuum compartments. The mechanical supports (F7 legs) of coil actuators faced to marionette permanent magnets arealso visible.

In Sec. 13 the reference solution considered for the implementation of NDRCs foresees design of a multi-mirror payload for the Beam Splitter superattenuator. In order to allow the installation of more complex payload the legs of the last filter of the superattenuator should be reasonably shortened and an intermediate mass will be needed. In Virgo+ lock force reallocation to the Beam Splitter marionette is not mandatory to reduce driving noise and according to preliminary estimates the situation remain the same for AdV. Then three systems of pendulums, two stages (reasonably simple double) to orientate the two folding mirrors of NDRCs and a quasi-standard double-branched stage (standard marionette hanging reaction mass and BS). Hence the role played by the intermediate mass mentioned above will not be exactly the same as that of Marionette Reaction mass for monolithic suspensions (i.e. to apply internal forces to the mirror marionette); indeed, it will be used to control the angular position of the whole multi-mirror payload. Thus, once such position will be in the range of few mrads all the three lumped systems DC orientated independently through their respective balance motors and the mechanical notch of the Beam Splitter branched suspension (marionette) will preserve the the intermediate mass from the recoil of the locking force. The Beam Splitter marionette will be controlled at low frequency with respect to the intermediate mass.

Remarkably, from preliminary estimates, the accuracy of actual optical levers in use for Virgo+ should allow to bring the system in the linear range of automatic alignment and a detailed study towards the final design goes through the following items:

1. Electromagnetic cross talk among actuators in order to set the minimal distance.

2. Optimal geometry for the intermediate mass and actuation strategy for controlling its position: short legs from F7 might be conceived. Its position can be read with respect to the ground by means of a standard optical lever, while the angular

position of the marionette can be read-out by means of a system similar to the standard one. Once the intermediate mass is controlled the BS marionette will have to follow it through a narrow band servo.

3. Actuation strategy for the two folding mirror stages (reasonably directly from the intermediate mass).

4. Mechanical response at the level of A) folding mirrors B) their steering stages (if double), C) BS, D) BS marionette, E) intermediate mass. This study can be performed by means of an analytical model successfully cross-checked during monolithic payload prototyping.

5. Optical levers for controlling the two folding mirrors (one optical lever each: 2 tilts + 1 longitudinal dampers)

6. SW study of ray tracing and diffused light into the BS vacuum chamber will be a serious issue that has to follow step-by-step the development of BS payload design.

7. Local controls of such a sophisticate system must be studied also from the point of view of the hardware components needed outside the BS vacuum chamber (as optical ports, benches etcetera...).

The overall scheme relies on the possibility of performing angular control in the range 0.1-2 Hz by acting directly on the BS and it will be mandatory to keep the beam well centered on it (within 1mm), a condition that in Virgo is actually obeyed only by FP cavities mirrors.

Finally the issue of the differential pressure, causing a torque on the Beam Splitter payload imposes some constraint to the locking hierarchy, in terms of NDPRC stored power with respect to the servoes involved in BS local control. As the design is close to the completion a strict interaction with ISC group will be needed.

13.3.2 Recycling cavity suspensions on benches

According to the reference solution two small mirror suspensions will be hosted onto the benches (INJ,DET). The main issue in this case is the room on the bench and this development is highly interlaced with the development of those benches. These systems will certainly require full chain of local controls dedicated to control and recover their position with respect to the sensors placed outside the vacuum chambers. ISC will define the reference solution the strategy of NDRC longitudinal control. From the perspective of PAY the main issue is related to evade the recoil due to the action on NDRC mirror sitting on benches and the related breadboards. Once the mechanical scheme will be even preliminarily designed a standard optical lever system will be easily deduced. In principle provided the existence of one folding mirror equipped with standard payload the angular correction dynamics can be attained by allocating to it the low frequency component.

13.4 Mirror local control system

The main function of local control system is to drive the position of the mirrors in the signal and dynamical range of automatic controls even starting from very large misalignments related to the presence of a low frequency suspension. During the commissioning this system has to ensure both robustness and control low-noise in order to gradually drive the interferometer towards the delicate phases of locking and automatic alignment in various intermediate configurations. The control is limited by the ground seismic noise and acts in the range $5 \times 10^4 - 0.02\,\mu$rad. Mirror local control of AdV system will be similar to that implemented in Virgo. However, given the Virgo experience and the new design of AdV payload one can delineate few main constraints for the update of the system. They are listed below each followed by a concise motivation.

(i) Coarse mirror control The existence of further bodies attached to the mirrors should be reduced. If it will not be possible to prevent the need of dynamical re-alignment the markers will be attached to the rear face of the reaction mass. Their use through the novel CCD imaging will provide the same performance as those located on the mirror main face. The system has been successfully tested using the monolithic prototype facility.

(ii) Additional degrees of freedom A further optical lever with incidence on the mirror reaction mass will be used to damp transversal pendulum oscillations of the payload. Such a system is already installed in the monolithic prototype test facility and will be implemented in Virgo+, provided that the optical ports are in principle available. Moreover a sensing stage at marionette level will be completed by adding the optical and electronics components for reading the longitudinal displacement. Such implementations are considered as a reference solution for AdV payloads in order to facilitate the locking process.

(iii) Large oscillation prevention Large oscillations of the payload are normally prevented by digital control guardian, however the experience shows that they can still occur and that they are due to SA control operation or hardware failures. In long suspensions the effect is quite reduced by the presence of the conductance pipe between the payload and the marionette. Provided the use of monolithic fibre suspensions and the possible novel design of the payload (MRM) a suitable system of motorized stops, preventing misalignments and oscillations larger that $\pm$ 7 mrad would bring the system in the range of optical levers through the standard viewports using standard PSD devices, with the further advantage of simplifying the local control setup, which would make the use of CCD optional.

(iv) Remote optical diagonalization The efficiency in separating the degrees of freedom by means of optical diagonalization reachable with Virgo equipment is significant (0.2-0.5 %) but the access to the location of local control micrometric slides have occurred more frequently than expected. Motorized control would significantly improve safety conditions (it is close to viewports) speeding up the process of PSD slide readjustments after maintenance interventions.

(v) PSD amplifiers The PSD amplifiers used for Virgo+ need an upgrade to improve the system sensitivity both to better match the new ADC resolution and to improve the general performances. A careful design of the amplifier power supplies is needed to avoid electromagnetic interference in the close environment, since these devices are placed close to the suspension towers.

The local control facility used to test, in air, the Virgo+ payload with monolithic suspension is very similar to the Virgo standard. It allowed to compare the payload equipped first with steel wires and then with fused silica fibres. The transfer functions of all the d.o.f. but roll, vertical and transversal pendulum (x) have been easily measured and the payload have been controlled using both marionette and mirror optical levers and acting from ground and reaction mass. In Virgo+ it is foreseen to install the x damper using a further optical lever (item ii above). Vertical resonant frequency measurements using an accelerometer have been performed on the prototype allowing to close the and refine the analytical model in order to use it as a guideline for designing the final marionette of Virgo+ (that is the reference solution for AdV).

From the point of view of local controls no significant difference occurs passing from steel to fused silica wires. Monolithic suspension prototype is robust with respect to tilt and translation oscillations, even sustained at the level of an excitation caused by control operation failure occurring at the payload level $20 - 50$ mrad$_{0P}$, 5 mm$_{0P}$), for several days.

13.5 Monolithic suspensions

Monolithic fused silica (FS) suspension of the four 42 kg Fabry-Perot cavity mirrors will be realized for AdV, exploiting the experience achieved developing the Virgo+ payload. The optimal geometry and technology is being pursued with the objectives of minimizing the pendulum thermal noise, fulfilling the requirements for an optimal control of the test mass, ensuring safety and reliability. For Virgo+ a large amount of work has been made to reduce the risk in the welding procedure. The fibers (once welded directly to the mirror) are now welded to intermediate components (called ears) silicate bonded to the lateral flats of the test mass. The former procedure induced a lot of thermal stress on the bonded surfaces that could damage the silicate bonding and eventually break it. Another problem is that the fibers pass through a dangerous manipulation procedure that can open cracks on their surface decreasing their breaking strength. To recover these problems a new technique has been developed: two lateral supports with vertical grooves are attached using silicate bonding to the mirror lateral flats. Fibers are produced apart from a fused silica bar previously welded to an upper clamp and a lower anchor. The fibers are then placed in position clamping the upper part to the marionetta and inserting the lower anchor below the lateral supports bonded to the mirror. In the end the anchor and the supports are bonded together through silicate bonding or *water glass*.

13.6 Geometry, dimensions

In this section the preliminary considerations that drive the design of the monolithic suspensions are presented. Breaking strength is not the only parameter that matters. The AdV test masses will weight 42 kg. They will have a diameter of 350 mm and a thickness of 200 mm. Such mirrors are twice as heavy and thick with respect to the Virgo and Virgo+ test masses.

13.6.1 Lateral support machining and clamps

The suspension scheme tested for Virgo+ will be applied for AdV trying to reduce the most critical part induced by silicate bonding the lateral supports on the lateral mirror flats.

The suspension scheme proposed is the following: one fused silica part called "anchor" will be welded to a 1.5 mm fused silica bar and to an upper clamp. Using the CO_2 laser machine the fiber will be produced from the bar welded to the clamps, the whole clamp-fiber will be placed in position on top to the marionetta and on the bottom under the mirror support. The contacting surfaces of the two parts (both with a polishing) will be bonded onsite using the silicate bonding or *water glass* procedure as for Virgo+.

To this aim it is necessary to find a geometry of the lateral supports easy to machine, and to demonstrate that the surface quality is sufficiently good for thermal noise performances.

As anticipated in the section 13.1 the role of the upper clamps coupling with the marionette in order not introduce further frictions and recoil losses is very important. For this purpose a stainless steel box has been carefully designed with the aim to host the silica upper clamp and to attach it to the marionette without introducing further losses (see fig. 40). The steel box is formed by two pieces. An external one fastened to the marionette by four screws. An internal one in direct contact with the fused silica and fastened by lateral screws to the external one. The silica core is kept fixed in its box by an upper lid fastened by screws. The steel inner box is also designed as the support of the upper clamp during the fiber pulling (see section 13.6.2) and then is coupled to the tool used to insert the fibre on the marionette lateral side, as foreseen by the assembly procedure. In the frame of the development of Virgo+ monolithic suspensions, optimization tests of the upper and lower clamps will be performed in the facility in Perugia. A pendulum composed by one of the fibers produced for the payload suspensions, coupled to an upper clamp and a lower clamp, and loaded with 1/4 the mirror mass, about 5 kg will be used. With this set up, the maximum Q value which could be measured in the facility will be about 6 10^7, very close to the value expected for the monolithic fibers, 7 10^7.

13.6.2 Fibres geometry and properties

Fibre length, fibre stiffness and position of bending points are driven by the room available and the choice of resonant frequency of the various modes of the suspension. This choice

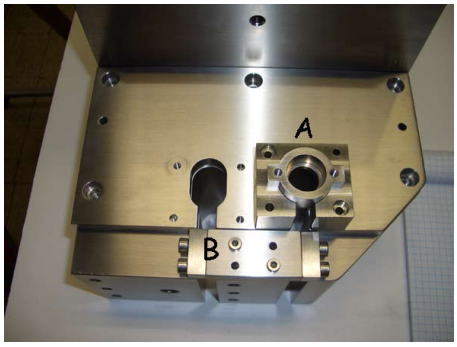

Figure 40: Photo of the wire clamps on the marionette. A. Steel box for the silica upper clamps. B. Reaction mass wires clamp.

depends strongly on control issues and a careful investigation is being carried on. The vertical bouncing frequency of the last stage represents the lower limit of the detection band because although the vertical to horizontal coupling is small (it has been assumed 10^{-3}), the vertical oscillation does not have any dilution factor. The result is that the vertical bouncing mode is clearly visible in the thermal noise spectrum and this frequency must be kept below 10 Hz. In order to have the detection band with the smaller number of resonant modes as possible, the first violin mode should be as high as possible. The position of the violin mode depends on the fibre cross section and then ultimately on its breaking stress. A violin mode at about 430 Hz is about 100 Hz higher than what can be obtained with steel wires.

Fused silica fibres are presently produced for Virgo+ starting from high purity fused silica cylindrical bars commercially available 1.5 mm thick. A machine for pulling fused silica fibres using a CO_2 laser has been developed at the University of Glasgow [144]. A duplicate of this machine has been assembled in a dedicated laser room at the site of the Virgo experiment. After modifications of the optical path the 100 W CO_2 laser provides enough power for welding the rod to the silica parts used for realizing the monolithic suspension. The fibre is then pulled directly from this welded rod.

Due to the low thermal conductivity of silica the thermoelastic peak of 400 μm diameter fibre is at 11 Hz. At this frequency the fibres mode shape is almost straight and the only significant bending is at the upper and lower ends. Using the effect of non linear thermoelasticity it is possible to demonstrate that exists a stress at which the thermal expansion and thermal elastic compliance compensate each other and that this stress for fused silica is in the range 200 MPa to 250 MPa. All these data seem to indicate that the fused silica fibre with a dumbbell shape has the lowest thermal noise. The possibility to control the pulling velocity offered by the CO_2 pulling machine allows to realize tapered fibres with a profile that is reproducible with a precision lower than 10 μm.

The bending length λ of the suspension is the distance of the fibre bending point from the clamped end. Positioning the bending point on the center of mass plane of boththe marionette and the mirror allows minimum coupling between the different degrees of

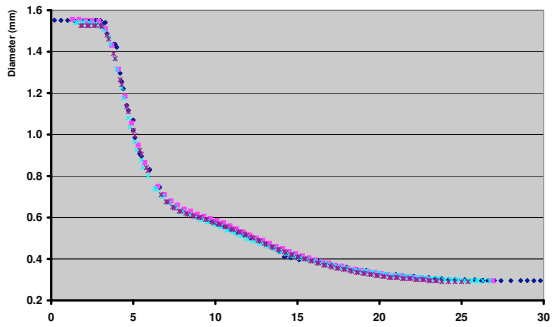

Figure 41: Profiles of the 'neck' region of several 280 μm diameter fibres: the superposition of the curves shows the good reproducibility of the fibre shape.

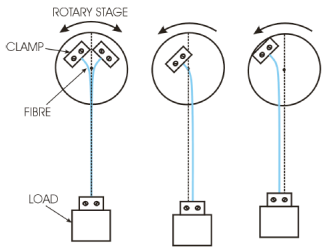

Figure 42: Sketch of the setup used for a direct measurement of the fibre bending length.

freedom; it is also possible through a simple model of the fibre based on the knowledge of λ to study its dynamical behaviour. The tapered profiles of the fibres near the heads require this quantity to be directly measured. For doing this a specific instrument was realized [145]. The fibre is clamped to a rotary stage, suspending a load as close as possible to the working conditions. If the bending point is placed exactly on the rotation axis of the stage, when the top head of the fibre is rotated, the bottom part of it actually does not move. Acting on a micrometric sleigh moving along a diameter of the rotary stage it is possible to find a position where the fiber movements get their minimum amplitude, thus having a measurement of the bending length. This device provides also an easy way to measure the first violin and bouncing frequencies. The results obtained for some of the 280 μm diameter fibres suspended to a 5 kg load are summarized in table 15.

Violin mode (Hz)	Bouncing mode (Hz)	Distance between b.p. (mm)
435±1	5.9±0.1	692.0±0.2
434±1	5.9±0.1	691.9±0.2
434±1	5.9±0.1	691.6±0.2

Table 15: First violin and bouncing modes frequencies and measured fibre lengths between bending points for some of the 280 μm diameter fused silica fibres realized for Virgo+.

Advanced Virgo Baseline Design:
PART 4:

Electronics, Vacuum, Infrastructures

14 Electronics, controls and data acquisition

The Electronics, Controls and Data Acquisition subsystem (DAQ) comprises the hardware and software components used for data acquisition and distribution, global control of the interferometer, environmental monitoring and also general purpose components used to perform control or monitoring on selected devices of other subsystems. The subsystem also includes the electronic and software infrastructures needed for carrying out the listed tasks, but the front end electronics belonging to other subsystems.

14.1 Overview

This section describes the most important components of the DAQ subsystem foreseen for AdV. The main upgrades, with respect to the Virgo+ configurations are discussed. For the advanced detector, in fact, it is expected to perform more effective and less noisy controls, to increase the number of the suspended optical components to control, and, in general, to manage a larger amount of signals with respect to Virgo+, while the general architecture of the whole system will be not changed.

The main subsystem components are:

- Data Acquisition and Global Control
- General Purpose DAC Boards
- Local Position Read-Out and Beam Imaging
- Environmental Monitoring
- Electronic Infrastructure
- Control Software Framework

14.2 Data Acquisition and Global Control

The Data Acquisition and the Global Control system employs the same hardware and logical architecture, even if they fulfill two very different task. The general architecture of these systems is described in details elsewhere [146],[147]. It is, in fact, very similar to the architecture implemented for the Virgo+ detector and only few upgrades are foreseen to face the upgrades foreseen in AdV. In particular the increased data flow coming from the new optical layout and from the additional systems foreseen for the interferometer control, and the increased complexity of the digital control section used for calculating the corrections from the global signals, both for the locking and the alignment, due to the increased degrees of freedom of the full interferometer.

The most important upgrades of AdV that will affect the Data Acquisition and the Global Control are:

- Enhancement of the Thermal Compensation System (TCS) and Phase Cameras;
- Introduction of the Signal Recycling (SR) system;
- Auxiliary laser and sensing system for the locking of high the finesse cavities (CALVA);
- Introduction of the marionette reference mass (MRM) equipped with sensing and actuation systems;
- Introduction of tilt sensing and control in the superattenuators (SAFE).

Nevertheless the performances of the DAQ and GC systems are already compliant with the AdV requirement, both for sustaining the increased data flow and for managing the more complex control system. Moreover this system does not require any new development, but the addition of new components to the existing one to manage the listed upgrades.

Both the Data Acquisition and the Global Control are based on the use of:

- Real Time Computer (RTPC). In the case of DAQ, they are dedicated to the collection of data coming from the ADC, through dedicated non commercial hardware, and to their organization in frame to send to the upper level DAQ devices. On the Global Control side, the RTPC have the role of computing, with fixed latency, the correction signals starting from the error signal coming from the photodiodes and quadrants associated to the different beams of the interferometer.
- TOLM and MUX-DEMUX Boards [148] [149]. The TOLM (Timing & Optical Links Mezzanine) provides for the timing and data exchange between the transmission media, namely a fast optical link, and the hosting hardware, usually the PCI bus of the RTPC. Since all the systems collecting or sending data for Data Acquisition or Global Control purposes are equipped with this mezzanine, it becomes very easy to distribute the signals along the chain. Of course, since the data collected by the different RTPCs have to be sent to few main collecting computers, it necessary to introduce an intermediate system able to collect the data coming from different sources and to drive them to the selected destination. This is exactly the task of the MUX-DEMUX boards. This couple of devices constitute, in this way, the main digital data gathering system, both for DAQ and Global Control, from the data production systems (ADC, DSP, RTPC) to the collection (DAQ RTPC) or the control (DSP, GC RTPC) systems.
- Timing System [150]. The timing system is used to synchronize all the digital systems used for data acquisition and control, and to ensure the right timing for scientific data. It provides for different timing signals, all coherent with the main one as received from the GSP and distributes it to acquisition sections.
- ADC Boards [151]. The analog to digital converters are used both for digitizing photodiode and quadrant signals, as well as for acquiring monitoring or other sparse signals. The ADC boards have 18 bits resolution and are equipped with a digital output, consisting of a fast optical link, that greatly facilitate the distribution of the collected data to the other components of the Data Acquisition or Global Control.

Also the software packages used for the data acquisition and control, need to be upgraded for the AdV architecture.

14.3 General Purpose DAC Boards

This task aims to the development of a general purpose digital to analog board, to drive all the fast actuators outside the suspensions, like PZT or galvanometers for auxiliary mirror steering. Currently this task is performed by using standard VME DAC board, managed by a VME CPU located on the same bus. In the new DAQ and Control architecture this simple solution is no more practical, while a design similar to the one adopted for the ADC is best applicable. In this scheme the data arrive on the DAC board through, an optical link, from a computing element, (RTPC or DSP). Two solution are possible and will be explored during the design phase.

- External TOLM Adapter for suspension mezzanine: use of a standard DAC mezzanine, already foreseen for the suspension control [152], equipping it with a TOLM adapter for receiving data and timing.
- Development of a DAC interfaced with TOLM: development of a new DAC board, similar to the ADC one, using the same hosting hardware.

14.4 Local Position Read-Out and Beam Imaging

Both the local position sensing of the suspended mirror and the beam imaging on the detection benches are performed by using CCD cameras. Hence these devices constitute an element of the control system, since the signals they provide, are widely used for the alignment and for the beam position monitoring. This system also include the electronic drivers and software to manage the cameras, to elaborate the images and to translate them in suitable signals to be send to the control system.

The main upgrade of these components is foreseen in Virgo+, while for AdV a small number of such devices are required for the local control of the SR mirror and for the imaging of the additional beams that will be necessary for the interferometer alignment and locking.

14.5 Environmental Monitoring

The high expected sensitivity of AdV requires a very carefully designed environmental monitoring system, since the coupling of ambient noises will be more challenging with respect to Virgo or Virgo+. Anyway the experience gained during the Virgo functioning is a fundamental guide in this task, both in sensors choice and placement in the most critical part of the interferometer.

Nevertheless a general improvement of the system performances has to be achieved, mainly in terms of probe sensitivity, both for a fruitful noise hunting during the commissioning phase and for an effective vetoing system during the scientific runs. The general upgrade of the environmental monitoring has also to take into account the presence of the new SR tower, that needs to be equipped with all the standard sensor.

As usual the environmental monitoring system is divided in two part: the slow monitoring and the fast monitoring, depending on the nature of the parameter to monitor.

- Slow Monitoring. The slow monitoring system has the same general architecture as in Virgo+, but the distributed modular acquisition boards will be changed due to their obsolescence and to increase the resolution of the onboard ADC. Moreover the architecture will be simplified thanks to the use of standard network components, increasing the system modularity and reliability. The new modular acquisition board are equipped with 32 channels 16 bit resolution ADC. The communication with the managing computer is foreseen through standard network connection, using the Mod-BUS standard. A standard PC will be used to collect the data coming from the network of such modules. The old modular system produced, in certain conditions, unwanted RF contamination caused by the HF modulation used on the communication link. To avoid such kind of problem, the new system will be carefully shielded in metallic boxes and optical fibers will be used as link between the module and the network switch connecting the systems with the master computer. Also the most useful probes of the slow environmental monitoring, namely temperature and humidity probes, need to be upgraded with more effective sensors, with higher accuracy with respect to the present situation, reducing the need of periodic sensor calibration. The conditioning electronics of the probes need also to be upgraded to better fit the dynamic range of the digital converters user to collect the data, allowing a full exploitation of the probe performances.

- Fast Monitoring. The fast environmental probes, and related conditioning electronics, have to be upgraded to increase the monitoring system sensitivity in the case where the disturbance dynamic range is significantly smaller with respect to the converter range. Most of the actual sensors can be upgraded simply by modifying the conditioning electronics, also taking into account that the increased dynamic range of the new ADC will allow an enhancements of the sensitivity for the sensors that are currently not limited by the electronic noise. Moreover the new ADC will integrate also shaping filters that could relax the requirements for the signal conditioning. For some sensors a major upgrade is required:

  - Episensors: the sensitivity of these probes is not at limit, but due to the slow drift of the DC content, it is difficult to increase their response without saturating the conditioning electronic. In particular it is necessary to filter out the low frequency part of the signal before the amplifier. Since these sensor are limited, in the low frequency range, at about 100 mHz, this change will not compromises the effectiveness.

  - PZT Accelerometers: the current probes have limited sensitivity and the con-

ditioning electronics is too noisy to allow further gain. It is necessary to change the sensors to gain sensitivity.

– Magnetometers: the high sensitivity produces, in some conditions, a saturation of the probe due to the 50 Hz contamination in the environment. To overcome this problem the conditioning electronics was modified to reduce the sensitivity, but the likely lower electromagnetic background foreseen in the buildings for AdV should allow the reverting to the original sensitivity.

Finally, due to the larger number of system to monitor in AdV, with respect to Virgo+, the total number of fast sensors should grow by a small amount: at least 2 low frequency seismometers and 2 microphones for the end buildings and 3 PZT accelerometers for the SR tower and for the TCS benches. In all the other case the existing sensors and conditioning electronics will be used.

14.6 Electronic Infrastructure

The electronic infrastructure includes the selection and design of general purpose electronic equipments, in particular:

- Racks: as standard structure to host electronics equipments;
- Crates: both EUROCARD or VME for hosting, powering and connecting different purpose electronics boards;
- Power Supply and DC distribution: using suitable power supplies aimed to minimize any RF contamination in the environment;
- Cabling: Standard or special cabling to allow interconnection between the electronics distributed in the experimental area.

These equipments are expected to be implemented also for standard front end electronics used in other subsystems. In this case they will be developed inside the DAQ system. Special equipments needed by other subsystem are instead not considerer and remain under the responsibility of the corresponding task. Of course a common interface with the rest of the DAQ system, if suitable, will be stated.

14.7 Software Framework

The control of large experiment like AdV constitute classical examples of a heterogeneous Distributed Control System (DCS). When looking at the software part of these systems there are several functionalities that can be found in all of them, which constitute their fundamental services:

- Communication: allows that the components (control servers and clients) of the distributed system communicate among them
- Online database: refers to the possibility to access online any data point of the DCS

- Configuration database: keeps and manages the configuration data
- Logging: collects the logs from all over the system and presents it to the operator

At the beginning of the Virgo Project the choice made at that time was developing a complete custom software framework in which the majority of the mentioned services and functionalities are implemented. Over the years, this framework has been made more robust and has demonstrated to be able to satisfactorily support the experiment operational phase like during VSR1. Within the scope of the upgrades to be done for AdV is reasonable to bring the question if the existing custom framework is still a viable choice. If the current framework has to be maintained the software maintenance could become a relevant issue especially in case of major Hardware or Operating System upgrades.

Since different solutions are available and largely supported, a change of the existing one has to be considered. A first survey about possible different software frameworks was already started [153].

15 Vacuum

15.1 Requirements

15.1.1 Vacuum level

The enhancement of the Virgo sensitivity by a factor of 10 requires an improvement of the present vacuum level to lower the phase noise given by the residual gas inside the 3km long arm tubes. At present the system operates at about 10^{-7} mbar (dominated by water) altough it has been designed and tested to reach a base pressure below 10^{-9} mbar (dominated by hydrogen) after an overall bake-out. A typical spectrum of gases recently taken in the Virgo west arm is reported in fig. 43.

The lowest point of the AdV sensitivity curve: $3\,10^{-24}/\sqrt{\text{Hz}}$ at 200-400 Hz is not compatible with the present residual gas noise, as shown by fig. 44 .

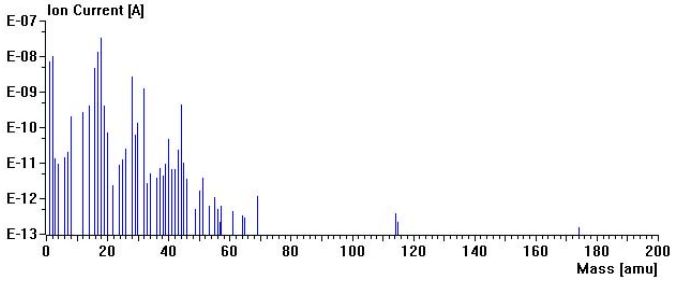

Figure 43: A recent measurement of residual gas composition in W arm. Horizontal axis reports the ratio mass/charge of the ions and the vertical axis the corresponding current, proportional to the partial pressure. The dominant peak is the one at mass 18, water. Total pressure is about 10^{-7} mbar.

Taking into account all the main species composing the residual gas at the presently attained pressure, the corresponding noise is at the level of $10^{-23}/\sqrt{\text{Hz}}$. To be not dominant in AdV this noise has to be reduced by at least a factor of 10 (about a factor of three below the AdV design sensitivity). The residual pressure in the tubes has to be reduced by a factor of 100, being the noise proportional to the square root of the partial pressure of the various gas species.

The proposed goal, expected after arm tubes bake-out, is shown in tab. 16, where the contributions of the different gases are reported separately.

The originally planned method of vacuum improvement was based on baking the whole system at 150 °C, the 3km tubes plus the 7 mirror towers. Baking of towers would have to be repeated after each opening of a tower. With the experience gained running Virgo, we have realized that the baking choice as foreseen is not opportune because:

- the long interruption needed after each tower opening affects excessively the interferometer duty cycle (about 1 month to achieve the bake-out procedure, to be

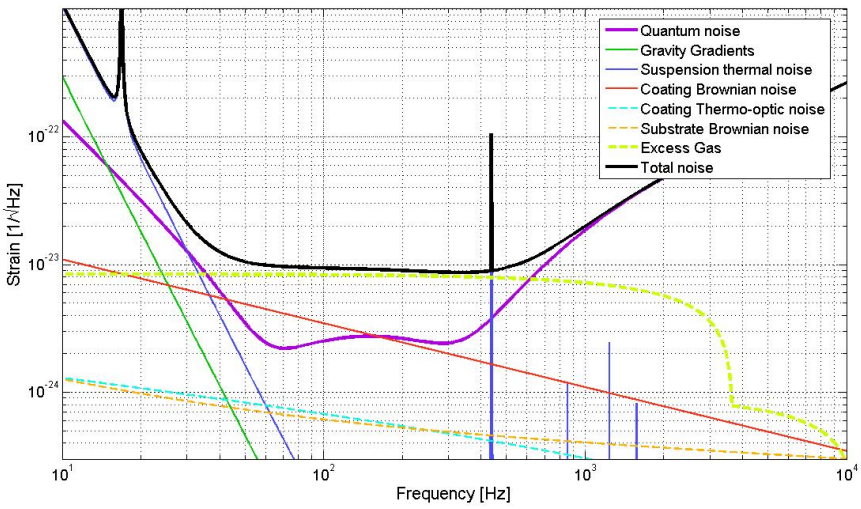

Figure 44: AdV sensitivity curve, as it would be with the present vacuum level, due to the phase noise given by water at a partial pressure of $1.5\,10^{-7}$ mbar. The sensitivity would be limited to about $10^{-23}/\sqrt{\mathrm{Hz}}$

Gas species	**Pressure (mbar)**	**Noise ($\mathbf{Hz^{-1/2}}$)**
H_2	1e-9	2.1e-25
H_2O	1e-9	7.2e-25
air+others	5e-10	6.5e-25
HC	1e-13	3.5e-25
TOTAL	2.5e-9	1.0e-24

Table 16: Proposed goal for phase noise (baked tubes) in the average frequency band.

compared to the present two days);

- unpredictable de-tuning effects are produced by the warm-up of the lower stages of the anti-seismic suspension at 50 °C or more, involving movements/stresses. Furthermore also the re-condensation of contaminants on mirrors and detaching of glued or silicate bonded parts are risks to be considered.

The selected techniques to meet the proposed goal are:

- installing cryogenic traps at tube extremities
- performing the bake-out of tubes only

Cryogenic traps are the classical solution to stop the migration of water from unbaked towers to the tubes. In the present Virgo, during the restart after a tower opening, the gas released from towers (water vapour) spreads in the tubes bringing temporarily the residual pressure near 10^{-6} mbar, orders of magnitude above our goal.

Cryotraps have been already experimented in Virgo and in other large vacuum systems, and can be considered without a long phase of tests and prototypes.

The baking system is already implemented in Virgo, tested and working, hence not discussed here. Cryotraps are presented in the next section.

15.1.2 Further vacuum upgrades

The different optical scheme and the larger beam waist of AdV require a full height tower for the Signal Recycling mirror, a different position of the 'mirror towers' of the central area and new link tubes with larger diameter. Furthermore it is necessary to renew the control system of the vacuum apparatus, to substitute the obsolete parts and to incorporate the new equipment with the updated control logic.

15.2 Cryotraps

15.2.1 Trap geometry and position

Four cryogenic traps will be installed for AdV, one at each tube extremity. Traps will consist in 'hollow cylinder' cryostats, cooled at 77 K with a bath of liquid nitrogen. The selected length is 2.0 m and the inner diameter is 1.0 m, a convenient size to be installed inside the 1.2 m diameter link tubes between the relevant tower and the respective 'large valve', isolating the 3 km tube. The setup will be completed by baffles of aperture 600 mm (diameter) for diffused light and thermal mitigation. With respect to other options, involving the installation of the traps inside the 3 km tube, downstream the large valves, the advantage of the selected choice is both economical and technical: it doesn't require to vent, cut and modify the 3 km tube. Hence the installation work is by far simpler and less risky. Basically, 8 1.2 m diameter bolted flanges shall be dismounted and restored by internal staff, with modest support from external manpower. Main drawback is the larger induced thermal effects on mirrors, because the reduced distance from towers; it is discussed in the next section. The selected trap position for AdV is shown in fig. 45.

The water 'trapping' performances are given by two effects:

- a majority of water molecules hit directly the inner trap surface, due to the geometrical view factor, and stick there: the molecule escaping fraction is 2.3% for a trap with the selected geometry
- large part of the transmitted molecules bounce back from tube walls and re-enters inside the trap, being pumped. The pumping speed is proportional to the trap aperture, about $4 \cdot 10^4$ l/s for the selected geometry.

More accurate calculations have been done both with Montecarlo methods and with f.e.m. models, to take into account the real geometry and the presence of optical/thermal baffles near the trap.

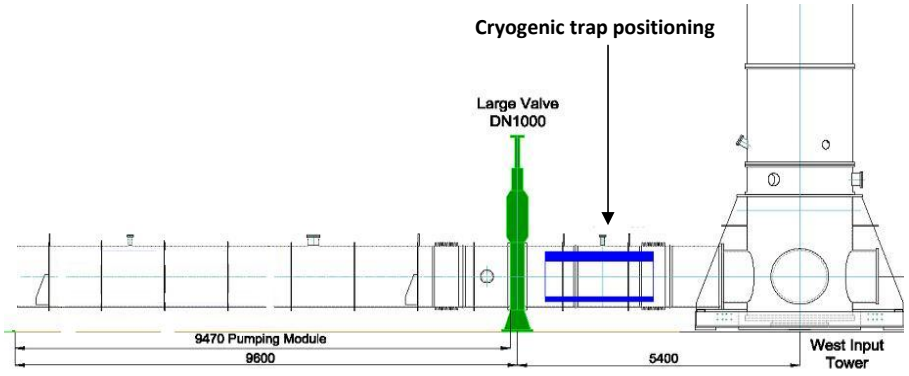

Figure 45: Position of the cryotrap.

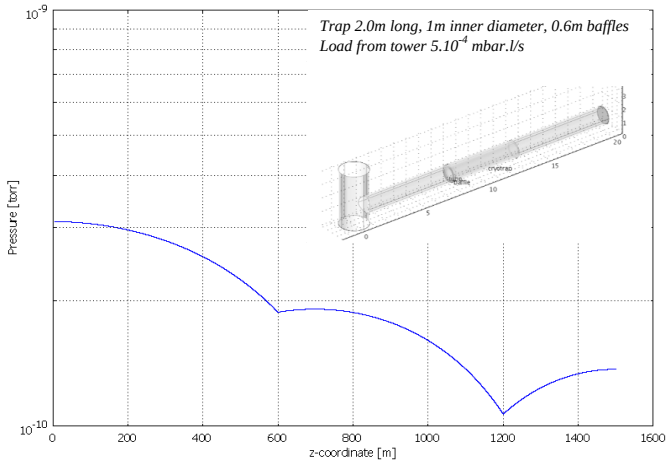

Figure 46: Water pressure profile along the beam tube calculated for selected trap geometry.

We have considered the typical gas load coming from a mirror towers after 2 days of pumping following an opening intervention. The calculated efficacy of the trap is presented in fig. 46, which reports the water profile in the first half of the tube in the above specified load conditions. The result meets the AdV requirements.

15.2.2 Thermal effects on Test Masses

The Cryotrap solution, given the proximity of large surface cooled to liquid nitrogen temperatures with respect to the test masses (TMs), will induce thermal effects on the TMs themselves through radiation. The relevance of these effects, in terms of structural and optical curvature of the TMs, have been analyzed independently by the NIKHEF and Roma Tor Vergata Groups with finite element thermo-mechanical simulations. The two main effects are:

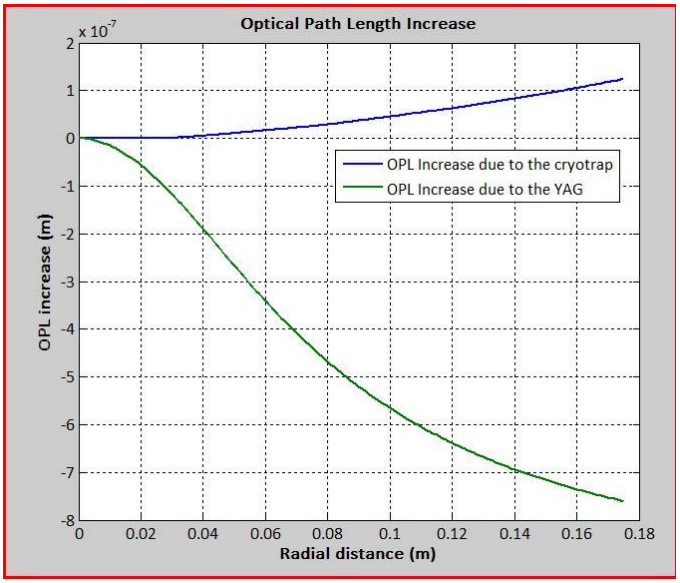

Figure 47: Optical path length (OPL) increase due to thermal effects in the TM. The blue curve is the OPL increase due to the trap, while the green curve is the OPL increase due to the absorption of YAG power.

- a change of radius of curvature of the test mass surface of about 2 m, negligible with respect to its original value of about 1500 m
- a change in optical path length inside the test mass (see fig. 47)

  both are smaller and of opposite sign with respect to the changes due to the YAG beam absorption.

In summary, the thermal and structural effects of the cryotraps on the TMs are negligible.

15.2.3 Optical constraints and diffused light

The criteria applied in Virgo to moderate the diffused light will be applied also on cryotrap design:

- the minimum free aperture radius is about 5 times larger than the average beam radius
- any discontinuity (potential reflecting spot) of the vacuum enclosure is hidden by suitable absorbing glass baffles, with respect to the beam spot on any mirror
- no point of the smooth surface of the vacuum enclosure can be seen contemporarily by the beam spots on two facing mirrors.

Moreover, in the main part of the arm tubes, between two large valves, all the inner surface is hidden by conical stainless steel baffles, with respect to the beam spots on

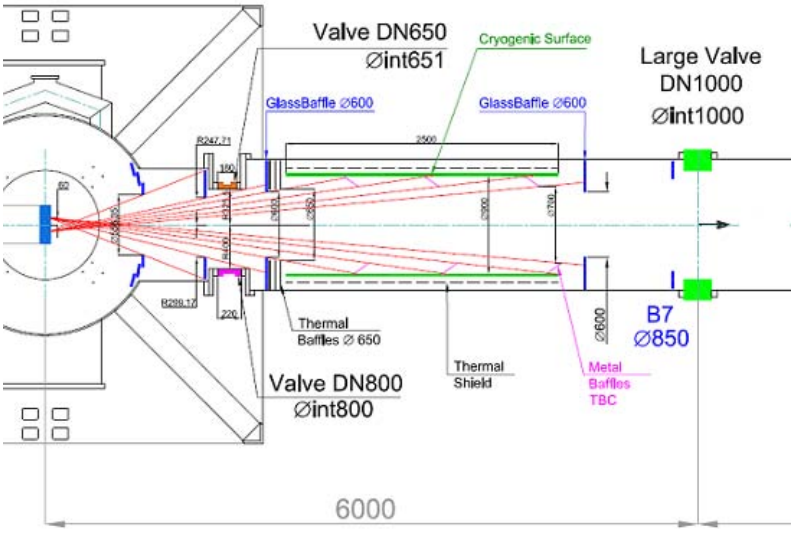

Figure 48: Proposed baffle configuration for the cryotrap. In the upper (lower) part of the drawing is shown the 650 (800) mm option for the additional valve.

the mirrors. This configuration has proven to be largely safe for Virgo. A very similar configuration (see fig. 48) will be chosen for the cryotrap. The size of the additional valves and position and diameter of baffles will be optimized with respect to diffused light.

15.2.4 Cryostat mechanical design

The cryotraps have a cold surface with a length of 2023 mm and a diameter of 1000 mm (fig. 49). The overall length is 3490 mm and the outer diameter is 1208 mm. It will be constructed from stainless steel 304L. The vessel is equipped with pump-out and service ports. Stainless steel hydro-formed bellows are used to accommodate expansion of the structure.

The inner surface of the trap is cooled with liquid nitrogen. The volume of the bath is about 200 l. To minimize boiling and LN2 consumption, this bath is thermally shielded from the outer surface of the vessel by using vacuum and multilayer superinsulation. Since the inner cold surface will move due to thermal expansion (about 3.2 mm/m) with respect to the outer vacuum vessel, expansion bellows are used. These bellows also act as heat bridges that minimize thermal losses due to heat conduction. The LN2 inlet will be designed such that LN2 will flow smoothly into the bath, minimizing any noise induced by bubbling. The liquid nitrogen level in the bath can easily be controlled within ± 10 mm. Note that the bath has a sizable width of more than 300 mm. Again this guarantees that bubbles have an easy escape path to the surface over the entire length of the cryotrap. A separate inlet is provided in order to admit hot nitrogen gas in case rapid heat-up of the structure is needed. The cryotrap can be operated for more than one year before

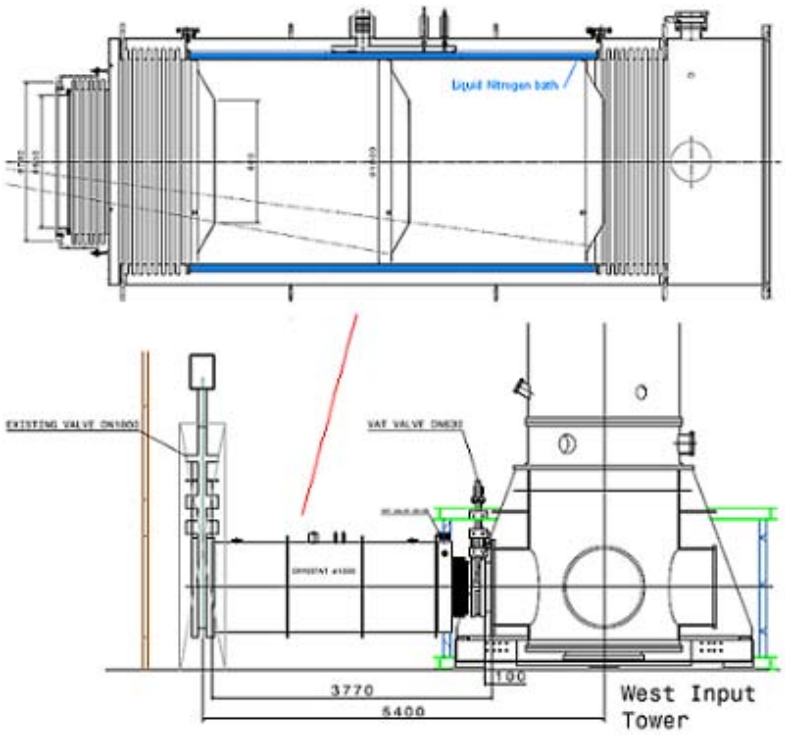

Figure 49: Cryotrap mechanical layout.

regeneration, assuming a load of about 10^{-4} mbar l/s from the mirror vessel. During this time a water layer of about 1 micron will be deposited on the inner surface. This causes the initial emissivity of about 0.1 to increase to 0.2. This relative low value for the emissivity leads to an average heat load of about 300 W, and results in an estimated LN2 consumption of about 3.5 l per hour. In a 'transient' phase of commissioning operations, when towers are frequently vented , the growing rate of the water layer will increase . Regenerations shall be maintained at the level of once per year, allowing an higher LN2 consumption .

Some auxiliary equipment is needed for each trap:

- cryogenic sensors to monitor the temperature distribution and the LN2 level;
- vacuum gauges, to monitor the residual pressure from the atmosphere down to 10^{-9} mbar; also a gas analyzer is needed for diagnostic;
- one turbo-molecular pump + one dry pump is needed for evacuation/regeneration and Ti-sublimation pumps are needed for the UHV service.

15.2.5 LN2 Supply System

The adopted reference design is a "standard" distribution plant based on large storage vessels (one for each trap) and vacuum insulated transfer lines. The lines could also include a multilayer superinsulation to reduce heat leaks and inner bubbling. The estimated overall heat leak for each cryotrap is in the range of 300 W . Typical losses for a 30 m long line with an insulating vacuum of 10^{-2} mbar are estimated to be 50 W or less. Losses of a good quality storage vessel are typically in the range of 1% per day of its content. Taking some extra safety factor we can estimate an upper limit for the overall heat load of 700 W/trap (for 10000 l vessels), corresponding to a liquid nitrogen consumption of 350 l/day per trap, and to 1400 l/day for the four traps. With these consumption rates the refilling of the exhausted LN2 should occur once per month.

15.3 Bake-out of tubes

A complete bake out equipment is already existing and installed in Virgo. No construction costs have to be sustained, apart for consumables: fuel and power generators to be rented during bake-out period. The estimated cost is 300 keur to bake both tubes and we don't consider an additional cost for AdV. Bake-out of the tubes could be performed in a second step, when convenient for commissioning activity, allowing a simpler start for the vacuum system together with a favourable distribution of the manpower and of the economical effort. Thanks to the cryotraps, a base pressure around 10^{-8} mbar shall be obtained in the tubes without baking, allowing a first period of interferometer commissioning. When required, both tubes shall be baked during a stop lasting 2 months .

15.4 Enlarged links

The *links* (vacuum tubes) connecting the various towers in the Central Building have to be replaced for different reasons:

- the positions of the towers will be changed by up to one meter along the beam direction
- the clear apertures of the links have to be increased since:
    1. the average radius of the beam in the central zone will be 60 mm, instead of the present 21 mm
    2. the optical lay-out of the interferometer may require a clear passage for multiple beams between the towers, needed to have not degenerate recycling cavities and widely separated pick-off beams, as produced by large wedge angles in the mirrors.

The length of the six links will range between 2 and 4 m, including bellows to allow thermal expansion and, possibly, valves to separate the towers. We consider a general scheme of links of 1 m with or without 650mm valves (fig. 50) that is adaptable to

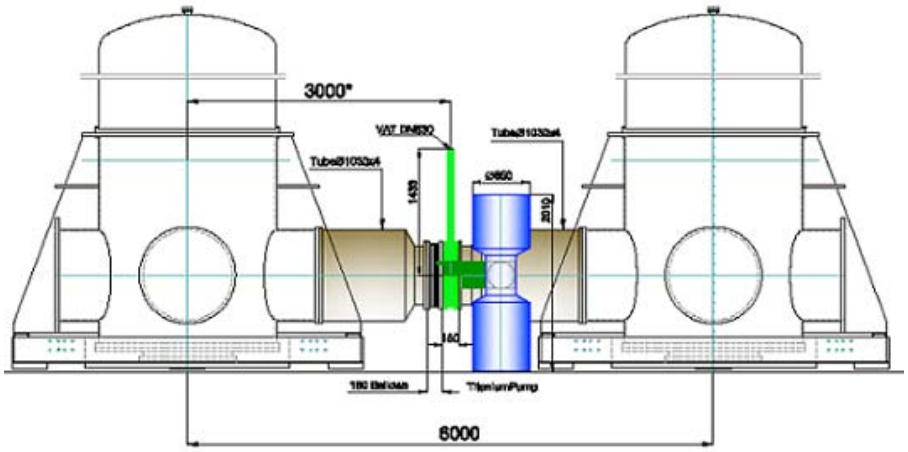

Figure 50: Enlarged link baseline design.

the baseline optical design . 1 m is the largest possible diameter, given the size of the corresponding ports on the towers .

Glass baffles will not be installed, since the large diameter would imply more than ten fragile narrow baffles per link; stainless steel baffles could be used instead, as in the arm tubes, while parasitic beams will have to be caught by suitable glass traps.

15.5 Tower chambers upgrade

15.5.1 SR tower and IB,DT towers

The SR tower has to grow by 3 vertical rings to host a full size superattenuator. Also the separating roof has to be built. All this will be a simple replica of existing objects. IB and DT towers will grow by one ring, to allow longer SA with improved performances.

15.5.2 UHV air flux improvement

The contamination reduction during the payload integration phase in the Ultra High Vacuum chamber is a crucial item. To reduce mirror pollution a better system to direct a quasi-laminar air flow within the vacuum chamber will be designed, as requested since years. The circuit will use the present clean air supply, with the addition of two metallic diffusers, to be installed inside towers, feeding the air from the actual port in a quasi laminar way. The detailed design of the system depends on the shape of the new marionette and of its reference mass.

15.6 Towers displacement

The change in interferometer optical configuration and the control strategies require changes of up to about 1m in the position of the principal mirrors. The displacement of the towers involves a considerable work and is submitted to infrastructural constraints, affecting the final choice of the optical scheme, which is not yet finalized. The main limitation to the possible displacements comes from the structure of the Central building. In order to install the payloads from below, the towers have bottom flanges that can be opened and under each tower there is a rectangular aperture in the building floor, allowing to connect the tower inner volume to the basement clean room. The maximum allowed displacement has to preserve this passage. Complex preparatory works will be necessary before the real tower displacement that could be done by moving the entire tower on special sliders or rollers, once removed links and payloads and having blocked the Superattenuators. A similar operation has been already performed successfully in the past, displacing the MC tower by about 800 mm.

15.7 Control system

The vacuum control system comprises 22 main control stations, and several other components installed along the whole vacuum system. It includes also the supervisor software which is used to drive the vacuum system. While being effective for today's needs, it requires to be revised, since it has been designed more than 10 years ago, based on the OS-9 standard, using components no more available on the market. This procedure has already been started and will have to be strongly boosted for sake of AdV. Besides the new hardware, it will be necessary to upgrade also the control logic, both hardware and software, for more versatility and to include new coming devices, like new pumping stations and pump types. Suitable interlocks and loops shall be added to actively control the improved vacuum conditions .

16 Infrastructure modifications: proposed strategy for environmental noise reduction

16.1 Subsystem overview

The IME subsystem (Infrastructure Modifications for Environmental noise reduction) concerns all the hard works aimed to reduce the level of anthropogenic noise into the experimental buildings. The main tasks of IME will be: the replacement of the machines with more silent ones and, if needed, their displacement out of the experimental halls; the improvement of the insulation performances of the air flow distribution systems; the realization of adequate acoustically insulated rooms to displace the noisy electronics (or part of it); the improvement of the Laser and Detection laboratories walls insulation. The subsystem will also be involved in minor tasks such as the support in the realization of the eventual infrastructural works needed for the installation of the deliverables of the other subsystems.

16.2 The noise hunting activity

16.2.1 Introduction

During Virgo/Virgo+ (V/V+) commissioning the most relevant noise-inducing machines have been identified and progresses have been made in understanding the coupling mechanisms between such noises and the interferometer. The description of such activities is provided in [154].
In order to mitigate the environmental noises several infrastructure works have been performed during V/V+ commissioning. A description of these actions is reported in [155] where, for each work, are detailed the motivations, the noise mitigation achieved, the limitations/side effects (if presents) and the residual noise.

16.2.2 Location of noisy components

The following figures show the position of the identified or suspected noisy equipments in each experimental building with respect to the scientific apparatus. Figures 51 and 52 refer to the Central Building (CB) (respectively Level 0, tower basement, and Level 1, metallic platform), Figure 53 shows the MC (Mode Cleaner), while Figure 54 shows the WEB (West End Building) (the NEB (North End Building) is symmetric).

16.3 Solutions for the infrastructure changes

In addition to the above mentioned works, in the following we propose the reference solution for IME, sorting the proposed works by priorities. Such priorities are based on:

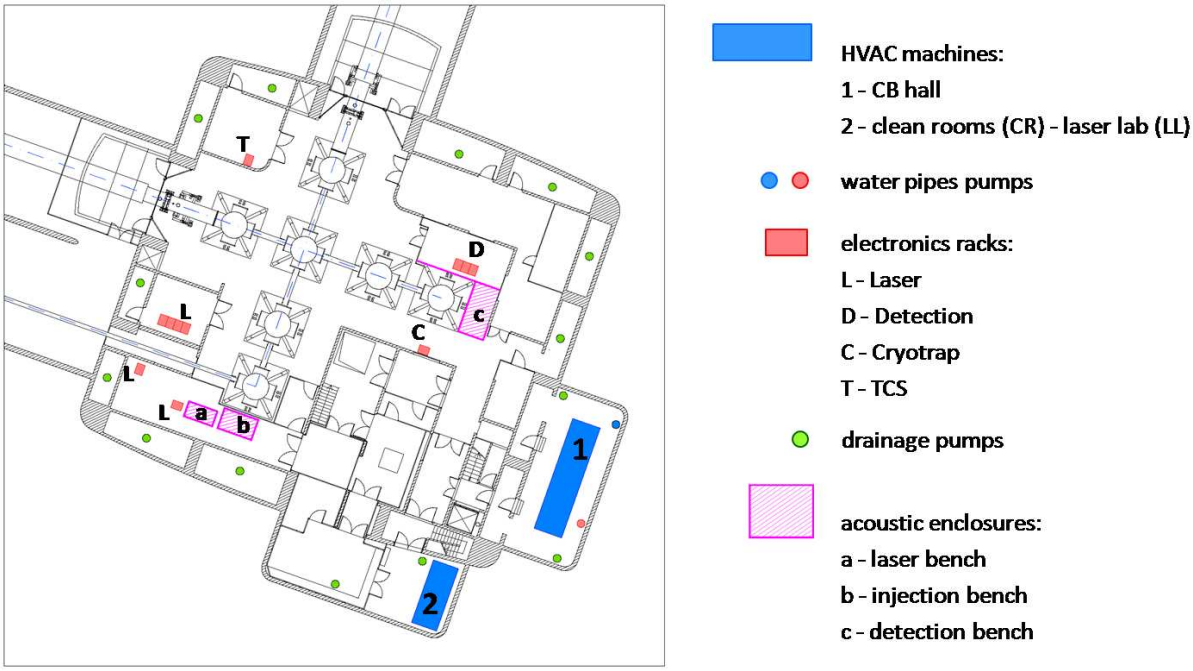

Figure 51: Central Building, Level 0 - Plan View.

- the trade-off between cost and efficiency in terms of noise mitigation;
- the need for upgrades of old machines;
- the need for maintenance and further non-IME upgrades: cryotraps; IMMS (Infrastructure Monitoring Machines System) improvements; modifications of spaces and electric systems for other subsystems installations.

16.3.1 Possible further environmental noise mitigations

For each experimental building possible interventions have been identified. Some of these interventions are evidenced by scientific observations (see [154]), while others are required for technical and functional reasons, or consequently to equipment re-arrangements. It is also reported the expected gain in terms of sensitivity, when this has been evidenced by scientific observations.

Central Building:

- HVAC systems of CB hall and Clean Rooms (CR) need further reduction of acoustic and seismic emissions in the experimental hall and Laser Laboratory (the expected environmental noise reduction is a factor 2 below 50Hz);

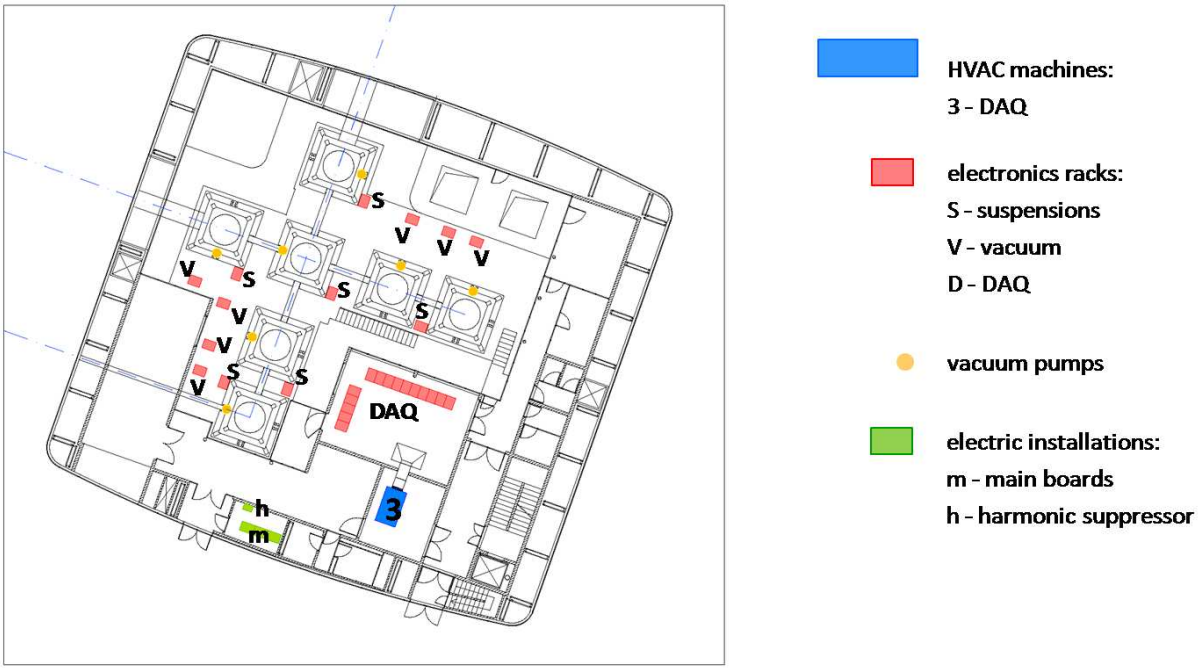

Figure 52: Central Building, Level 1 - Plan View.

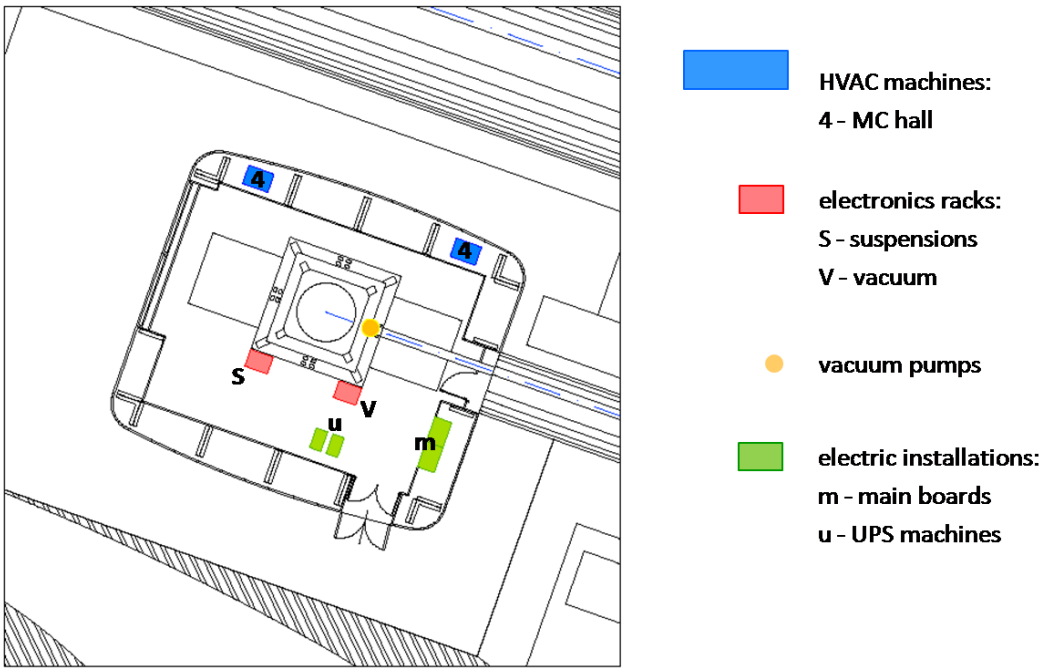

Figure 53: Mode Cleaner Building - Plan View.

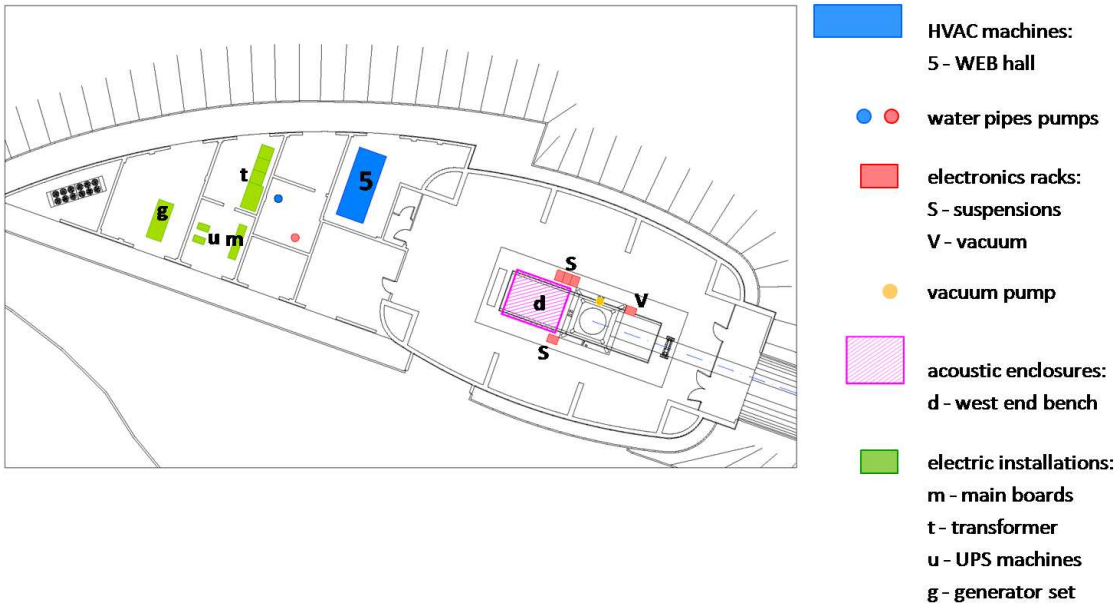

Figure 54: West End Building - Plan View.

- electronics racks need to reduce electro-magnetic (EM) and acoustic emissions, which would require to displace them, or at least their noisiest components (AC/DC converters), in dedicated acoustically isolated places (expected acoustic RMS noise reduction is a factor 5 above 50Hz, while the expected reduction of EM noise is a factor 5 to 10 below 100Hz);
- vacuum scroll pumps are very noisy devices and will run continuously for AdV, thus they should be displaced from towers in an acoustic and seismic isolated place.

Mode Cleaner Building:

- HVAC machines need to be replaced to eliminate disturbing EM noise, displacing them outside would also help to reduce the large acoustic and seismic emissions.

End Buildings:

- HVAC systems emit large acoustic noise and affect external benches: they need to be modified for running at lower air flow (expected acoustic noise reduction by a factor 5 below 100Hz).

Air distribution improvements (for each experimental building):

- duct sections could be increased in order to reduce the air and fans speed;
- air flow strengtheners and silencers could be added.

We expect acoustic noise reduction from both actions.

16.3.2 Motivations for changes not directly linked with noise mitigation

The proposed infrastructure changes are motivated not only by noise mitigation, but also by technical and functional reasons, as:

- the improvement of the equipments efficiency and reliability, replacing heavily used machines;
- the over or under-dimensioning of the current machines;
- the flexibility for adjusting the running conditions of the machines (i.e. a lower regime might be required if the towers will be thermally insulated);
- the separation of the systems to adjust independently the running conditions for different labs;
- the relocation of the machines would allow a gain in time for installation, easier maintenance and better working conditions;
- the improvement of the thermal insulation for energy saving.

16.3.3 Prioritization of the proposed solutions

As consequence of the considerations stated in the previous Sections 16.3.1 and 16.3.2, the proposed infrastructure improvement works for IME have been grouped into 3 packages, corresponding to an increasing cost, but characterized by a decreasing grade of priority: Level A, B and C.
However, the baseline solution taken into consideration in the costs budget refers to levels A+B only.

Level A. It includes the following infrastructure changes, divided for their motivation:

- A.1 (evidenced by scientific observations):
  - the installation of new HVAC machines for CB (CB hall+Laser Lab+Electronic Equipments (EE) Room) (ref. [154], Sec.1, figures 3 and 4);
  - the acoustic and seismic isolation of the HVAC CR machine (ref. [154], Sec.1, fig.1);
  - the installation new HVAC machine for MC and relocation (ref. [154], Sec.1 fig.1 and Sec.4 fig.13);

  - the realization of insulated EE rooms for noisy racks and power supplies (Laser Lab+Detection Lab+Vacuum+Suspensions+Data Acquisition) in CB (ref. [154], Sec.2, fig.8 and 9, Sec.4 Fig. 13 and 14);
  - the realization of insulated rooms for vacuum scroll pumps (ref. [154], Sections 3.1 and 3.4, fig.10);
  - the improvements of the Laser Lab and Detection Lab walls insulation (ref. [154], Sec.2).

- A.2 (for easier maintenance, better working conditions and the A.1 re-arrangements):
  - the relocation of CB HVAC machines (CB hall and CR);
  - the realization of new underground water pipes for CB HVAC machines;
  - the IMMS improvement;
  - the electric systems modifications for HVAC machines installation.

- A.3 (works for the other subsystems):
  - the realization of external areas for Cryotraps LN2 tanks;
  - the modifications of spaces and electric systems for other subsystems installations.

  The following figures, from 55 to 57, show drawings of the preliminary design of such solutions.

Level B. As further improvements in addition to Level A, Level B includes the following infrastructure changes:

- the installation of new HVAC air distribution for all experimental buildings;
- the realization of End Building HVAC machines seismic isolation (ref. [154], Sec.3, fig.12).

Level C. Finally, as lower level of priority, Level C includes, in addition to Levels A and B, the following infrastructure works:

- the reduction of the high value of the reverberation time for each experimental hall.

It has to be observed that Level C interventions have to be carefully evaluated due to the difficulty of realization and the various drawbacks. However, its level of priority could be increased in case other interventions could not be carried out (like the displacement of the noisy electronics).

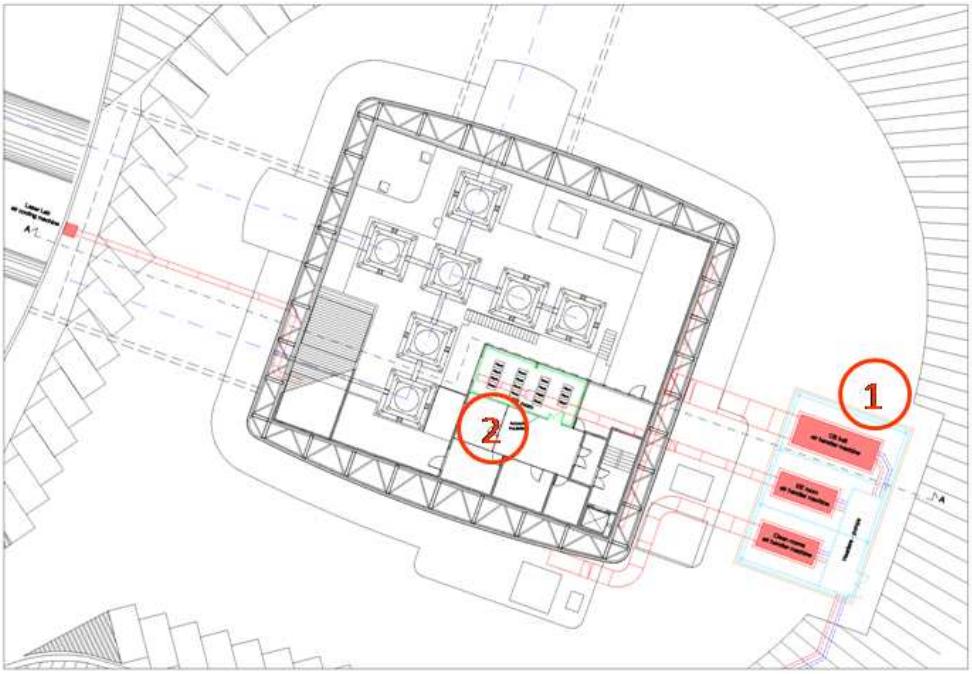

Figure 55: Plan view of the Central Building, Level 2 - 1) New external technical area, 2) EE Room (indicative location).

16.4 Particularity of the subsystem

A few considerations have to be made in order to underline the particularity of IME with respect to the other subsystems.
The basic requirements of the IME design are difficult to fix since the scope of the project - the environmental noise mitigation - is to be evaluated not in view of complying with general standards or official laws, but with the future AdV interferometer sensitivity. As a consequence also cost-benefits analyses are very hard to perform.
In fact, a fundamental role in defining the design requirements will be played by the result of Virgo+ environmental noise mitigation activity, as described in the previous Section 16.2. A preliminary evaluation of the works performed seems to be encouraging, however the effectiveness of the mitigation campaign has to be evaluated in parallel with the interferometer running and the increase of sensitivity.
On the other side, it has to be noted that the results expected from Virgo+ mitigation works can only represent a projection of the present noises on the AdV sensitivity. Considering the large amount of noises produced to the interferometer by various noisy sources, we should avoid to face the possibility that not yet evidenced noise coupling could affect the AdV interferometer in the new most sensitive configuration.
Besides, there are still some uncertainties in defining the IME design requirements concerning important design solutions that could be envisaged by other subsystems/Virgo groups in relation to the AdV project, such as the thermal stability of the towers and the electric power DC distribution for the experimental halls apparatus. The implemen-

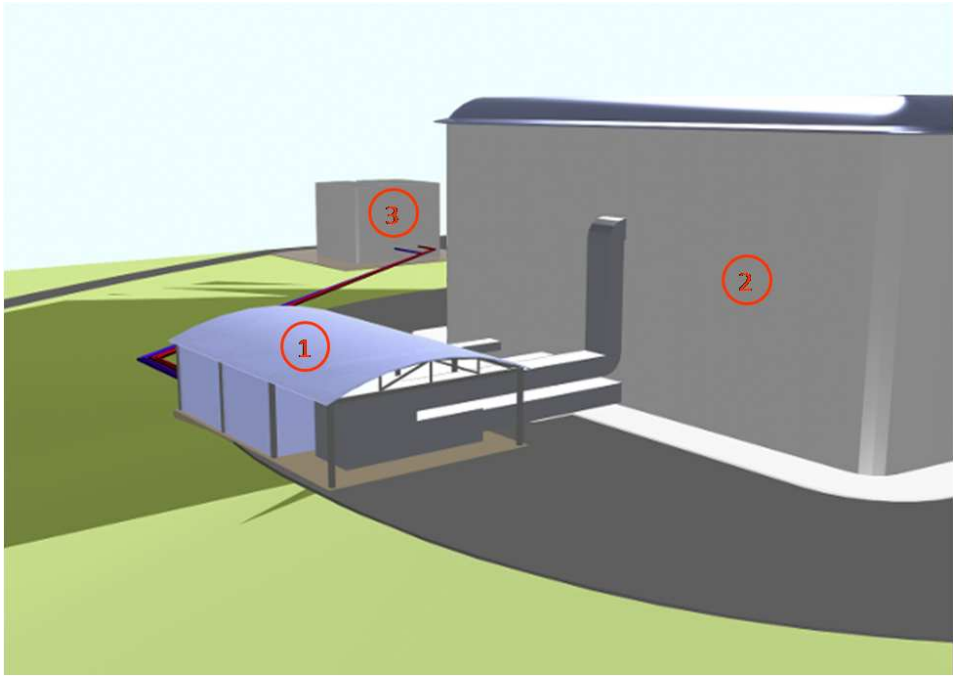

Figure 56: Perspective view of the Central Area - 1) New external technical area, 2) Central Building, 3) Technical Building.

tation of such solutions would significantly affect the definition of the specifications for the HVAC systems and for the electrical power systems and, consequently, the strategy to adopt in order to reduce environmental noises.
Moreover, other important improvements of the interferometer sensitive components are currently under study or discussion, as the improvements of the seismic and acoustic isolation of the in-air optical benches with in vacuum and/or suspended solutions, or the radiofrequency shielding of the electronic racks. This could have a remarkable impact on the noise hunting activity, modifying the specifications for the noisy systems. However the full results are not likely to be available before the AdV project approval; besides, such alternative strategies will inevitably need other infrastructure modification works.
In light of the above, at present the IME subsystem keeps open various possible strategies to approach the problem of noise mitigation.
The baseline solution described in the previous sections represents a preliminary design of the infrastructure changes for the environmental noise mitigation, mainly based on the experiences gained with regard to Virgo systems operation, the rules quoted in literature and qualitative considerations.
Therefore, the hypotheses evaluated are based on the "principle of care". Given the heavy impact on the interferometer of the civil engineering modification works and the uncertainties of their effective mitigation effects, it is necessary to take into account significant safety margins. Interventions "a posteriori" to be realized during the commission phase of AdV are generally more expensive, difficult to implement and would require the interruption of the scientific activity.

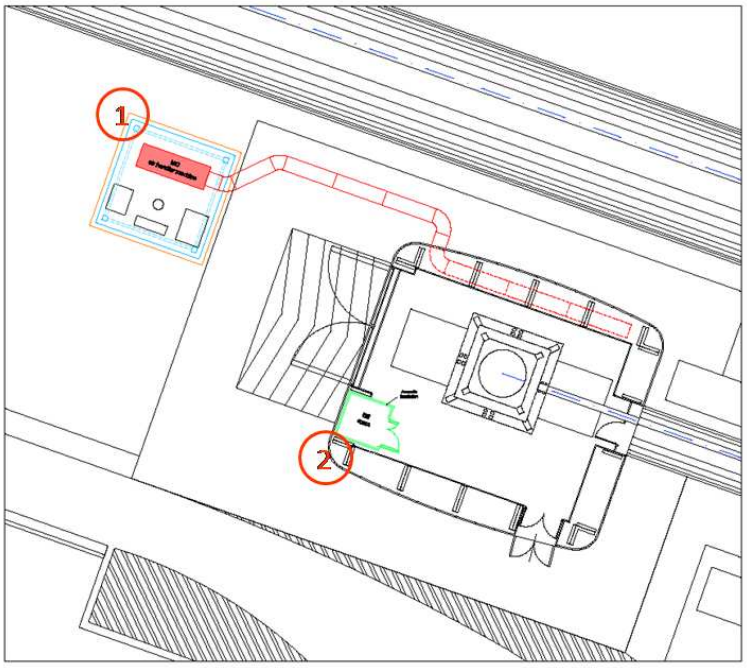

Figure 57: Plan view of the Mode Cleaner - 1) New external technical area, 2) Vacuum pumps Room (indicative location).

References

[1] R.Flaminio, A.Freise, A.Gennai, P.Hello, P.La Penna, G.Losurdo, H.Lueck, N.Man, A.Masserot, B.Mours, M.Punturo, A.Spallicci, A.Viceré, *Advanced Virgo White Paper*, Virgo Internal report VIR-NOT-DIR-1390-304 (2005). 3

[2] The Virgo Collaboration, *Advanced Virgo Conceptual Design*, Virgo Internal report VIR-042A-07 (2007). 3

[3] The Virgo Collaboration, *Advanced Virgo Preliminary Project Execution Plan*, Virgo Internal report VIR-043A-07 (2007). 3

[4] The Virgo Collaboration, *Advanced Virgo Preliminary Design*, Virgo Internal report VIR-089A-08 (2008). 3

[5] Advanced LIGO team, *Advanced LIGO Reference Design*, LIGO-M060056-06-M (2006). 3

[6] S. Hild, G. Losurdo and A. Freise: *Optimising the Advanced Virgo sensitivity for astrophysical sources*. Presentation at Virgo week July 2008. Available at http://wwwcascina.virgo.infn.it/collmeetings/presentations/2008/2008-07/AdV/hild_160708.ppt 11, 46

[7] http://lhocds.ligo-wa.caltech.edu:8000/advligo/GWINC . 11

[8] S. Hild and G. Losurdo: *Advanced Virgo design: Comparison of the Advanced Virgo sensitivity from Bench 4 and GWINC (v1)*, Virgo note, VIR-055A-08 (2008). 11, 45

[9] S. Hild, A. Freise and G. Losurdo: *Sensitivity Options for the Advanced Virgo Baseline Design*, Virgo note, VIR-026A-09 (2009). 11

[10] C.Kim, V.Kalogera and D.Lorimer, *Effect of PSRJ0737-3039 on theDNS Merger Rate and Implications for GW Detection*, astro-ph:0608280 http://it.arxiv.org/abs/astro-ph/0608280, to appear in proceedings of "A life with stars", a conference in honour of Ed van den Heuvel (Amsterdam, August 2005). 16

[11] K.Belczynski, R.E.Taam, V.Kalogera, F.A.Rasio, T.Bulik, *On the rarity of double black hole binaries: consequences for gravitational-wave detection,* astro-ph:0612032 http://it.arxiv.org/pdf/astro-ph/0612032, The Astrophysical Journal 662:1 (2007) 504-511. 16, 18, 19, 20

[12] CBC Group, *Rate predictions for LIGO-Virgo Compact Binary Coalescence events*, https://www.lsc-group.phys.uwm.edu/ligovirgo/cbc/protected/papers/rates/rates.pdf (2009) 17

[13] F.Pretorius, *Evolution of binary black hole spacetimes.*, Phys.Rev.Lett.**95**:121101,2005. 19

[14] F.Pretorius *Simulation of binary black hole spacetimes with a harmonic evolution scheme*, Class.Quant.Grav.**23**:S529-S552,2006. 19

[15] A.Buonanno, G.B.Cook, F.Pretorius *Inspiral, merger and ring-down of equal-mass black-hole binaries*, Phys.Rev.D**75**:124018,2007. 19

[16] M.Vallisneri *Prospects for gravitational wave observations of neutron star tidal disruption in neutron star / black hole binaries.*, Phys.Rev.Lett.**84**:3519,2000. 19

[17] T.Bulik, K.Belczynski, A.Prestwich, *IC10 X-1: the immediate progenitor of a double black hole* astro-ph:0803.3516 http://it.arxiv.org/pdf/0803.3516, submitted to Astrophysical Journal. 19, 21

[18] R.Narayan, Ap.J.**319** (1987), 162. 23

[19] The LIGO Scientific Collaboration *All-sky LIGO Search for Periodic Gravitational Waves in the Early S5 Data*, LIGO-P080024, http://arxiv.org/abs/0810.0283 23

[20] R.Diehl et al (INTEGRAL) *Radioactive ^{26}Al from massive stars in the Galaxy*, Nature **439** (2006), 45-47 25

[21] C.Ott *The gravitational wave signature of core collapse supernovae*, astro-ph:0809.0695v1 http://arxiv.org/abs/0809.0695v1 25

[22] N.Arnaud, M.Barsuglia, M.A.Bizouard, F.Cavalier, M.Davier, P.Hello, T.Pradier *Gravity wave and neutrino bursts from stellar collapse: A Sensitive test of neutrino masses.* Phys.Rev.D**65**:033010,2002 25

[23] The LIGO Scientific Collaboration, *Search for gravitational wave radiation associated with the pulsating tail of the SGR 1806-20 hyperflare of December 27, 2004 using LIGO*, astro-ph:0703419, http://arxiv.org/abs/astro-ph/0703419, Phys.Rev.D**76** (2007) 062003 26

[24] S.E.Woosley and J.S.Bloom *The Supernova - Gamma-Ray Burst Connection*, astro-ph/0609142v1, Ann.Rev.Astron.Astrophys.**44** (2006) 507-556. 26

[25] W.H.Lee, E.Ramirez-Ruiz *The Progenitors of Short Gamma-Ray Bursts*, astro-ph/0701874v3, New J.Phys **9** (2007) 17. 26, 34

[26] F.Acernese et al. (The Virgo Collaboration) *Search for gravitational waves associated with GRB 050915a using the Virgo detector*, to appear in Class.Quant.Gravity (2008). 27

[27] Y. Gürsel, M. Tinto, *Near optimal solution to the inverse problem for gravitational wave bursts*, Phys.Rev.D**40**:3884-3938,1989. 30

[28] N.Arnaud, M.Barsuglia, M.A.Bizouard, V.Brisson, F.Cavalier, M.Davier, P.Hello, S.Kreckelbergh, E.K.Porter *Coincidence and coherent data analysis methods for gravitational wave bursts in a network of interferometric detectors.*, Phys.Rev.D**68**:102001,2003. 31, 32

[29] A.Viceré, *Network analysis for coalescing binaries: Coherent versus coincidence based strategies.*, Class.Quant.Grav.**21**:S1793-S1800,2004. 31

[30] A.Viceré, *Advanced Virgo in the LIGO-Virgo network* https://workarea.ego-gw.it/ego2/virgo/advanced-virgo/erc/public-materials/vicere_LVCvsLIGO_27april2009.pdf, (2009). 31

[31] C.Rover, R.Meyer, G.M.Guidi, A.Vicere, N.Christensen, *Coherent Bayesian analysis of inspiral signals.*, Class.Quant.Grav.**24**:S607-S616,2007. 31

[32] F.Cavalier, M.Barsuglia, M.A. Bizouard, V.Brisson, A.C.Clapson, M.Davier, P.Hello, S.Kreckelbergh, N.Leroy, M.Varvella, *Reconstruction of source location in a network of gravitational wave interferometric detectors.*, Phys.Rev.D**74**:082004,2006. 31

[33] F.Beauville et al. (The joint LIGO-Virgo working group) *A comparison of methods for gravitational wave burst searches from LIGO and Virgo.* Class.Quant.Grav.**25** (2008) 045002. 31

[34] F.Beauville et al. (The joint LIGO-Virgo working group) *Detailed comparison of LIGO and Virgo inspiral pipelines in preparation for a joint search* Class.Quant.Grav.**25** (2008) 045001. 31

[35] S.Birindelli, *Coherent algorithm for reconstructing the location of a coalescing binary system using a network of three gravitational interferometers*, Ph.D. thesis, University of Pisa, 2008, http://www.infn.it/thesis/PDF/getfile.php?filename=2427-Birindelli-dottorato.pdf 31

[36] Chandra http://chandra.harvard.edu 32

[37] X-MM Newton http://xmm.esac.esa.int 32

[38] XEUS http://sci.esa.int/xeus 33

[39] SWIFT http://www.nasa.gov/mission_pages/swift/bursts/index.html 33

[40] GLAST http://www.nasa.gov/mission_pages/GLAST/team/index.html 33

[41] S.Fukuda et al. *The Super-Kamiokande detector*, N.I.M. A **501** (2003), 418-462. 33

[42] The LVD Collaboration *The 1 kton LVD neutrino observatory*, Proc. 27th ICRC,Hamburg, 1, 1093, 2001. 33

[43] S.R.Klein for the IceCube Collaboration *IceCube: A Cubic Kilometer Radiation Detector* http://www.icecube.wisc.edu/science/publications/update2008/update.pdf 33, 34

[44] SuperNova Early Warning System http://snews.bnl.gov 33

[45] Sudbury Neutrino Observatory http://www.sno.phy.queensu.ca 33

[46] SNO+ http://snoplus.phy.queensu.ca 33

[47] http://amanda.uci.edu 34

[48] The KM3NeT Consortium, *KM3NeT: Conceptual Design for a DeepâĂŘSea Research Infrastructure Incorporating a Very Large Volume Neutrino Telescope in the Mediterranean Sea*, http://www.km3net.org/CDR/CDR-KM3NeT.pdf 34

[49] ANTARES Collaboration *A Deep Sea Telescope for High Energy Neutrinos*, astro-ph/9907432v1 http://lanl.arxiv.org/abs/astro-ph/9907432v1 34

[50] NEMO http://nemoweb.lns.infn.it 34

[51] NESTOR http://www.nestor.noa.gr 34

[52] M. Mantovani, A. Freise, *Initial set of optical parameters for numerical simulations towards Advanced Virgo*, Virgo note VIR-002B-07 (2007). 38

[53] G. M. Harry et al *Thermal noise in interferometric gravitational wave detectors due to dielectric optical coatings Classical and Quantum Gravity* **19** (2002). 41

[54] S. Hild, A. Freise: *Advanced Virgo Design: Preliminary Revision of the Beam Size and the Test Mass Curvatures*, Virgo note VIR-038B-08 (2008). 41

[55] S. Hild, M. Mantovani, A. Perreca and A. Freise: *Advanced Virgo design: The Advanced LIGO approach for choosing modulation frequencies*, Virgo note VIR-066A-08 (2008). 42, 45

[56] S. Hild and A. Freise: *Near-symmetric arm cavity design for Advanced Virgo*, Virgo note VIR-087B-08 (2009). 42

[57] S. Hild and A. Freise: *Advanced Virgo Design: Differential Arm Length Noise from Vertical Movement of Wedged Input Mirrors*, Virgo note VIR-037A-08 (2008). 43

[58] S. Hild and A. Freise: *Choice of the Arm Cavity Finesse for Advanced Virgo*, Virgo note, VIR-22A-09 (2009) 43

[59] Meers B. J *Recycling in laser-interferometric gravitational-wave detectors*, *Phys. Rev. D* **38** (1988). 43

[60] Freise A and Heinzel G et al *Demonstration of detuned dual recycling at the Garching 30 m laser interferometer*, *Physics Letters A* **277** (2000). 43

[61] Hild S and Grote H et al *Demonstration and comparison of tuned and detuned signal recycling in a large-scale gravitational wave detector*, *Classical and Quantum Gravity* **24** (2007). 43

[62] S. Hild and A. Freise: *Why use FinesseTools for Advanced Virgo simulations*. Presentation at AdV biweekly meeting, June 2008. Available at http://wwwcascina.virgo.infn.it/advirgo/biweekly/2008/2008-06/hild_190608.ppt 45

[63] S. Hild, G. Losurdo and A. Freise: *Sensitivity curves for the Advanced Virgo Preliminary Design*, Virgo note VIR-101A-08 (2008). 45

[64] A. Freise, S. Hild and J. Marque *Advanced Virgo design: Layout options for the non-degenerate Recycling Cavities* Virgo note VIR-025A-09 (2009). 46

[65] S. Hild, M. Barsuglia and A. Freise *Thermal Noise Constraints for the Advanced Virgo Non-Degenerate Recycling Cavity Design* Virgo note VIR-005A-09 (2009). 47

[66] G.Vajente, PhD thesis *Analysis of sensitivity and noise sources for the Virgo gravitational wave interferometer*, Scuola Normale Superiore, Pisa (2008) 54

[67] D.Shaddock et al, *Opt Lett*, **24**, 1499, (1999). 56

[68] B.Willke, *Status of Adv Ligo PSL*, talk at the LSC-Virgo meeting, March 08, Caltech 57

[69] B. Canuel, R. Day, E. Genin, P. LaPenna, J. Marque, *AdV INJ: Design requirements*, May 2009, https://workarea.ego-gw.it/ego2/virgo/advanced-virgo/inj/resolveuid/9babbdec14f69977418f9ce21ca10101 58

[70] B. Canuel, R. Day, E. Genin, P. LaPenna, M. Mantovani, J. Marque, F. Paoletti, *AdV INJ: Preliminary Design Study*, Virgo Internal note, VIR-023A-09, May 2009, https://pub3.ego-gw.it/codifier/index.php?content=show&doc=2215 58, 60, 64, 65

[71] F.Acernese, *et al.* (The Virgo Collaboration), *Class. Quantum Grav.*, **21**, S395-S402 (2004). 63

[72] E. Genin, M. Mantovani and P. Ruggi, *Advanced Virgo INJ: Radiation pressure effects in the Advanced Virgo IMC - longitudinal and angular directions*, Virgo Internal note, VIR-009A-09, April 2009 64

[73] B.Canuel, Talk at AdV INJ IRC,*AdV INJ: High Power optical components*, AdV INJ-HPIO working area, https://workarea.ego-gw.it/ego2/virgo/advanced-virgo/inj/restricted/hpio-r-d/randd-presentation/INJ_canuel_290409.pptx/ 65, 66

[74] J.D. Mansell et al, Appl.Opt., 40, 366-374 (2001) 65

[75] LIGO T-060267-00-D (2006). 65

[76] G.Mueller, LIGO T020021-00-D (2002). 65

[77] P.Fritschel, LIGO T010075-00-D (2001). 65

[78] E. Khazanov et al, *IEEE Journ. Quant. Electr.*, **35** (8), (1999) 66

[79] E. Khazanov et al, *IEEE Journ. Quant. Electr.*, **40** (10), (2004) 66

[80] D.Tanner et al, *The LIGO input optics*, LIGO-G070296-00-R 66

[81] E.A. Khazanov, Quantum Electronics, 29(1), 59-64(1999) 67

[82] The Virgo collaboration, *In-vacuum optical isolation changes by heating in a Faraday isolator Appl. Opt.*, Vol. 47, Issue 31, pp. 5853-5861 (2008) 67

[83] V. Zelenogorsky, O.Palashova and E. Khazanova, Optics Communications Volume 278, Issue 1, 2007, 8-13 67

[84] Khazanov et al., *IAP report on High power Faraday isolator for AdV*, march 2009, AdV INJ-HPIO working area, https://workarea.ego-gw.it/

ego2/virgo/advanced-virgo/inj/restricted/documents/advanced-virgo/high-power-faraday-isolator/Virgo_report_March_IAP.pdf/ 67

[85] C.Comtet et al., *Proceedings of the 42th Rencontres de Moriond*, 2007. 69, 71

[86] Z. Yan, Li Ju, *et al.*, Applied Optics 45 (2006) 2631-2637 69

[87] http://www.virgo.optique.espci.fr/Virgo_Mirrors/ 70

[88] A.Brillet, *et al.*, Phys. Rev. D, **67**(10), 102006 (2003) 70

[89] F. Bondu, M. Laval and J.-Y. Vinet Virgo Note VIR-054A-07 (2007). 70

[90] M. Smith, P. Willems, Auxiliary Optics Support System Conceptual Design Document, Vol. 1 Thermal Compensation System, LIGO-T060083-01-D 74, 80

[91] V. Fafone, talk at the Advanced Virgo Meeting, Cascina March 12, 2009. 75, 78

[92] A. Rocchi, talk at the Advanced Virgo Meeting, Cascina December 18, 2008. 76

[93] P. Willems, LIGO-T060224-00D (2006). 76, 77

[94] R.C. Lawrence, Ph.D. thesis, MIT, 2003, LIGO-P030001-00-R. 76, 79

[95] A. Rocchi, talk at the LSC-Virgo Meeting, Cascina May 24, 2007. 76

[96] V. Fafone, talk at the Virgo Meeting, Cascina July 16, 2008. 76

[97] Optickle web-page http://ilog.ligo-wa.caltech.edu:7285/advligo/ISC_Modeling_Software 77

[98] G. Vajente, M. Mantovani, talk at the Advanced Virgo Meeting, Cascina October 16, 2008. 77

[99] F. Bondu, private communications. 77

[100] J. Degallaix, Ph.D. thesis, UWA, 2006. 79

[101] J.Y. Vinet, in http://wwwcascina.virgo.infn.it/commissioning/OPC/Talks/TCSworkshop011008/Vinet_011008_TCS-WRKSHP.ppt 79

[102] A.F. Brooks, *et al.*, LIGO?P080089?00?Z (2008). 80

[103] T.L. Kelly, *et al.*, *Appl. Opt.*, **46**(6), 861-866 (2007) 80

[104] Y. Fan, *et al.*, Rev. Sci. Instrum. **79**, 104501 (2008). 81

[105] E. Tournefier, *Technical noises for Virgo+: DC and AC readout cases*, VIR-NOT-LAP-1390-338 83

[106] G. Vajente, *"Advanced Virgo Length Sensing and Control System: parameters for Non-Degenerate Recycling Cavities"*, Virgo Internal Document VIR-080A-08 (2008) 84, 94

[107] G. Vajente, *"Simulation of Advanced Virgo Length Sensing and Control System"* Virgo Internal Document VIR-068B-08 (2008) 84

[108] G. Vajente, *"Requirements for the Advanced Virgo Length Sensing and Control system"*, Virgo Internal Document VIR-083A-08 (2008) 84, 93, 95

[109] E. Tournefier, *Back-scattering by the optical benches: results from Virgo and constraints for AdV Technical noises for Virgo+: DC and AC readout cases*,VIR-NOT-070A-08 84

[110] E. Tournefier, *Advanced Virgo output mode cleaner: specifications"*,VIR-NOT-071-08 86

[111] E. Tournefier, *"Advanced Virgo output mode cleaner: specifications"*, Virgo Internal Document VIR-071A-08 (2008) 91

[112] G. Vajente, *"Note on signal recycling I: Field equations"*, Virgo Internal Document VIR-030B-08 (2008) 91, 92, 93

[113] F. Bondu, *"AdV Interferometer Sensing and Control: Design Requirement Document"*, Virgo Internal Document VIR-024A-09 (2009) 91

[114] F. Acernese et al. [Virgo collaboration], *"The variable finesse locking technique"*, Class. Quant. Grav. **23** (2006) S63 92

[115] F. Acernese et al. [Virgo collaboration], *"Lock acquisition of the Virgo gravitational wave detector"*, Astropart. Phys. **30** (2008) 29 92

[116] G. Vajente, *"Note on signal recycling II: Lengths and modulations"*, Virgo Internal Document VIR-032A-08 (2008) 92, 93

[117] G. Vajente, *"Possible sets of lengths and modulation frequencies for Advanced Virgo"*, Virgo Internal Document VIR-049A-08 (2008) 94

[118] G. Vajente, *"Simulation of Advanced Virgo Length Sensing and Control system"*, Virgo Internal Document VIR-068B-08 (2008) 94

[119] B. Swinkels, E. Campagna, G. Vajente, L. Barsotti and M. Evans, *"Longitudinal noise subtraction: the alpha-, beta- and gamma-technique"*, Virgo Internal Document VIR-050A-08 (2008) 95

[120] M. Mantovani, A.Freise, S.Hild: *The consequences of using the etalon effect to tune the arm cavity finesse on the alignment signals for Advanced Virgo*, Virgo note VIR-027A-08 (2008). 96

[121] M. Mantovani, *"Advanced Virgo single cavity alignment"* Virgo Internal Document VIR-109A-08 (2008) 96

[122] V B Braginsky, S E Strigin, and S P Vyatchanin, *Phys. Lett. A* **287**, 331 (2001) 96

[123] C. Zhao *et al.*, *Phys. Rev. Lett.* **94**, 121102 (2005) 96

[124] T. Carmon *et al.*, *P*hys. Rev. Lett. **95**, 223902 (2005) 96

[125] O Arcizet *et al.*, *Nature* **444**, 71 (2006) 96

[126] C Zhao *et al.*, *P*hys. Rev. A **78**, 023807 (2008) 96

[127] *SAFE: Superattenuator Facility at EGO*, VIR-048A-07 (2007). 101

[128] G. Losurdo, D. Passuello, P. Ruggi, VIR-NOT-FIR-1390-318 (2006) 103

[129] S. Braccini et al., Rev. Sci. Instrum. 66 (3), 2673 (1995) 103

[130] A.N. Luiten et al, Rev. Sci. Instrum. 68, 1889 (1997) 103

[131] SAT Group,*"SAT AdV Plan for R&D, SR Construction and Short SA Upgrade"*, VIR-091A-08 (2008) 104

[132] SAT Group,*"AdV Superattenuators Risk Assesment"*, VIR-110A-08 (2008) 104

[133] G. Vajente, VIR-083A-08 (2008) 104

[134] M. Barsuglia,P. Ruggi, internal presentation at OSD workshop, (Jan. 2009) http://wwwcascina.virgo.infn.it/advirgo/090129/ 105

[135] A. Gennai, *"Advanced Virgo-Suspension Control System"*,VIT-NOT-PIS-4900-151, (2009) 105

[136] M. Ferrante, *"Caratterizzazione e realizzazione di una scheda di conversione D/A A/D per l'esperimento VIRGO"*, University Degree thesis, Facoltà di Ingegneria Università di Pisa. 106

[137] G. Scandurra, *"Sviluppo di una scheda di I/O dotata di interfacce PCI e IEEE1394b per il rivelatore Virgo"*, fellowship paid by Fondazione Bonino-Pulejo. 106, 107

[138] The Virgo Collaboration, *Commissioning progress report for the STAC and EGO council*, VIR-043A-08 (2008). 107

[139] A. Gennai, *DAC Contribution to Virgo Sensitivity*, VIR-072A-08 (2008). 107

[140] A. Gennai, *New DSP board installation*, http://wwwcascina.virgo.infn.it/collmeetings/DMwebpages/Virgo+/2ndReviewDocuments/DSP.pdf. 107

[141] https://workarea.ego-gw.it/ego2/ego/itf/software/auth-only/projects/superattenuator-controlsoftware 108

[142] P.Puppo and P.Rapagnani, VIR-NOT-ROM-1390-311 113

[143] F.Frasconi et al., Virgo Note VIR-024A-08 (2008). 114

[144] A. Heptonstall, I. Martin, A. Cumming, C.A. Cantley, G. Cagnoli, R. Jones and D.R.M. Crooks, Production and characterization of synthetic fused silica ribbons for advanced ligo suspensions, 2005. LIGO technical note, LIGO-T050206-00-K. 120

[145] For details see M.Lorenzini, "Suspension thermal noise issues for advanced GW interferometric detectors", thesis for Dottorato di Ricerca in Astronomia, University of Florence (http://www.infn.it/thesis/). 121

[146] T. Bouedo, S. Cap, N. Letendre, A. Masserot, B. Mours, J.M. Nappa, E. Pacaud, S. Vilalte, *Virgo+ Control and DAQ Electronic Deployment*, VIR-022C-07 (2007). 125

[147] T. Bouedo, F. Carbognani, N. Letendre, A. Masserot, B. Mours, E. Pacaud, D. Sentenac, *New Global Control*, VIR-056A-o8 (2008). 125

[148] O. Chautemps, C. Drancourt, N. Letendre, A. Masserot, B. Mours, J. Prast, *Proposal for the Timing & Optical Links Mezzanine (TOLM)*, VIR-NOT-LAP-1390-279 (2004). 126

[149] LAPP Group, *MUX/DEMUX optical card specifications*, VIR-NOT-LAP-1390-321 (2006). 126

[150] N. Letendre, A. Masserot, B. Mours, *Virgo+ Timing Deployment*, VIR-073A-08 (2008). 126

[151] LAPP Group, *ADC Board Specifications*, VIR-NOT-LAP (2007). 126

[152] A. Gennai, *Advanced Vigo Suspension Control*, VIR-NOT-4900-151 (2008). 127

[153] EGO Software Group, *Non Commercial Framework for Distributed Control Systems*, EGO-NOT-OPE-92 (2006). 130

[154] I.Fiori, *Environmental noise: experience with Virgo/V+ commissioning and indication of further mitigations*, VIR-019A-09. 141, 142, 145, 146

[155] I.Fiori, *Infrastructure works for the mitigation of environmental noises during Virgo commissioning and plans until VSR2*, VIR-018A-09. 141